Modelling of High Temperature Polymer Electrolyte Fuel Cells

Qing Cao

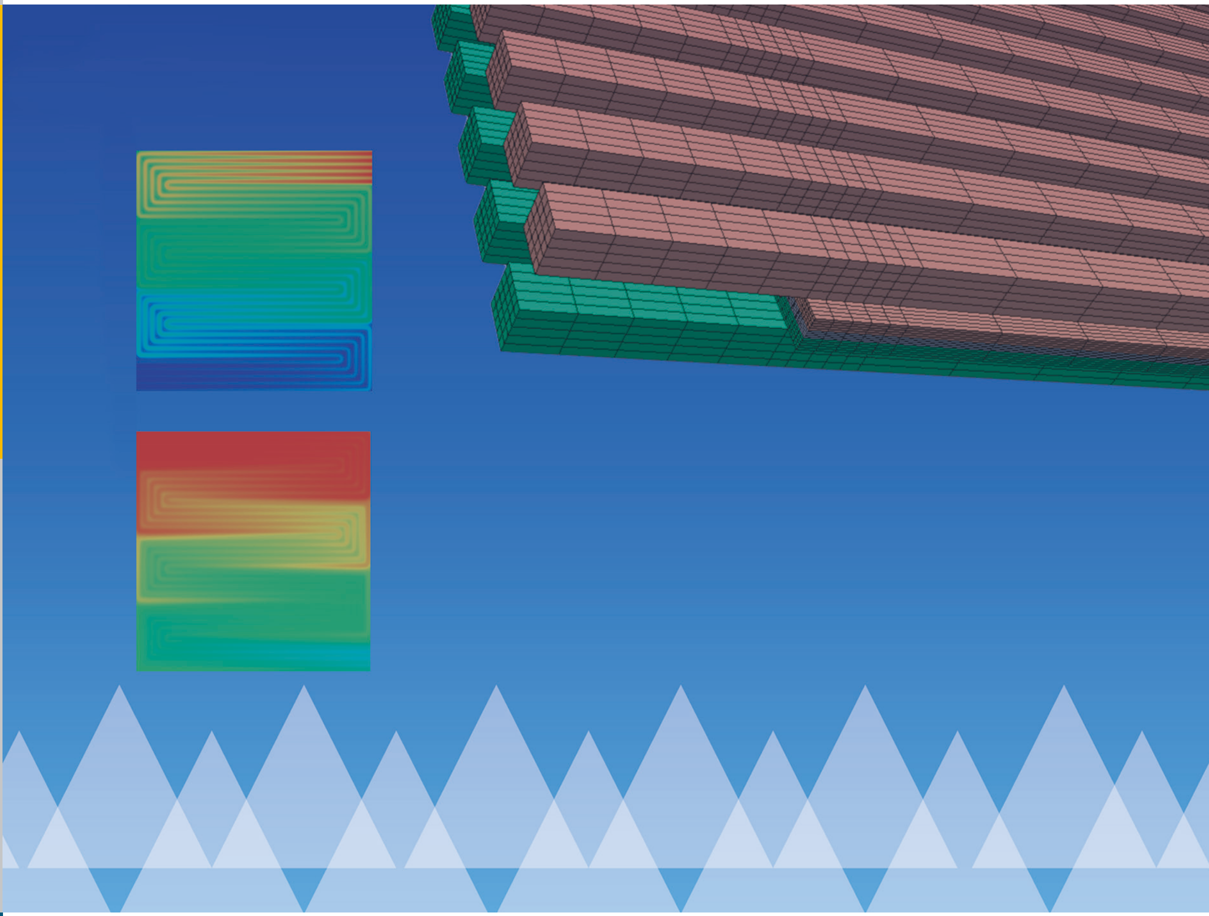

Member of the Helmholtz Association

Energie & Umwelt /
Energy & Environment
Band / Volume 389
ISBN 978-3-95806-263-4

JÜLICH
FORSCHUNGSZENTRUM

Schriften des Forschungszentrums Jülich
Reihe Energie & Umwelt / Energy & Environment Band / Volume 389

Forschungszentrum Jülich GmbH
Institute of Energy and Climate Research
Electrochemical Process Engineering (IEK-3)

Modelling of High Temperature Polymer Electrolyte Fuel Cells

Qing Cao

Schriften des Forschungszentrums Jülich
Reihe Energie & Umwelt / Energy & Environment Band / Volume 389

ISSN 1866-1793 ISBN 978-3-95806-263-4

Bibliographic information published by the Deutsche Nationalbibliothek.
The Deutsche Nationalbibliothek lists this publication in the Deutsche
Nationalbibliografie; detailed bibliographic data are available in the
Internet at http://dnb.d-nb.de.

Publisher and Distributor: Forschungszentrum Jülich GmbH
Zentralbibliothek
52425 Jülich
Tel: +49 2461 61-5368
Fax: +49 2461 61-6103
Email: zb-publikation@fz-juelich.de
www.fz-juelich.de/zb

Cover Design: Grafische Medien, Forschungszentrum Jülich GmbH

Printer: Grafische Medien, Forschungszentrum Jülich GmbH

Copyright: Forschungszentrum Jülich 2017

Schriften des Forschungszentrums Jülich
Reihe Energie & Umwelt / Energy & Environment, Band / Volume 389

D 82 (Diss. RWTH Aachen University, 2017)

ISSN 1866-1793
ISBN 978-3-95806-263-4

The complete volume is freely available on the Internet on the Jülicher Open Access Server (JuSER)
at www.fz-juelich.de/zb/openaccess.

This is an Open Access publication distributed under the terms of the Creative Commons Attribution License 4.0,
which permits unrestricted use, distribution, and reproduction in any medium, provided the original work is properly cited.

Modelling of High Temperature Polymer Electrolyte Fuel Cells

by Qing Cao

Abstract

Fuel cells are energy conversion devices that generate electricity and heat through electrochemical reactions involving hydrogen and oxygen. They are divided into different types according to the electrolytes and the operating temperatures. One promising fuel cell type, which can be used as an on-board power supply in trucks or airplanes, is the high-temperature polymer electrolyte fuel cell (HT-PEFC). In a HT-PEFC, phosphoric acid-doped polybenzimidazole is employed in the electrolyte. The typical working temperature of this fuel cell type is between 150 ℃ and 180 ℃.

The aim of this thesis is the 3D modeling of HT-PEFC at the cell level, in order to better understand the physical and electrochemical processes within the cell. The open-source software OpenFOAM is used as a platform for model development. Four models were implemented to describe different phenomena.

- The first model describes electrochemistry with effective parameters related to the geometric surface of the catalyst layer. Mass transfer in the porous gas diffusion layer is represented by a simple Fick's law approach.

- The second model employs a macrohomogeneous approach for the description of electrochemistry, whereby the penetration depth of the electrochemical reaction in the catalyst layer is considered to be a function of the current density.

- A mathematical description of water transport from the cathode side to the anode side of the phosphoric acid doped polybenzimidazole membrane, during fuel cell operation, is depicted in the thirdmodel.

- The fourth model compares gas transport in the gas diffusion layer, as described by a Stefan-Maxwell approach, with the gas transport according to model 1, above.

The mathematical models developed in the present work were validated by comparison of the numerical calculations with experimental data and analytical solutions. Two different cell geometries were considered: a cell with parallel straight channels, with an active area of 0.2 cm^2, and a 50 cm^2 cell, with meandering (serpentine) channels. The results of performance calculations in terms of the distributions of local species, velocity, temperature and current density, under different operating conditions are presented and discussed in detail. The results show the influence of mass transport-inhibition by mechanical compression of the gas diffusion layers under the ribs on the local gas partial pressure, as well as on the current density distribution. Furthermore it is shown that, under the present situation, the description of the diffusion species in the gas diffusion layer, by means of a Maxwell-Stefan formulation, is essentially the same as one by means of the Wilke approach. The macrohomogeneous approach for the description of electrochemistry in the catalyst layer, desrcibed in the second model, results in a more homogeneous current density distribution compared to the surface-oriented approach from model 1. The significance of water transport through the membrane from the cathode side to the anode side is also described and discussed. Phosphoric acid concentrations, which are caused by water production and water transport, differ on the anode and cathode sides of the membrane. On the anode-side boundary surface between the membrane and catalyst layer, a 95.3% phosphoric acid concentration is observed. On the cathode side, a value of 93.9% is obtained. These results are in good agreement with experimental data.

Modellierung von Hochtemperatur-Polymerelektrolyt-Brennstoffzellen

von Qing Cao

Kurzfassung

Brennstoffzellen sind Energiewandler die durch elektrochemische Reaktionen von Wasserstoff und Sauerstoff Strom und Wärme erzeugen. Sie werden nach den verwendeten Elektrolyten und den Betriebstemperaturen in verschiedene Typen eingeteilt. Ein vielversprechender Brennstoffzellentyp, der als Bordstromversorgung in Lastkraftwagen oder Flugzeugen eingesetzt werden kann, ist die Hochtemperatur-Polymerelektrolyt-Brennstoffzelle (HT-PEFC). In einer HT-PEFC wird phosphorsäure-dotiertes Polybenzimidazol als Elektrolyt eingesetzt. Die typische Arbeitstemperatur dieses Brennstoffzellentyps liegt zwischen 150 ℃ und 180 ℃.

Ziel dieser Arbeit ist die 3D-Modellierung von HT-PEFC auf Zellebene, um das Verständnis der physikalischen und elektrochemischen Prozesse innerhalb der Zelle besser zu verstehen. Als Basis für die Modellentwicklung kommt die Open-Source Software OpenFOAM zur Anwendung. Vier Modelle wurden implementiert, um verschiedene Phänomene beschreiben zu können.

- Im ersten Modell wird die Elektrochemie mit effektiven auf die geometrische Fläche der Katalysatorschicht bezogenen Parametern beschrieben. Der Stofftransport durch die poröse Gasdiffusionslage wird durch einen Fickschen Diffusionsansatz dargestellt.

- Das zweite Modell verwendet einen makrohomogenen Ansatz zur Beschreibung der Elektrochemie wodurch die Eindringtiefe der elektrochemischen Reaktion in der Katalysatorschicht als Funktion der Stromdichte berücksichtigt werden kann.

- Die Beschreibung des Wassertransportes von der Kathodenseite zur Anodenseite durch die phosphorsäuredotierte Polybenzimidazolmembran während des Brennstoffzellenbetriebs wird im dritten Modelle abgebildet.

- Das vierte Modell vergleicht den Gastransport in den Gasdiffusionsmedien, beschrieben durch einen Stefan-Maxwell Ansatz, mit dem Gastransport entsprechend Modell 1.

Die in der Arbeit entwickelten mathematischen Modelle wurden durch Vergleich der numerischen Simulationsergebnisse mit experimentellen Daten und analytischen Lösungen validiert. Zwei verschiedene Zellgeometrien wurden betrachtet: Eine Zelle mit parallelen geraden Kanälen, einer aktiven Fläche von 0,2 cm^2 und eine 50 cm^2 -Zelle mit mäandrierenden Kanälen. Die Simulationsergebnisse der lokalen Spezies-, Geschwindigkeit-, Temperatur- und Stromdichteverteilung bei verschiedenen Betriebsbedingungen werden vorgestellt und detailliert diskutiert. Die Ergebnisse zeigen den Einfluss der stofftransporthemmenden Kompression der Gasdiffusionslagen unter den Stegen sowohl auf die lokale Gaspartialdruckverteilung als auch auf die Stromdichteverteilung. Weiterhin wird gezeigt, dass unter den vorliegenden Betriebsbedingungen die Beschreibung des diffusiven Stofftransportes in der Gasdiffusionslage, im Rahmen einer Maxwell-Stefan-Formulierung, einer Beschreibung mittels eines Wilke Ansatzes äquivalent ist. Der im zweiten Modell entwickelte makrohomogene Ansatz zur Beschreibung der Elektrochemie in der Katalysatorschicht resultiert in einer homogeneren Stromdichteverteilung im Vergleich zu dem flächenbezogenen Ansatz aus Modell 1. Die Relevanz des Wassertransportes durch die Membran von der Kathodenseite zur Anodenseite wird ebenfalls demonstriert. Die sich aufgrund der Wasserproduktion und des Wassertransportes einstellende Phosphorsäurekonzentrationen unterscheiden sich auf Anoden- und Kathodenseite. An der anodenseitigen Grenzfläche von Membran und Katalysatorschicht ist eine 95,3 prozentige Phosphorsäurekonzentration beobachtbar. Auf der Kathodenseite ergibt sich ein Wert von 93,9%. Diese Ergebnisse stimmen qualitativ gut mit experimentellen Daten überein.

Contents

1 Introduction **9**

1.1 Motivations and objectives . . . 9

1.2 Organization of this thesis . . . 12

1.3 Working principle and components of the HT-PEFC . . . 13

1.4 Thermodynamic and polarization curve . . . 17

1.5 Classification of the flow of an HT-PEFC . . . 20

1.6 Literature review . . . 23

1.6.1 Modelling work . . . 23

2 Modelling aspects **29**

2.1 Assumptions and computational domain . . . 30

2.1.1 Assumptions . . . 30

2.1.2 Computational domain and operating conditions . . . 31

2.2 Basic model (model I) . . . 35

2.3 Macro-homogeneous model (model II) . . . 44

2.4 Water transfer model (model III) . . . 50

2.5 Multicomponent diffusion model using Maxwell-Stefan equations (model IV) . . . 57

2.6 Discretization methods . . . 61

3 Numerical results **65**

3.1 Mesh independence study . . . 65

3.2 Simulations with the single channel pair . . . 68

3.2.1 Basic model (model I) . . . 68

3.2.2 Compression effect of GDL (model I) . . . 87

3.2.3 Multicomponent diffusion model (model IV) . . . 97

3.3 Simulations with the single cell with serpentine flow field . . . 107

3.3.1 Basic model (model I) and Macro-homogeneous model (model II) . . . 107

3.3.2 Water transfer model (model III) . . . 116

4 Discussion **125**

5 Conclusion **129**

6 Appendix **131**

6.1 Experimental data for the parameter fitting of Model I and II 131

6.2 Experimental data for the parameter fitting of Model III 132

6.3 Derivation of the matrix form of Maxwell-Stefan relationship 134

6.3.1 Basic equaitons 134

6.3.2 Molar-based matrix form of Maxwell-Stefan relationship 136

6.3.3 Mass-based matrix form of Maxwell-Stefan relationship with respect of gradient of molar fraction 138

6.3.4 Relationship between gradient of mass fraction and gradient of molar fraction 140

6.3.5 Mass-based matrix form of Maxwell-Stefan relationship with respect of gradient of mass fraction 141

References **143**

Acknowledgments **173**

1 Introduction

1.1 Motivations and objectives

Since the industrial revolution, the major energy source of human industry has been fossil fuels. In recent years, with the development of industry and the increasing of population, two aspects of the energy crisis have been performed: 1) energy shortage, which is caused by continuous consumption of fossil fuels [1]; 2) climate change, which is caused by dramatically increasing of the greenhouse gases emission [2].

As a clean energy-converting device, the fuel cell has attracted considerable attention over the past decade. As a membrane reactor, fuel cell directly converts the chemical energy into the electrical energy through the electrochemical reaction. It ensures a stable supply of energy and has been used in many applications, such as portable, mobile and stationary power generation. Compared to the classic power sources, such as internal combustion engine (ICE), fuel cell shows the following advantages: 1) the process of the fuel cell is not restricted to the Carnot cycle; it means that fuel cell has a higher efficiency than ICE; 2) fuel cell doesn't have moving parts, it means that fuel cell operates silently and the maintenance is simple; 3) if the pure hydrogen is utilized as fuel for the fuel cell, the only products are water and heat, there is no emission of greenhouse gas.

According to the different electrolyte and operating temperature, fuel cell can be classified in many varieties: alkaline fuel cell (AFC), direct methanol fuel cell(DMFC), proton exchange membrane fuel cell (PEFC), phosphoric acid fuel cell (PAFC), molten carbonate fuel cell (MCFC), solid oxide fuel cell (SOFC), etc.

In the application area of mobile power supply, the industry shows a keen interest of PEFC. In 2015, Toyota and Hyundai began selling numbers of PEFC vehicles on the market. These vehicles operate with PEFC-battery systems. PEFC stack produces electricity from pure hydrogen for driving the electromotor; battery stores electricity recovered during deceleration, and then adds to the output during acceleration. Nevertheless, in the case of vehicles, the produce, distribute, store of hydrogen are major issues [3]. The infrastructure of hydrogen in most of the countries like Germany is under development. It can be expected that the petroleum-based fuels, such as diesel and kerosene, are still the primary sources of energy for vehicles, ships, and aircraft in short to medium term.

For using the petroleum-based fuels more efficiently and improve the idling efficiency of ICEs, the fuel-cell-based auxiliary power units (APU) is proposed as an attractive bridge technology. Through an on-board fuel reformer, the liquid fuel is converted into reforming gas. The reforming gas contains besides H_2 mainly H_2O, CO_2, N_2 and CO [4, 5]. However, the CO molecules can adsorb on the surface of Pt and decrease the performance by blocking the active sites [6, 7]. In the case of PEFC, the feed gas can poison the Pt/C catalyst with only 5-10 ppm CO [8]. Therefore, the operating of PEFC-based APU requires high-quality gas cleaning devices to remove the CO. That brings a high system complexity.

Furthermore, the water management is a delicate issue of PEFC. In the case of bad water management, the Nafion membrane might be dehydrated, or the gas diffusion layers and gas channels might be flooded. It fetches the decreasing of the performance and stability of the system.

An alternative technology is high-temperature polymer electrolyte fuel cell (HT-PEFC) based APU. The idea of HT- PEFC is to take both benefits of PEFC and the classical phosphoric acid fuel cells (PAFC) and leave their weaknesses. HT-PEFC has the similar structure with PEFC and uses the phosphoric acid-doped polymer as the electrolyte. This device has an operating temperature between 150 ℃ and 180 ℃ [9, 10] and shows several advantages compared to PEFC:

- It has a higher CO tolerance than PEFC. Under the typical operation temperatures the CO tolerance of HT-PEFC is around 1-2% [11].
- There is no flooding of water in gas channels and porous layers.
- Humidification is not required [12].
- The membrane has a promising proton conductivity at the temperature above 100 ℃ [13].

HT-PEFC based APU systems designed for using diesel and kerosene are developed in Juelich. These systems contain besides HT-PEFC stack mainly the autothermal reformer, the water-gas shift reactor, and the catalytic burner. Compared to the PEFC system, the HT-PEFC system shows a much simpler system design. The net system efficiency of the HT-PEFC based APU system is in the order of 22% [5], which is higher than the conventional, ICE-powered APUs (in the order of 10%-20%) [14].

The goal of the present thesis is the 3D-modelling of HT-PEFC on cell level by using the computational fluid dynamics (CFD) technology, to improve the understanding of the physical phenomena in the cell and make the contribution to the development and optimisation of HT-PEFC. For achieving this goal, four models are developed in this thesis: a basic model and three extend models. In the basic model, through calculations of conservation of mass-, momentum-, species and heat transfer, the temperature, the pressure, the velocity of the gas mixture and the distribution of the species in the gas channels and GDLs are characterised. Meanwhile, the electrochemical equations are implemented at the interface between the MEA and the GDL, to allow for calculations of the overall electrical performance and the local current density distribution of the cell.

The other three models are respectively focussed on the transport losses of oxygen and protons in the catalyst layer, the water cross over in the membrane and the multicomponent diffusion in the GDL and gas channels. These models provide the advanced understanding of the mass transfer of the HT-PEFC.

An open source software (OpenFOAM [15]) based on finite volume method is employed for implementing the models. It provides high transparency and extensibility. The workflow of the modelling work contains mainly four steps: 1) establish the mathematical models; 2) establish the geometries and meshes; 3) solve the transport equations using OpenFOAM; 4) visualisation, validation and analysation of the results.

1.2 Organization of this thesis

This thesis is organised as follows:

In Chapter 1, the working principle, the components, the thermodynamic and the polarisation curve of the HT-PEFC are introduced. Additionally, the state of the research of PEFC/HT-PEFC modelling is reviewed.

In Chapter 2, the governing equations are introduced in detail. Four models are presented in this chapter: a basic model, a macro-homogeneous model, a water transfer model and a multicomponent diffusion model. The 3D geometries, meshes, boundary conditions and discretization methods are also shown in Chapter 2.

The numerical results are presented in Chapter 3:

Section 3.1 presents the mesh independence studies of the single-channel mesh and the serpentine mesh.

Section 3.2 contains the results of the simulations with the single channel pair. The results of the basic model and the multicomponent diffusion model are shown. The numerical study of compression effect of GDL is also presented.

Section 3.3 contains the results of the simulations with the single cell with serpentine flow field. The basic model and the macro-homogeneous model are validated and compared. The performance of the water transfer model is also shown.

Chapter 4 presents the discussion of the numerical results.

Chapter 5 contains the conclusions of this thesis.

Appendix introduces the experimental data used for the parameter fitting and the mathematical derivation of the matrix form of Maxwell-Stefan relationship.

1.3 Working principle and components of the HT-PEFC

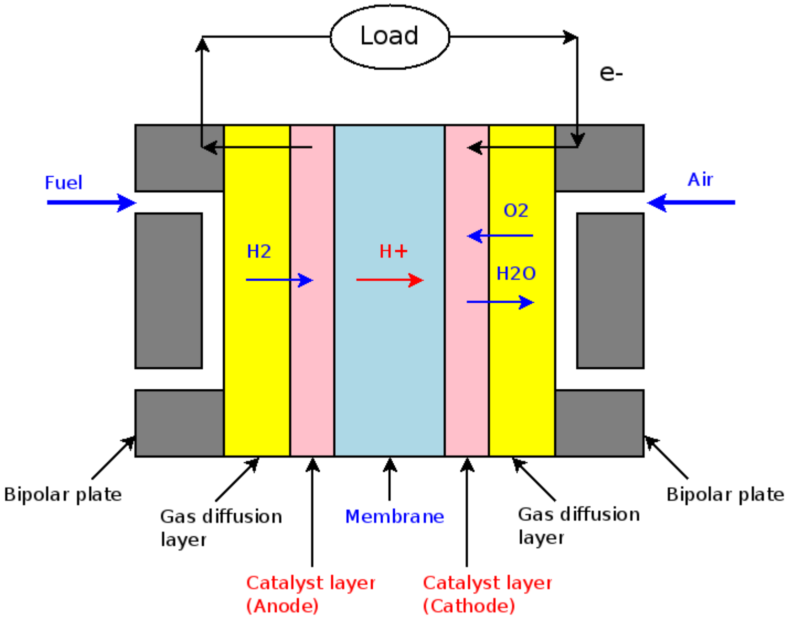
Load
e-
Fuel
Air
H2
H+
O2
H2O
Bipolar plate
Gas diffusion layer
Membrane
Gas diffusion layer
Bipolar plate
Catalyst layer (Anode)
Catalyst layer (Cathode)

Figure 1.1: The basic structure of HT-PEFC.

The basic structure of an HT-PEFC is presented in Figure 1.1. As shown, HT-PEFC mainly consists of bipolar plates (BPPs), Gas diffusion layers (GDLs), catalyst layers (CLs) and a phosphoric acid doped membrane. It is worth to note that, other necessary hardware of an HT-PEFC such as current collectors, coolant supplies and gaskets are not shown in Figure 1.1, and they are also not implemented in the modelling work.

When the HT-PEFC is running, the fuel and air are delivered through the gas channels. Then the gases move through the porous GDL to catalyst layers. In the anode catalyst layer, a hydrogen molecule splits into two protons and two electrons. These protons move further through the membrane to the cathode side. In the cathode catalyst layer, the protons react with oxygen and produce water. The generated electrons flow through an external circuit from the anode to the cathode. The electrochemical reactions are as follows:

Anode reaction:

$$\mathrm{H_2 \rightarrow 2\,H^+ + 2\,e^-} \tag{1.1}$$

Cathode reaction:

$$\frac{1}{2}\,\mathrm{O_2} + 2\,\mathrm{H^+} + 2\,\mathrm{e^-} \rightarrow \mathrm{H_2O(g)} \tag{1.2}$$

Overall reaction:

$$\mathrm{H_2} + \frac{1}{2}\,\mathrm{O_2} \rightarrow \mathrm{H_2O(g)} \tag{1.3}$$

Reaction 1.1 is called hydrogen oxidation reaction (HOR) and Reaction 1.2 is called oxygen reduction reaction (ORR). The cell performance is strongly limited by the kinetics of ORR and the mass transfer (proton and oxygen) in ORR reaction zone [16, p.11].

The functionalities and the physical properties of the components of HT-PEFC are introduced in the following paragraphs.

Bipolar plates Bipolar plates provide space for gas channels and electrical pathway. The material of bipolar plates must satisfy the following requirements: 1) high electric conductivity, to minimize the electrical loss; 2) high chemical stability, to avoid the corrosion caused by acid; 3) mechanical strength, to prevent the damage under stress; 4) impermeability to gases, to prevent the gas leakage. A reliable material is a graphite composite material. Most of our in-house cells use graphite as bipolar plates.

Figure 1.2 displays two typical graphite bipolar plates with serpentine flow field design. However, graphite brings two drawbacks: 1) for series production, graphite brings additional processing cost compared with metal; 2) the porous structure of graphite can uptake a part of phosphoric acid that is originally in the membrane [17]. That limits the cell performance and durability.

An alternative device is a metallic bipolar plate. It requires the coating of bipolar plates. Without coating the corrosion effect becomes critical, and a passive layer will be built on the surface of the plates and will reduce the electrical conductivity dramatically [18].

Gas diffusion layer The GDL allows the reactant gas to move to the reaction zone by the diffusion and convection. The generated water can also pass through the GDL into the gas channels. Additionally, the GDL provides the electrical contact, and the electrons can pass through the GDL to bipolar plates. The GDL normally consists of carbon fiber paper (Figure 1.3), which can be considered as a porous solid matrix. The diameter of one carbon fiber is typically less than 10 µm, and the thickness of the whole carbon paper is in the range from 100 µm to 300 µm [19]. The GDL applied in the Jülich HT-PEFC is a commercial one with the thickness of 257 µm.

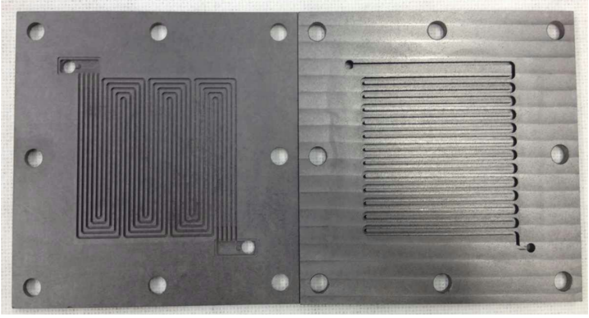

Figure 1.2: Graphite bipolar plates of the single cells for laboratory testing.

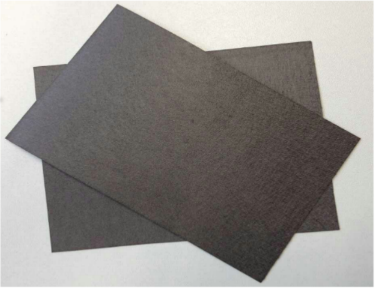

Figure 1.3: Photograph of a GDL used in HT-PEFC.

When the GDL is mounted in HT-PEFC, some material properties will locally change due to the mechanical stress. Figure 1.4 shows the SEM photo of a channel-rib scenario of a GDL embedded in a fuel cell. One can see that the thickness of the GDL under the ribs are smaller than the GDL under the channels. The porosity and permeability under the ribs also changed correspondingly.

Catalyst layer Two catalyst layers (anode CL and cathode CL) are located between the GDLs and the membrane. The combination of the CL and the GDL is known as the gas diffusion electrode (GDE). The catalyst layers consist of the catalyst, catalyst supports, and binders. The catalyst of HT-PEFCs can be pure Platinum (Pt), or Pt alloy. In recent years, Pt alloy attracted much attention due to its economical cost and excellent stability [20, 21], although pure Pt still shows a higher activity for HT-PEFC. Carbon blacks are usually used as the catalyst support, and the polytetrafluoroethylene (PTFE) are typically used as the binder for HT-PEFC. The thickness of CL is in the range from 20 µm to 120 µm [22, 23]. The diameter of the Pt/C

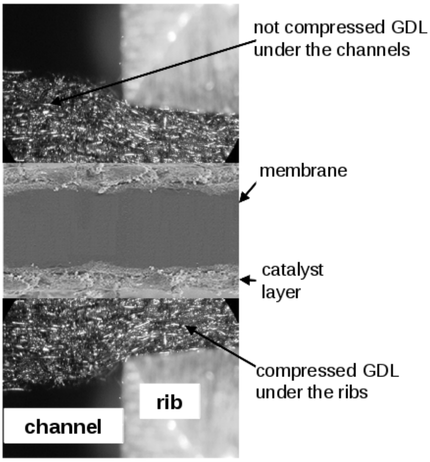
not compressed GDL under the channels
membrane
catalyst layer
compressed GDL under the ribs
rib
channel

Figure 1.4: Channel-rib scenario of a GDL embedded in a fuel cell. Reprinted from [19], with the permission from Elsevier.

particles applied in the Jülich HT-PEFC is 2.7 nm.

Membrane The membrane offers a pathway for protons from the anode to the cathode. It also prevents any gas passing through the MEA. The composition of the membrane is a thermoplastic polymer doped with the concentrated phosphoric acid. The polymer is typically poly(2,2'-m-phenylene-5,5'-bibenzimidazole) (PBI), which has an excellent chemical and thermal stability and mechanical strength. The melting point is above 600 ℃ [24]. Previous studies show that the proton conductivity of the phosphoric acid-doped PBI membrane reaches maximum in the range of 85 wt % (weight percent) of phosphoric acid [13, 25]. The thickness of a dry PBI-membrane is in the range from 30 µm to 100 µm [13, 26, 27]. One alternative of the PBI membrane is the poly(2,5-benzimidazole) (ABPBI) membrane. The membrane employed in the Jülich HT-PEFC is the phosphoric acid doped ABPBI membrane, which is offered by company Fumatech. The thickness of this membrane is in the range from 50 µm to 60 µm. The thermal stability is up to 500 ℃. The chemical structures of PBI and ABPBI are presented in Figure 1.5:

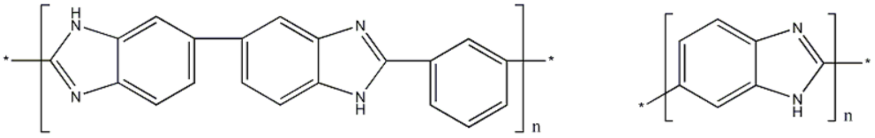

Figure 1.5: Chemical structures of PBI (left) and ABPBI (right).

1.4 Thermodynamic and polarization curve

Thermodynamiclly, the enthalpy change for a chemical reaction of HT-PEFC can be expressed as [28, p.20]:

$$\Delta H = \Delta G + T\Delta S \tag{1.4}$$

where
ΔH = enthalpy change of a reaction (kJ mol^{-1})
ΔG = Gibbs free energy change of a reaction (kJ mol^{-1})
T = reacting temperature (K)
ΔS = entropy change of a reaction (kJ mol^{-1} K^{-1})

Maximum theoretical efficiency (thermodynamic efficiency) of HT-PEFC is defined by:

$$\eta_{max} = \frac{\Delta G}{\Delta H} \tag{1.5}$$

where
η_{max} = thermodynamic efficiency (-)

For reaction of HT-PEFC (Reaction 1.3) under the standard condition (i.e., 1 atm and 298 K), the thermodynamic efficiency of HT-PEFC is defined by:

$$\eta^0_{max} = \frac{\Delta G^0}{\Delta H^0} \tag{1.6}$$

where
η^0_{max} = thermodynamic efficiency under the standard condition (-)
ΔG^0 = Gibbs free energy change of a reaction under the standard condition (kJ mol^{-1})
ΔH^0 = enthalpy change of a reaction under the standard condition (kJ mol^{-1})

Under the standard condition, ΔG^0 equals to -228.6 kJ mol^{-1}, ΔH^0 equals to -241.8 kJ mol^{-1} for water vapor. Maximum theoretical efficiency reaches 94.5 %, which is much higher than the efficiency of a heat engine.

When all the Gibbs free energy of Reaction 1.3 is converted to electrical energy, the thermodynamic voltage of HT-PEFC under the standard condition is defined as:

$$E_{th}^{0} = \frac{\Delta G^{0}}{2F} \tag{1.7}$$

where
E_{th}^{0} = thermodynamic voltage of a reaction under the standard condition (V)
F = Faraday constant (C mol^{-1})

However, the majority of the operating conditions of HT-PEFC are not the standard condition. The theoretical open-circuit voltage of the HT-PEFC, also known as Nernst voltage, is a function of temperature and pressure:

$$E_{Nernst} = \frac{-\Delta G^{T}}{2F} - \frac{RT}{2F}\ln\left(\frac{\widetilde{p}_{H_2O}}{\widetilde{p}_{H_2}\widetilde{p}_{O_2}^{0.5}}\right) \tag{1.8}$$

where
E_{Nernst} = Nernst potential (V)
ΔG^{T} = Gibbs free energy change of a reaction at the operating temperature (kJ mol^{-1})
$\widetilde{p}_{H_2O}$, $\widetilde{p}_{H_2}$, $\widetilde{p}_{O_2}$ = normalized partial pressure (p_i / p_0) of H_2O, H_2 and O_2 (-)

In practice, the cell voltage is not equal to the Nernst voltage, since there are voltage losses during the operation. The plot of cell voltage against current density is called polarisation curve, which is the standard method for characterising the performance of an HT-PEFC. A typical polarisation curve is shown in Figure 1.6.

The voltage losses can be classified into three categories: the activation overpotential, the ohmic overpotential and the concentration overpotential. The cell voltage is therefore written as [29, p.70]:

$$E_{cell} = E_{Nernst} - \eta_{act} - \eta_{ohm} - \eta_{conc} \tag{1.9}$$

where
E_{cell} = cell voltage (V)
η_{act} = activation overpotential (V)
η_{ohm} = ohmic overpotential (V)
η_{conc} = concentration overpotential (V)

η_{act} is caused by overcoming the activation energy barrier of the chemical reaction, which can occur at both anode and cathode. Since the oxygen reduction at the cathode (ORR) is much slower than the hydrogen oxidation at the anode (HOR), the activation overpotential occurs mainly at the cathode.

η_{ohm} is caused by ohmic resistance, which results mainly from: 1) resistance to the flow of electrons through the electrodes, GDLs, BPPs and interconnections; 2) resistance to the flow of protons through the electrolyte.

η_{conc} is caused by the concentration polarisation, which appears from the decrease in concentration of the reactants. This concentration polarisation can cause a rapid drop in cell voltage at high current density.

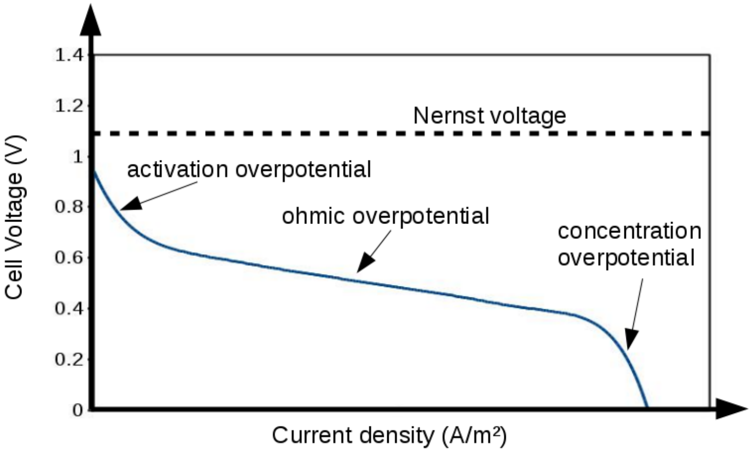

Figure 1.6: Schematic diagram of a polarization curve and losses of HT-PEFC.

1.5 Classification of the flow of an HT-PEFC

Before we build the numerical models of the HT-PEFC, several questions should be answered first to allow us to pick the right physical approach:

1. Is the flow steady or transient?
2. Is the flow in continuum state?
3. Is the flow laminar or turbulent?
4. Is the flow compressible or incompressible?

The answer to the above questions are listed as follows:

For question 1 During the most working time of an HT-PEFC system, the velocity of flow does not change with time due to the dynamic equilibrium of the chemical reaction and the mass transport. It means that the flow is in steady state, and the transient terms are not necessary to be included in the governing equations. In some special processes with the small time scale, for instance, start-up, the flow is dependent on the time. However, these special cases are not considered in this thesis.

For question 2 For the flow in the HT-PEFC, a dimensionless number, Knudsen number, is used to determine that if the flow is in continuum state:

$$\mathrm{Kn} = \frac{\lambda}{l_g} \tag{1.10}$$

where

Kn = Knudsen number (-)
λ = mean free path of the molecules (m)
l_g = geometric characteristic length (m)

In the porous media of an HT-PEFC, l_g is the pore diameter. The mean free path λ is estimated from [30, p.194]:

$$\lambda = \frac{k_B T}{\sqrt{2}\pi\sigma^2 p} \tag{1.11}$$

where
k_B = Boltzmann constant (J K^{-1})
σ = collision diameter of the diffusing species (m)

Generally speaking, the flow is considered as continuum only when Kn < 0.01. For the flows with the Kn > 0.01, they are classified to 3 classes: slip flow (0.01 < Kn < 0.1), transition flow (0.1 < Kn < 10) and free-molecule flow (Kn > 10) [31, p.3]. In these cases, the continuum assumption is not a good approximation any more, and the statistical methods should be employed.

Table 1.1 presents the approximations of Knudsen numbers of different HT-PEFC species in the GDL applied in the Jülich HT-PEFC. As shown in Figure 1.3, since the porous structure is made by randomly stacked carbon fibers, only effective pore diameter can be used for estimation of the Knudsen number. The values of σ are taken from literature [32, p.224] and λ is according to Equation 1.11. As shown in Table 1.1, the Knudsen numbers are below 0.01, which means the flow in GDL can be considered as continuum.

For the flow in the channel, l_g is the characteristic length of the channel, which is in millimeter range. That means the Knudsen numbers of the gas flow in the channel is around two orders of magnitude higher than that in the GDL. Therefore, the flow in the channel can be also considered as continuum.

Table 1.1: Knudsen numbers of HT-PEFC species in GDL, T= 160 ℃, l_g = 20 µm.

Species	σ (m)	λ (m)	Kn
H_2	2.92×10^{-10}	15.63×10^{-8}	0.0088
O_2	3.47×10^{-10}	11.27×10^{-8}	0.0050
N_2	3.80×10^{-10}	9.88×10^{-8}	0.0047
H_2O (g)	2.64×10^{-10}	8.32×10^{-8}	0.0054
CO_2	3.94×10^{-10}	20.91×10^{-8}	0.0031

For questions 3 and 4 In the scope of fluid mechanics, Reynolds number is used to determine if a flow is laminar or turbulent. The Reynolds number is defined as:

$$\mathrm{Re} = \frac{v\rho L}{\mu} \tag{1.12}$$

where
Re = Reynolds number (-)

v = velocity of the fluid (m s^{-1})
ρ = density of the fluid (kg m^{-3})
L = hydraulic diameter (m)
μ = dynamic viscosity of the fluid (Pa s)

For pipe flow, the critical Reynolds number is about 2300 [33, p.117]. It means when this number is smaller than 2300, the flow can be treated as laminar flow.

Another dimensionless quantity, Mach number, is used to determine if a flow is compressible or incompressible:

$$\mathrm{Ma} = \frac{v}{c} \tag{1.13}$$

where
Ma = Mach number (-)
c = speed of sound in the medium (m s^{-1})

When the Mach number of the flow is smaller as 0.3 [34, p.33], the flow can be treated as the incompressible flow.

The hydraulic diameter L in rectangular channels in Equation 1.12 is defined as:

$$L = \frac{2ab}{a+b} \tag{1.14}$$

where
a = width of the channel (m)
b = height of the channel (m)

Since the cross-sections of the channels in this thesis are always 1 mm×1 mm, L equals 1 mm. At 160 ℃, the denstiy of air is estimated as 0.80 kg m^{-3} and the dynamic viscosity of air is estimated as 2.45×10^{-5} Pa s; the density of hydrogen is estimated as 0.06 kg m^{-3} and the dynamic viscosity of hydrogen is estimated as 1.15×10^{-5} Pa s [35].

Table 1.2 shows Reynolds numbers and Mach numbers at the inlets of the gas channels of our in house single cells with an active area of 50 cm^2 under several mean current densities. The pure hydrogen is used as fuel, and the chemical stoichiometry is 2/2. Easy to find that for all of the operating points, the flow in the gas channel can be always considered as laminar and incompressible.

Table 1.2: Reynolds numbers and Mach numbers at the inlets of anode side and cathode side under different operating conditions of a HT-PEFC

Current density (Am^{-2})	Re, anode	Re, cathode	Ma, anode	Ma, cathode
2000	3.4	55.6	0.0005	0.004
4000	6.9	111.2	0.001	0.008
6000	10.3	166.7	0.0015	0.012

1.6 Literature review

The first PBI/H_3PO_4 system was introduced by Wainright et al. [13]. In that work, polybenzimidazole membrane doped with phosphoric acid was first used as polymer electrolyte of fuel cells. The experiment showed that the proton conductivity was related to water vapour activity and temperature. After that the PBI based high-temperature polymer electrolyte fuel cell has attracted much attention. Many experimental works were published to research the cathode kinetics [36], CO tolerance [37], heat and water management [38], stack performance [39], membrane conductivity [40] and degradation [41] of HT-PEFC. On the other hand, numerous models were developed to understand the physical processes. In the following sections, an overview of PEFC/HT-PEFC models is presented.

1.6.1 Modelling work

Non-CFD model

The pioneering PEFC modelling work was done by Springer et al. [42] from Los Alamos National Laboratory in 1991. They provided an isothermal, 1-D steady state model for PEFC with Nafion membrane. The equilibrium between liquid and gas phase of water, the liquid water diffusion and the electro-osmotic drag were considered. This work showed the importance of water management for PEFC. In the same year, Bernardi et al. [43] published their PEFC model, which is based on the macro homogeneous electrode model [44] and for isothermal, 1-D steady state. This work focused on the cell polarisation, water transfer and catalyst utilisation. It should be pointed out that the driving force of water transfer in Bernardi's model was the pressure gradient, and the driving force of water transfer in Springer's model was the concentration gradient. Additionally, the membrane in Bernardi's model was assumed to be fully hydrated, which is not true in Springer's model. Two years later, Fuller and Newman [45], Nguyen and

White [46] published 2-D models on water and thermal management of PEFC. These models discussed in more detail about the water and heat management than Springer/Bernardi's model. Around the same time, Kim et al. [47] simulated the polarisation curve using an empirical equation. West et al. reported the channel-rib effect with their 2-D model [48]. Since 1998, Perry et al. [49] and Eikerling et al. [50] developed independently the 1-D mass transport model in gas-diffusion electrodes, which reported the limiting effects of the catalyst layer. Woehr et al. [51] and van Bussel et al. [52] published dynamics models, which allowed to simulate the transient state after the change of operating conditions. Bultel et al. [53] provided a model of PEMFC electrodes at the particle level. Baschuk et al. [54] developed a membrane model to study the water flooding effect. Weber et al. [55] developed transport model in polymer electrolyte membranes, to describe the structural changes in the membrane due to water content. The model from Chan et al. [56] considered the anode CO kinetics, in which the CO poisoning was explained.

In 2008, Korsgaard et al. [57] published an empirical model of the reforming-based HT-PEFC system. The numerical results show that the total energy utilisation efficiency of this system is better than the PEFC based system. Two years later, Shamardina et al. [58] developed a 2-D analytical model of HT-PEFC, the crossover effect of reactant gases through the membrane was analysed.

In recent years, Kulikovsky et al. published several paper [59–61] on advanced modelling of cathode catalyst layer performance, which was based on the macro homogeneous approach and could be used as a diagnostic tool for PEFC. This group also [59] provided a parametric model to simulate the polarisation curve of HT-PEFC.

CFD model

Since 2000, many PEFC and HT-PEFC models based on CFD were published. By modelling with CFD, two methods were usually employed to solve the governing equations: the finite volume method (FVM) and the finite-element method (FEM). Both of these two methods can convert partial differential equations to linear algebraic equations. In these two methods, meshes are required to discrete the volume and store the local information.

Many commercial CFD software are based on FVM, for instance, FLUENT, STAR-CD and PHOENICS. These software provide a set of proven methods to solve the conservation equations, which can be used to simulate the mass transfer and heat transfer of fuel cells. On the other hand, the commercial software COMSOL, which is based on FEM, also provides a fuel cell simulation module.

PEFC The early CFD based modelling work on PEFC was published by Gurau et al. [62] in 1998. In this paper, a 2-D CFD model was provided to solve the Navier-Stokes equations, continuity, energy and mass transfer equations. The polarisation curve was validated with experiment data [63]. In this work, it is assumed that there is no liquid water in the gas channels and GDLs. In the same year, Djilali et al. [64] reported another CFD model for heat and mass transport in PEFC. In 2000, Um et al. [65] provided further a transient, 2-D CFD model and also validated using the data from [63].

In 2001, Wang et al. [66] published the first CFD-based two-phase flow model. The model was isothermal, and a so-called multiphase mixing approach is used to study the phase change. This model suggested that by high current densities liquid water appears in the porous zone.

Dutta et al. [67] developed the first 3-D CFD model on PEFC in 2001. This model was based on FVM. FLUENT was employed to solve the similar governing equations as [62]; the two-phase flow was not considered. The gas channel was serpentine designed, and the mesh was with $34 \times 200 \times 28$ uniform grid cells. This work focused on the in-plane gas cross over effect.

Mazumder et al. [68] developed a 3-D CFD model to simulate the formation and transport of liquid water and predict their effects on performance. The phase change process was modelled as an equilibrium process. Um et al. [69] also provided a 3-D CFD model based on their previous work [65], the 3-D mass transfer effect was examined. Around the same time, Nguyen et al. [70] provided a 3-D CFD model with the serpentine gas flow channels. The Stefan–Maxwell equations were implemented to solve the multicomponent diffusion. Lum et al. [71] published their work with a steady state, single phase, isothermal 3-D CFD model. The current density along the channel was locally validated. The agglomerate approach was implemented in a 2-D CFD code including liquid water transport by Siegel et al. [72].

Recently, other work of PEFC based on 3-D CFD simulation were published. Shimpalee et al. [73] simulated the flooding effects on cell performance. Hashemi et al. [74] and Cheng et al. [75] focused on 3-D transport effects on the flow fields design. Iranzo et al. [76] calculated the local liquid water distributions and validated it with neutron imaging. Yang et al. [77] coupled the CFD model and optimise technology to optimise the flow fields design.

HT-PEFC Many valuable 2-D and 3-D CFD models of HT-PEFC were developed in the last decade. In 2006, Cheddie et al. presented the first 3-D [78] CFD models of HT-PEFC, where the local distribution of species and the polarisation effects was studied. The flow was single phase due to the operating temperature. The FEM (COMSOL) was employed to solve the mass, momentum, energy, species and charge transfer. The mesh in this work consistent with 3190 elements and the computation time was up to 5 minutes for a single run. The geometry used in this work was a 10mm single-channel cell. The simulated polarisation curve fits the experimental data well. One year later, Cheddie et al. [79] developed further a two-phase model, to simulate the gas solubility in the electrolyte and to consider aqueous phase electrochemical reactions.

Peng et al. [80] developed 3-D transient model accounting for transient transport using FVM (FLUENT). A 235 mm single-channel cell was simulated. The transient responses of local current density, local membrane potential and temperature distribution while cell voltage changes between 0.6 and 0.4 with were discussed. Ubong et al. [81] provided another 3-D model using FEM (COMSOL). They reported that the concentrations overpotential did not appear at high current density, due to the single phase flow. Lobato et al. [82] developed a 3-D model on cell level for studying the influence of flow channel geometry. This study was based on using FEM (COMSOL) and compared the serpentine, parallel and pin-type flow channels. The study showed that the serpentine design had the best performance.

Sousa et al. [83] developed a 2-D isothermal model for studying the influence of the catalyst layer on cell performance. In this work, the agglomerate approach was implemented. The catalyst layers were treated as spherical agglomerates with porous spaces. The phosphoric acid and PTFE were placed between agglomerates. This model examined the effects of the size of agglomerates and phosphoric acid loading on cell performance. Based on this work, the group of Sousa published further [84] a dynamic 2-D non-isothermal model to study the transient response. However, Doubek et al. [85] reported that the agglomerate model did not satisfactorily simulate the activation region of the polarisation curve.

Jiao et al. [86] developed a 3-D non-isothermal CFD model of a single channel cell. The effects of operating temperature, operating pressure, phosphoric acid doping level, inlet relative humidity, and the stoichiometry ratios of the gases on cell performance were researched.

In 2012, Falcucci et al. [87] examined the effects of different channel design on cell performance using 3D-CFD software. Park et al. [88] developed a non-isothermal, quasi-three-dimensional model of the HT-PEFC. One year later, Chippar et al. [89] published a 3-D FEM model of HT-PEFC on the cell level, to investigate the compression/intrusion effect of the GDL. The numerical results showed the maximum stresses in the deformed GDLs occur near the edge of the ribs. The compression/intrusion effect of the GDL increased the spatial non-uniformity in current distributions as well as species. In the same year, Kvesić et al. [90] presented a 3-D CFD model on stack level using FVM (FLUENT). In this work, the volume averaging approach was used to simplify the calculation. A short stack with five cells was simulated. The current densities were locally validated with a segmented measuring plate.

More recently, Krastev et al. [91] developed another 3D CFD model of HT-PEFC on the cell level, the simulation has been carried out by using both pure H2 and Syngas with 2% CO at the anode. The simulated polarisation curve is validated with the experiment. Oh et al. [92] studied the thermal stress in the HT-PEFC using the 3-D FEM simulations. Kazdal et al. [93] published their 2-D model on the vapor-liquid equilibrium of water for HT-PEFC, Hertz-Knudsen equation was used for describing phase change of water. The local concentration of phosphoric acid and the swelling of the membrane could be calculated. However, the vapour pressure of water over the membrane, which is the key parameter of phase change of water, was not given in this paper. Beale et al. [94, 95] developed a 3D CFD model of SOFC based on open-source CFD software. This work provided the object-oriented C++ libraries of fluid flow, heat transfer, electrochemistry and multi-component species transfer. These libraries can be further modified and used in the modelling of HT-PEFC.

Overall, many valuable 2-D and 3-D models of HT-PEFC in cell level or stack level were developed in the last decade. The CFD technology was successfully applied for the modelling of HT-PEFC.

2 Modelling aspects

In the last chapter, the publications of the HT-PEFC modelling are reviewed. However, there are still some lacks on the previous work:

- Little attention has been paid to the diffusion processes. For multicomponent mass transfer, either Fick's law or Maxwell-Stefan equation for calculating diffusion flux has been used, but the difference between these both was not studied.
- There are three main methods for catalyst layer modelling: the surface-related approach, the macro-homogeneous approach [49, 50, 60] and the agglomerate approach. The surface-related approach and the agglomerate approach were implemented in the 3-D CFD models of HT-PEFC in the previous work ([82, 90] and [72, 83]), but the macro-homogeneous approach was never implemented in the 3-D CFD model and compared with the other two.
- The mechanism of water crossover in the membrane was usually neglected, and the phosphoric acid distribution was not calculated in the membrane. A good water transfer model still lacks for HT-PEFC.
- The gas diffusion layer was usually considered as isotropic. It is not true when the GDL is compressed by the bipolar plates. In the scope of the CFD modelling of the HT-PEFC, only [89] has considered this compression effect of the GDL.
- Most of the HT-PEFC CFD models were implemented in commercial codes (FLUENT or COMSOL). The source codes of these model are not publicly available. For other research groups, it is hard to validate, implement and compare with these models.

For filling the research gaps above, in the scope of this thesis:

- The Fick's law and the Maxwell-Stefan equation are implemented and validated in different models. The differences between these two approaches are compared.
- The surface-related approach and the macro-homogeneous approach are implemented and validated in different models. The differences between these two approaches are

compared.

- The crossover effect of the water and the compression effect of the GDL are implemented and validated in different models.
- The open source software OpenFOAM is employed for implementing the models to ensure the transparency and extensibility.

Four mathematical models on cell level are presented: one basic model and three extend models. The basic model (model I) incorporates the simple heat- and mass transfer equations and electrochemistry equations, which is based on Fick's law and the surface-related approach. The crossover effect of the water is not considered. This model can be used to calculate the species distribution and cell performance. The compression effect of the GDL can also be represented using this model. The basic model was based on the open-source C++ code developed by Beale et al. [94–96], and further modified by Keuler [97] and the present author for application to HT-PEFCs. The library of electrochemistry in the basic model is modified according to the kinetic of HT-PEFC. The second model (model II) is a model to describe the effects of mass transfer in catalyst layers on performance, which is based on Fick's law and the macro homogeneous approach. Similar to model I, this model does not consider the crossover effect of the water. The third model (model III) is a water transfer model, which allows people to calculate the water crossover. This model is based on Fick's law and the surface-related approach. The last one (model IV) is a multicomponent diffusion model, which is based on the Maxwell-Stefan equation and the surface-related approach. The crossover effect of the water is not considered in model IV.

Before describing of these four models, the assumptions for those models and computational domains should be mentioned first. These are introduced in the next section.

2.1 Assumptions and computational domain

2.1.1 Assumptions

Due to complex physical phenomena in HT-PEFC, several assumptions were employed to simplify the calculation:

- The cell operates under steady state condition.
- The flow is laminar flow in the gas channels as well as that in the porous GDLs (see

Section 1.5).

- In practice, the temperature of the cell is managed by the heating device and the cooling channels. For simplifying the calculation, those devices are not considered in the models, and the fixed temperature boundary conditions (Dirichlet boundary condition) are assumed on the outer walls of the bipolar plate.
- Overpotential of anode side is assumed to be zero since the kinetics of the hydrogen oxidation at the anode (HOR) are extremely fast compared to the kinetics of the oxygen reduction at the cathode (ORR).

2.1.2 Computational domain and operating conditions

Two geometries are investigated in this work: a single channel pair and a single cell with serpentine flow field. Both meshes encompass five distinct regions: 2 gas regions (air and fuel), one liquid region (electrolyte) and two solid bipolar plates. The structure of an HT-PEFC cell is complex, and therefore only the cross-section of a single channel area is shown to illustrate the composite structure. Three distinct physical domains are considered (see Figure 2.1):

1. the ‘main’ domain composed of all regions, wherein the heat transfer is solved;
2. ‘domain I’, composed of the gas channels and porous GDL, in which mass and momentum transfer are considered;
3. ‘domain II’ in the electrolyte, wherein only mass transfer is solved.
4. the electrochemical reactions are assumed to occur on the electrolyte-GDE interfaces, but different electrochemical models are taken into account.

Dimensions of this geometry are summarized in Table 2.1.

The mesh of the single channel pair is illustrated in Figure 2.2, this geometry is composed of 94400 hexahedral volumes. The active area of this cell is 0.2 cm^2 (2 mm × 10 mm). It is worth to note that, there are two offset zones at the left side (5 mm) and the right side (2 mm) of the active zone. The electrochemical reactions do not occur at the offset zones. The reason of the introducing of the offset zones is that, the simulations with the offset zones present the better mass balances of the species than the simulations without the offset zones. The mesh is an unstructured polyhedral mesh. A pre-processing tool of OpenFOAM ’blockMesh’ was used for the mesh generating.

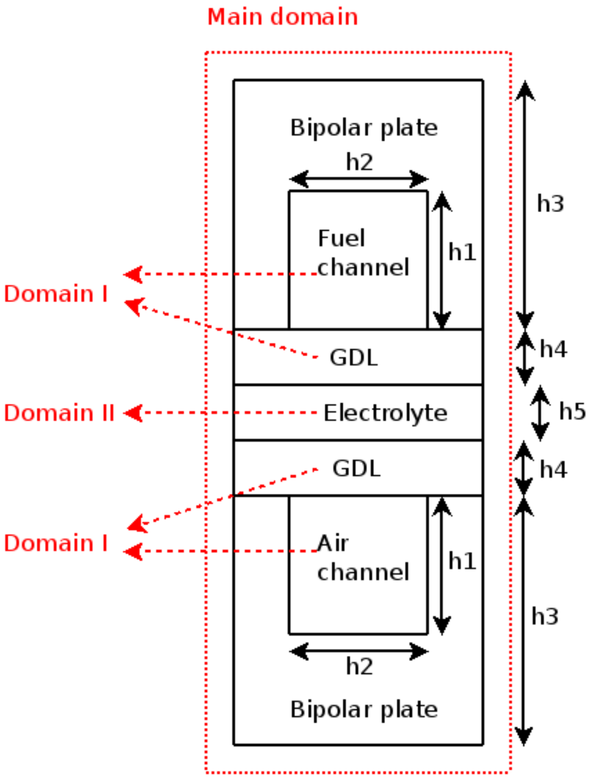
Main domain
Bipolar plate
h2
Fuel channel
h1
h3
Domain I
GDL
h4
Domain II
Electrolyte
h5
GDL
h4
Domain I
Air channel
h1
h3
h2
Bipolar plate

Figure 2.1: Cross-section of a single channel pair.

The single cell is illustrated in Figure 2.3, and corresponds to an existing HT-PEFC cell (Figure 2.4) for which experimental data are being gathered in-house, as part of a fully-integrated program of research. The active area of this serpentine cell is 50 cm^2. The geometry is tessellated with a computational mesh composed of 0.74 million hexahedral volumes. Similar to the single channel pair, this mesh is also an unstructured polyhedral mesh. Due to the complexity of the geometry, the blockMesh can not be used, a third-party open-source pre-processing tool Salome (version 7.2 for Linux platforms) was used for the mesh generating.

Table 2.1: Geometric parameters of composite HT-PFC cell structure.

Parameter	Symbol	Value	Unit
Height of gas channel	$h1$	1×10^{-3}	m
Width of gas channel	$h2$	1×10^{-3}	m
Thickness(total) of bipolar plate	$h3$	4×10^{-3}	m
Thickness of GDL	$h4$	3×10^{-4}	m
Thickness of membrane + CLs	$h5$	2×10^{-4}	m

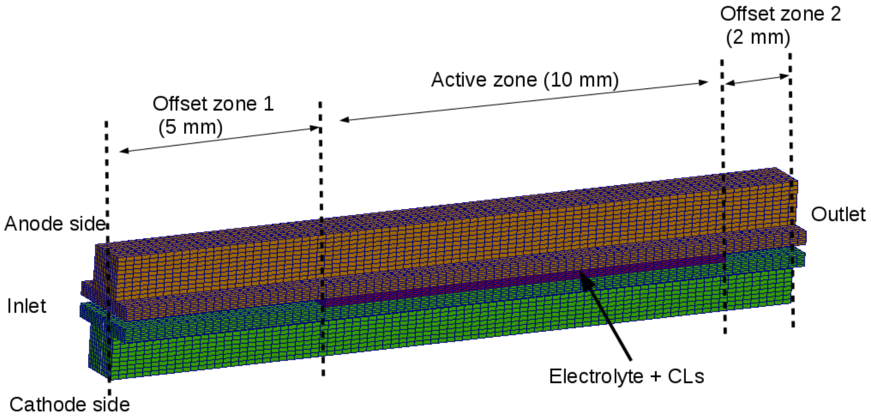
Offset zone 2
(2 mm)
Active zone (10 mm)
Offset zone 1
(5 mm)
Anode side
Outlet
Inlet
Electrolyte + CLs
Cathode side

Figure 2.2: Mesh of single channel pair with 17 mm straight channel (bipolar plates not shown). The active zone is 10 mm, one offset (dead zone) on the inlet side is 5 mm, the other offset (dead zone) on the outlet side is 2 mm. Brown part: channel and GDL at the anode side; green part: channel and GDL at the cathode side; red part: electrolyte and CLs.

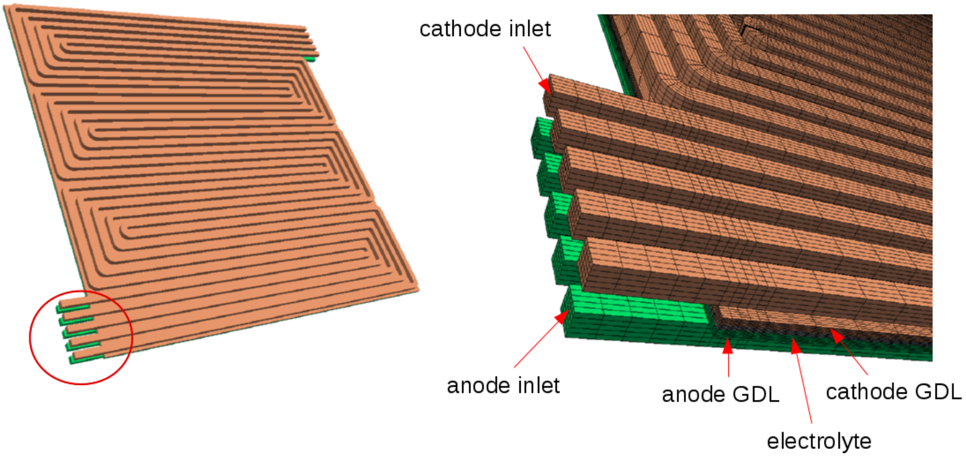
cathode inlet
anode inlet
anode GDL
cathode GDL
electrolyte

Figure 2.3: Left: geometry of single cell with 5-fold serpentine flow field (bipolar plates not shown); right: an enlarged view of inlet area.

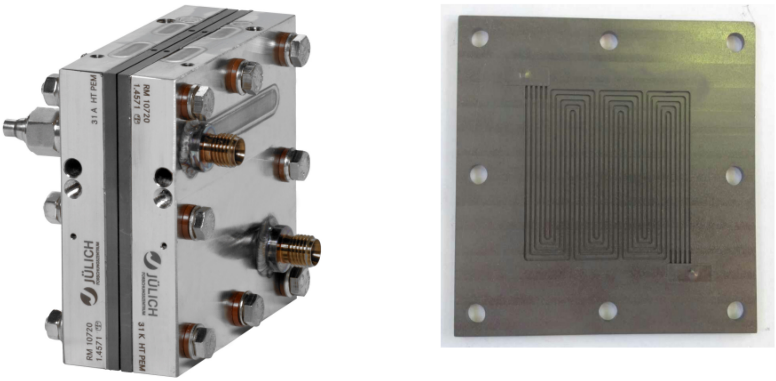
31 A HT PEM
RM 10720
1.4571
JÜLICH
JÜLICH
31 K HT PEM
RM 10720
1.4571

Figure 2.4: Left: the in-house test cell with 5-fold serpentine flow field; right: the bipolar plate of this single cell.

2.2 Basic model (model I)

In this section, the governing equations in the basic model are presented. Since steady state is assumed, all transient terms are neglected in governing equations.

continuity and momentum transfer The continuity- and momentum transfer of the gas mixture are solved in the gas channel and the GDL. Gas mixture is supplied to the gas channels from the inlets of the channels. As mentioned in section 1.5, the flow in the gas channel and the GDL is considered as continuum. Therefore, the conservation of mass of the gas mixture can be solved by solving the continuity equation:

$$\nabla \cdot (\rho \mathbf{U}) = 0 \tag{2.1}$$

where
$\mathbf{U}$ = velocity vector of gas mixture (m s^{-1})
ρ = density of gas mixture (kg m^{-3})

Water is produced while hydrogen and oxygen are consumed. The source/sink term of individual species is given by:

$$S_i = \pm I/(nF) \tag{2.2}$$

where
S_i = source term of species i due to chemical reaction (mol m^{-2} s^{-1})
I = current density (A m^{-2})
F = Faraday constant (C mol^{-1})
n = number of electrons (-)

In the basic model, the chemical reactions are assumed to occur on the boundaries between the GDLs and the electrolyte, the total mass flux equals to the sum of all species flux:

$$J = \sum S_i M_i = \mathbf{U}_b \rho \tag{2.3}$$

where
J = mass flux of the gas mixture on the electrolyte-GDE interface(kg m^{-2} s^{-1})
$\mathbf{U}_b$ = velocity of the gas mixture on the electrolyte-GDE interface, which is perpendicular to the interface (m s^{-1})
M_i = molar mass of species i (g mol^{-1})
ρ = density of gas mixture (kg m^{-3})

Therefore, the boundary velocity at the electrolyte-GDE interface is obtained as:

$$\mathbf{U}_b = \frac{\sum S_i M_i}{\rho} \tag{2.4}$$

This local velocity boundary is updated iteratively during the simulation.

The momentum transfer is governed by a Darcy-modified Navier-Stokes equation:

$$\rho U \cdot \nabla \mathbf{U} - \mu \nabla^2 \mathbf{U} = -\nabla p + R_p \tag{2.5}$$

where
μ = dynamic viscosity of gas mixture (Pa s)
p = pressure of gas mixture (Pa)
R_p = Darcy resistance (Pa m^{-1})

R_p indicates the additional resistance in porous media, which is obtained from the Darcy equation [98]:

$$R_p = -\mu \mathbf{d} \cdot \mathbf{U} \tag{2.6}$$

where
$\mathbf{d}$ = Darcy parameter (-)

The Darcy parameter $\mathbf{d}$ is the inverse of permeability. It is a three-dimensional vector and applies only in the porous media. In the channel, this vector is set to zero in all three directions (x, y and z).

heat transfer The heat transfer is described by the energy conservation equation:

$$\nabla(\rho C_p \mathbf{U} T) - \nabla \cdot k \nabla T = S_h \tag{2.7}$$

Where
C_p = heat capacity (J K^{-1})
T = temperature (K)
k = thermal conductivity (W m^{-1} K^{-1})
S_h = volumetric heat source (J m^{-3} s^{-1})

S_h is the source term of heat, which is consisting of two parts: change of enthalpy and ohmic heating. It is obtained as follows:

$$S_h = -(h_F + h_P + h_R)\varphi - \frac{I E_{cell}}{l_e} \tag{2.8}$$

where
h_F = enthalpy of formation (kJ mol^{-1})
h_P = enthalpy of product (kJ mol^{-1})
h_R = enthalpy of reactant (kJ mol^{-1})
φ = volume rate of reaction (mol m^{-3} s^{-1})
I = current density (A m^{-2})
l_e = thickness of the electrolyte (m)
E_{cell} = cell voltage (V)

The volume rate of reaction φ is given by:

$$\varphi = \frac{I}{Fl_e} \tag{2.9}$$

species transfer In the gas channels and GDLs of the cell, each species moves due to the pressure gradient and its concentration gradient. Hence, the transfer of each species consists of two parts: the convection part and the diffusion part.

The species transfer is solved by the convection–diffusion equation of species:

$$\nabla \cdot (\rho \mathbf{U} Y_i) + \nabla \cdot j_i = 0 \tag{2.10}$$

where
Y_i = mass fraction of species i (-)
j_i = mass based diffusion flux of species i (kg m^{-2} s^{-1})
ρ = density of gas mixture (kg m^{-3})

The first term on left-hand side of Eq.(2.10) is the convection term, the second term is the diffusion term, the subscript i indicates different species. It is worth to note that, the velocity in Eq.(2.10) is the mass-averaged velocity, the definition of this velocity is given in Appendix 6.3.1.

A simple concept for solving the diffusion flux j_i is Fick's law, which is an empirical equation and derived by Fick in 1855 [99]. It postulates that the diffusion flux of one species is proportional to its concentration gradient:

$$j_i = -\rho D_i \nabla Y_i \tag{2.11}$$

where

D_i = multi-component diffusivity of species i (m^2 s^{-1})

To obtain D_i of Eq.(2.11), binary diffusion coefficients D_{ij} are calculated for each pair of species, according to a binary diffusivity model from Fuller, Schettler and Giddings [100]:

$$D_{ij} = \frac{10^{-7} T^{1.75} \sqrt{1/M_i + 1/M_j}}{p(v_i^{1/3} + v_j^{1/3})^2} \tag{2.12}$$

where
D_{ij} = binary diffusivity for species i and j (m^2 s^{-1})
v_i = diffusion volume of species i (cm^3)

i and j indicate different species, $i \neq j$. The diffusion volumes v_i are according to [101], as shown in Table 2.2.

Table 2.2: Diffusion volumes of species.

	H_2	O_2	H_2O	N_2	CO_2
v$_i$ (m^3)	6.12×10^{-6}	16.3×10^{-6}	13.1×10^{-6}	18.5×10^{-6}	26.7×10^{-6}

The binary diffusion coefficient of flow in a porous media has been approximated by [102]:

$$D_{ij,p} = \frac{\varepsilon}{\tau} \cdot \frac{1}{1/D_{ij} + 1/D_{K_n}} \tag{2.13}$$

where
$D_{ij,p}$ = binary diffusivity for species i and j in porous media (m^2 s^{-1})
ε = average porosity of porous media (-)
τ = average geometric tortuosity of porous media (-)
D_{K_n} = Knudsen diffusivity in porous media (m^2 s^{-1})

The Knudsen diffusivity D_{K_n} is determined from [103]:

$$D_{K_n} = 97 \cdot (d_p/2)\sqrt{T/M_i} \tag{2.14}$$

where
d_p = mean diameter of pores in porous media (m)

The values of ε, τ and d_p are according to literatures and listed in Table 2.4.

Finally, the diffusion coefficient D_i could be calculated according to Wilke's equation [104]:

$$D_i = \frac{1 - X_i}{\sum_{j \neq i} \frac{X_j}{D_{ij}}} \tag{2.15}$$

where
X_i = mole fraction of species i (-)

In Eq.(2.15), D_{ij} is replaced by $D_{ij,p}$ in case of flow in porous media. The D_i can be substituted into Eq.(2.11) to solve the diffusion flux j_i.

electrochemistry The cell voltage is calculated by:

$$E_{cell} = E_{Nernst} - \eta_{act} - IR_{\Omega} \tag{2.16}$$

where
E_{Nernst} = Nernst potential (V)
η_{act} = activation overpotential (V)
I = local current density (A m^{-2})
R_{Ω} = specific ohmic resistance (Ω m^{-2})

As shown in Eq. 1.9, the total overpotential is consisting of three parts: activation overpotential, ohmic overpotential and concentration overpotential. However, the concentration overpotential is not included in Eq. 2.16. The reason is that Eq. 1.9 is an empirical-analytical equation, the mass transfer losses in the porous media are expressed in a single term η_{conc}. In the CFD modelling, the mass transfer in the porous media is locally solved by using Eq. 2.10 - Eq. 2.15, the mass transfer losses are expressed in the decreasing of the concentration of the reactants on the electrolyte-GDE interface.

The activation overpotential is calculated by Tafel equation [16, p.15]:

$$\eta_{act} = \frac{RT}{\alpha F} \ln\left(\frac{I}{i_0} \cdot \frac{X_{ref}}{X_{O_2}}\right) \tag{2.17}$$

where
i_0 = exchange current density (A m^{-2})
α = symmetry factor (-)
X_{ref} = reference mole fraction (-)
X_{O_2} = mole fraction of oxygen (-)

The symmetry factor α is given by kinetic theory; the exchange current density i_0 is approximated by [28, p.38]:

$$i_0 = i_0^{ref} \text{exp}(-\frac{E_A}{R}(\frac{1}{T} - \frac{1}{T_{ref}})) \tag{2.18}$$

where
i_0^{ref} = reference exchange current density (A m^{-2})
E_A = activation energy (J mol^{-1})
T_{ref} = reference temperature (K)

The Nernst potential is given by:

$$E_{Nernst} = E_{th}^T - \frac{RT}{2F} \text{ln}(\frac{X_{H_2O}}{X_{H_2} {X_{O_2}}^{0.5}}) \tag{2.19}$$

where
E_{Nernst} = Nernst potential, neglects pressure changes (V)
E_{th}^T = thermodynamic voltage at the operating temperature (V)
X_{H_2O}, X_{H_2}, X_{O_2} = mole fraction of species H_2O, H_2 and O_2 (-)

Physical properties For determining the density of gas mixture, one can use [105, p.483]:

$$\rho = \frac{p}{RT \sum_{i=1}^{n} \frac{Y_i}{M_i}} \tag{2.20}$$

The heat capacity and dynamic viscosity of each species are determinated using the following polynomials:

$$Cp_i = a_6(\frac{T}{1000})^6 + a_5(\frac{T}{1000})^5 + a_4(\frac{T}{1000})^4 + a_3(\frac{T}{1000})^3 + a_2(\frac{T}{1000})^2 + a_1(\frac{T}{1000}) + a_0 \tag{2.21}$$

$$\mu_i = b_6(\frac{T}{1000})^6 + b_5(\frac{T}{1000})^5 + b_4(\frac{T}{1000})^4 + b_3(\frac{T}{1000})^3 + b_2(\frac{T}{1000})^2 + b_1(\frac{T}{1000}) + b_0 \tag{2.22}$$

where
Cp_i = heat capacity of species i (J K^{-1})
μ_i = dynamic viscosity of species i (Pa s)

The coefficients $a_0, a_1, ...a_6$ and $b_0, b_1, ...b_6$ are according to Todd and Young [106], as shown in Table 2.3.

Table 2.3: The coefficients of Todd-Young's polynomials to calculate heat capacity and dynamic viscosity.

	a_0	a_1	a_2	a_3	a_4	a_5	a_6
H_2	21.157	56.036	-150.55	199.29	-136.15	46.903	-6.4725
O_2	34.850	-57.975	203.68	-300.37	231.72	-91.821	14.776
H_2O	37.373	-41.205	146.01	-217.08	181.54	-79.409	14.015
N_2	29.027	4.8987	-38.040	105.17	-113.56	55.554	-10.350
	b_0	b_1	b_2	b_3	b_4	b_5	b_6
H_2	15.553	299.78	-244.34	249.41	-167.51	62.966	-9.9892
O_2	-1.6918	889.75	-892.79	905.98	-598.36	221.64	-34.754
H_2O	-6.7541	244.93	419.50	-522.38	348.12	-126.96	19.591
N_2	1.2719	771.45	-809.20	832.47	-553.93	206.15	-32.430

The other physical parameters used in the basic model are listed in Table 2.4. The geometric parameters of the porous media are: average porosity ϵ, average geometric tortuosity τ and average diameter of pores d_p. The values of first two are taken from [107]. It must be noted that the value of d_p does not precisely correspond to the GDLs used in the Jülich experiments for validation.

The critical electrochemical parameters are: α, R_Ω and i_0^{ref}. α is the symmetry of the energy barrier of the electrochemical reaction, which can be measured experimentally. In most electrochemical systems the value of α is between 0.3 and 0.7. In the scientific literatures for the modeling work of HT-PEFC, the values of α are between 0 and 1, for example, 0.25 [108], 0.7 [90], 0.8 [58] or 1 [80, 109]. Kinetic theory gives a value α = 0.5, this value is usually used as an approximation in the absence of measurements [110, p.97]. In this work, the value of α is assumed to be 0.5.

R_Ω is the ohmic resistance of the system times the active area. Each component of the HT-PEFC system (such as bipolar plates, membrane, and connectors) has an ohmic resistance. R_Ω represents the overall effect of them. The in-house impedance measurement showed that R_Ω of the HT-PEFC, which was manufactured in our lab, was in the range of 1×10^{-5} Ωm^{-2} to 2×10^{-5} Ωm^{-2}. In this work, the ohmic resistance R_Ω was assumed to be 2×10^{-5} Ωm^{-2}.

i_0^{ref} is the integral characteristic of the catalyst layer, which may depend on several factors: such as the loading of the catalyst, the distribution of the acid in the catalyst layer, the loading of the PBI in the catalyst layer, and the mass transfer resistance of species in the catalyst layer. In practice, since the manufacturing method can not guarantee an isotropic property of the catalyst layer, i_0^{ref} may also vary locally. In this work, i_0^{ref} was assumed to be a constant value of 3.0 A m^{-2}, which is fitted from the polarization curve of an in-house experiment, the experimental data are listed in Appendix 6.1.

Table 2.4: Physical parameters used in the basic model.

Parameter	Symbol	Value	Unit
Average porosity of porous media	ϵ	0.78 [107]	
Average geometric tortuosity of porous media	τ	1.5 [107]	
Average diameter of pores in porous media	d_p	16×10^{-6} [111]	m
Symmetry factor	α	0.5	
Ohmic resistance of cell per m^2	R_Ω	2×10^{-5}	Ω m^{-2}
Reference exchange current density	i_0^{ref}	3.0	A m^{-2}
Reference mole fraction of oxygen	X_{ref}	0.23	
Reference temperature	T_{ref}	433	K
Thermodynamic voltage	E_{th}^T	1.15	V
Activation energy	E_A	57100	J mol^{-1}
Thickness of membrane + CLs	l_e	2×10^{-4}	m

Numerical algorithm The numerical algorithm of the basic model is shown in the following figure.

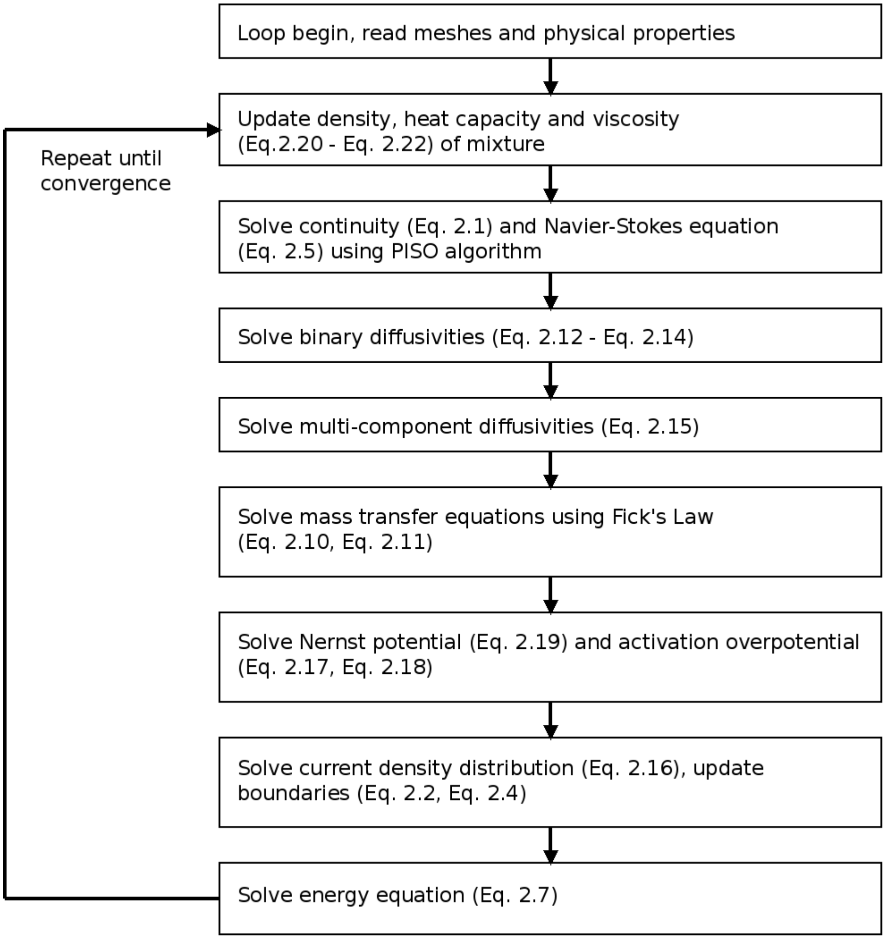
Loop begin, read meshes and physical properties
Update density, heat capacity and viscosity (Eq.2.20 - Eq. 2.22) of mixture
Repeat until convergence
Solve continuity (Eq. 2.1) and Navier-Stokes equation (Eq. 2.5) using PISO algorithm
Solve binary diffusivities (Eq. 2.12 - Eq. 2.14)
Solve multi-component diffusivities (Eq. 2.15)
Solve mass transfer equations using Fick's Law (Eq. 2.10, Eq. 2.11)
Solve Nernst potential (Eq. 2.19) and activation overpotential (Eq. 2.17, Eq. 2.18)
Solve current density distribution (Eq. 2.16), update boundaries (Eq. 2.2, Eq. 2.4)
Solve energy equation (Eq. 2.7)

Figure 2.5: Numerical algorithm of the basic model.

2.3 Macro-homogeneous model (model II)

In the previous basic model, the transfer of oxygen in the catalyst layer is assumed to be very fast. In other words, the basic model assumes that there is no overpotential due to the oxygen transfer in the CL. In this section, the effect of the CL is taken into account. As discussed in Section 1.3, the CL consists of Pt-carbon particles, ionomer and PTFE. The Pt-C particles build agglomerates. The diameter of Pt-C particles is usually in the range of 10 to 20 nm while the diameter of the agglomerates is generally between 60 and 200 nm. Pores exist between the Pt-C particles and between the agglomerates.

The modelling of the mass transfer issue in the CL considered the detailed structure is complicated. To simplify the calculations, distinct theories were developed with their assumptions. An important contribution in this area is the macro-homogeneous approach [49, 50]. This theory employs the macroscopical transfer properties of oxygen and protons in the CL and provides a set of partial differential equations to describe the 1-D concentration distribution of oxygen and protons.

In this section, the macro-homogeneous model based on the work of Kulikovsky [60] is modified and implemented in the CFD code to present the transport effect in the catalyst layer. The catalyst layer is assumed to be isotropic.

Figure 2.6 shows the schematic macro-homogeneous model, where the red curve indicates the density of proton current, the black curve indicates the molar concentration of oxygen and the blue curve is the overpotential. Subscript 0 denotes the membrane-CL interface. The overpotential at the membrane-CL interface is the total overpotential of the CL. The transport properties of protons and oxygen in this region are assumed to be constant.

As shown, the oxygen moves from the GDL side to the membrane side. There are two reasons of the decreasing of oxygen concentration:

1. Oxygen is continuously consumed on the whole diffusion pathway due to ORR.
2. The mass transfer resistance is significant due to the geometrical structure.

Simultaneously, the protons move from the membrane side to the GDL side. Unlike the oxygen, the transport of protons is not through pores between the Pt-C particles and the agglomerates, but through the liquid (phosphoric acid). Due the ORR, the protons are also consumed and the concentration reduced along the pathway.

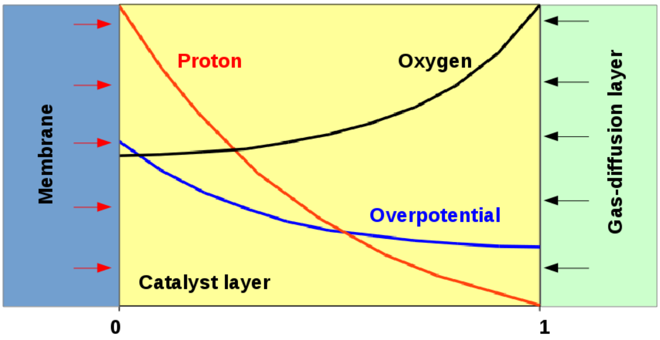

Figure 2.6: Schematic of the cathode CL and the profiles of oxygen, protons and overpotential. Redrawn from [60]

In the cathode CL, the reaction rate of ORR can be expressed as:

$$k_{ORR} = i_*(\frac{c_{O_2}}{c_{ref}})\left[\text{exp}(\frac{\alpha F\eta}{RT}) - \text{exp}(-\frac{(1-\alpha)F\eta}{RT})\right] \tag{2.23}$$

where

k_{ORR} = reaction rate of ORR (A m^{-3})

i_* = volumetric exchange current density (A m^{-3})

c_{O_2} = molar concentration of oxygen (mol m^{-3})

c_{ref} = reference molar concentration (mol m^{-3})

α = symmetry factor (-)

η = total overpotential in CL (V)

This is the Butler-Volmer equation. When α equals 0.5, Eq. 2.23 can be written as:

$$k_{ORR} = 2i_*(\frac{c_{O_2}}{c_{ref}})\text{sinh}\frac{\eta}{b} \tag{2.24}$$

where

k_{ORR} = reaction rate of ORR (A m^{-3} s^{-1})

b is the Tafel slope, which is given by:

$$b = \frac{RT}{\alpha F} \tag{2.25}$$

From the proton current conservation in the CL, there is:

$$\frac{dj_p}{dx} = -k_{ORR} \tag{2.26}$$

where
j_p = proton current density (A m^{-2})
x = distance from the membrane (m)

Therefore the protons current along x in CL is given by:

$$\frac{dj_p}{dx} = -2i_*(\frac{c_{O_2}}{c_{ref}})\text{sinh}\frac{\eta}{b} \tag{2.27}$$

The molar diffusion flux of oxygen is determinated by the electrochemical reaction [50]:

$$D_{CL}\frac{dc_{O_2}}{dx} = \frac{i - j_p}{4F} \tag{2.28}$$

where
D_{CL} = effective diffusivity of oxygen in CL (m^2 s^{-1})
i = local current density (A m^{-2})

According to Ohm's law, the proton current can be calculated as [50]:

$$j_p = -\sigma_t\frac{d\eta}{dx} \tag{2.29}$$

where
σ_t = proton resistance of the CL (Ω m^{-1})

The solution of equation system 2.27-2.29 gives the concentration profiles of oxygen, current density and overpotential along x. The CFD simulation requires a particular solution of the above system: the total overpotential at the membrane-electrolyte interface. The way for solving that particular solution of equation system 2.27-2.29 was provided by [60]. After some mathematical manipulation, that solution can be obtained:

$$\eta_0 = b \cdot \text{arcsinh}(\frac{(i/j_\sigma)^2}{2(c_{O_2}/c_{ref})(1-\text{exp}(-i/(2j_*)))}) + \frac{\sigma_t b^2}{4FD_{CL}c_{O_2}}(\frac{i}{j_*} - ln(1 + \frac{i^2}{{j_*}^2\beta^2})) \tag{2.30}$$

where
η_0 = total overpotential at the membrane-electrolyte interface (V)
j_σ = characteristic current density (A m^{-2})
j_* = superficial exchange current density (A m^{-2})
β = dimensionless parameter (-)

The above equation takes all the potential losses in the CL of the cathode side of the HT-PEFC into account: the first term of the right-hand side represents the proton transfer loss and the activation overpotential, while the second term accounts for the oxygen transfer loss.

The parameter j_σ is given by:

$$j_\sigma = \sqrt{2 i_* \sigma_t b} \tag{2.31}$$

The parameter j_* is given by:

$$j_* = \frac{\sigma_t b}{l_t} \tag{2.32}$$

where
l_t = thickness of the catalyst layer (m)

The parameter β is a solution of:

$$\beta \tan(\frac{\beta}{2}) = \frac{i}{j_*} \tag{2.33}$$

Notice that the Eq. 2.30 is slightly different from Kulikovsky's model [60], the transport losses of the GDL are neglected, because the effect of the GDL is already included in the 3-D CFD simulation.

The local cell current density i at the membrane side is calculated as:

$$i = \frac{E_{cell} - E_{Nernst} - \eta_0}{R_\Omega} \tag{2.34}$$

The Nernst potential is calculated according to Eq. 2.19.

Besides the parameters of Table 2.4, the additional physical parameters of the macro-homogeneous model are listed in Table 2.5. These parameters are fitted from the polarization curve of an in-house experiment, the experimental data are listed in Appendix 6.1.

Table 2.5: Physical parameters used in the macro-homogeneous model.

Parameter	Symbol	Value	Unit
Proton conductivity of the CL	σ_t	8 (assumed)	Ω m^{-1}
Effective diffusivity of oxygen in CL	D_{CL}	6×10^{-7} (assumed)	m^2 s^{-1}
Thickness of the CL	l_t	50×10^{-6} (assumed)	m

In the macro-homogeneous model, the momentum transfer, species transfer and heat transfer are solved with the same governing equations as the basic model. The only difference between the two models is the approach of the electrochemistry. The basic model takes into account the activation overpotential and the ohmic loss, while the macro-homogeneous model takes into account the activation overpotential, the ohmic loss, the proton transfer loss in the CL and the oxygen transfer loss in the CL. Consequently, through the introduction of three additional parameters (σ_t, D_{CL} and l_t), the effect of the CL on the cell performance is reflected in the macro-homogeneous model.

Numerical algorithm The numerical algorithm of the macro-homogeneous model is shown in the following figure. The dashed red box indicates the difference between the macro-homogeneous model and the basic model.

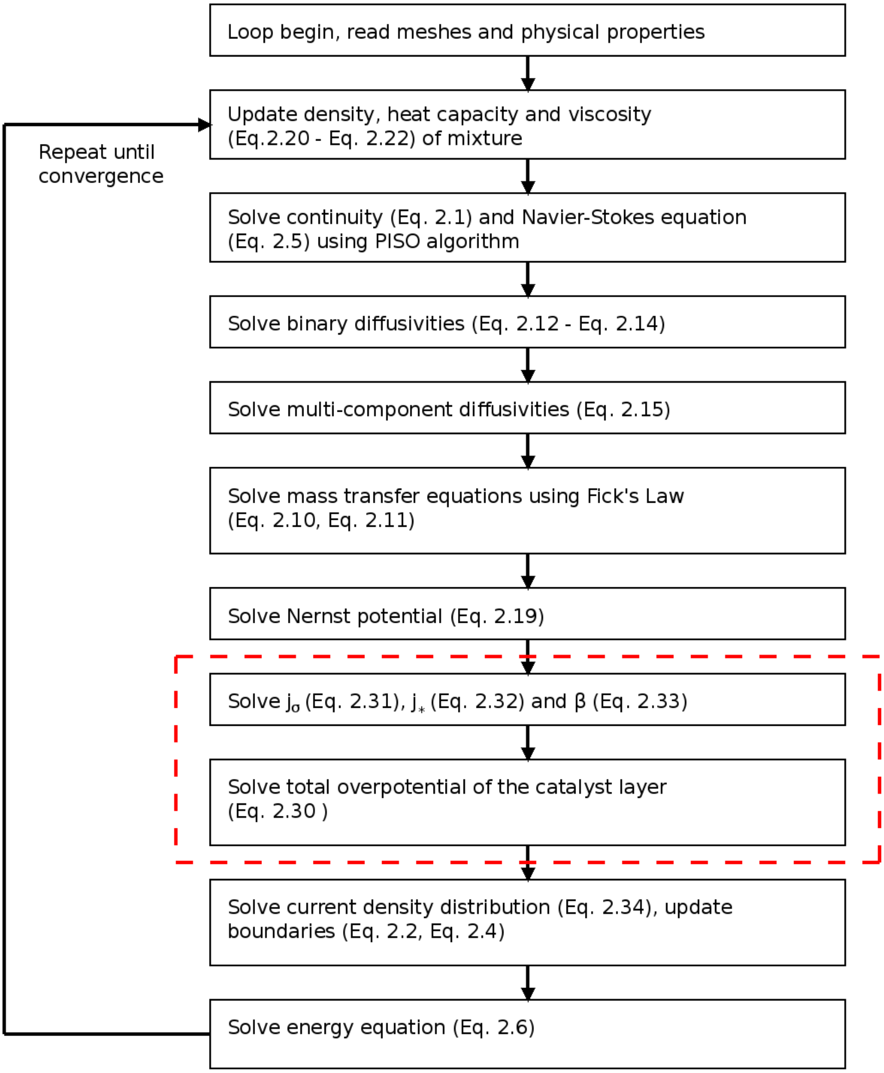
Loop begin, read meshes and physical properties
Update density, heat capacity and viscosity (Eq.2.20 - Eq. 2.22) of mixture
Repeat until convergence
Solve continuity (Eq. 2.1) and Navier-Stokes equation (Eq. 2.5) using PISO algorithm
Solve binary diffusivities (Eq. 2.12 - Eq. 2.14)
Solve multi-component diffusivities (Eq. 2.15)
Solve mass transfer equations using Fick's Law (Eq. 2.10, Eq. 2.11)
Solve Nernst potential (Eq. 2.19)
Solve j_σ (Eq. 2.31), j_* (Eq. 2.32) and β (Eq. 2.33)
Solve total overpotential of the catalyst layer (Eq. 2.30)
Solve current density distribution (Eq. 2.34), update boundaries (Eq. 2.2, Eq. 2.4)
Solve energy equation (Eq. 2.6)

Figure 2.7: Numerical algorithm of the macro-homogeneous model.

2.4 Water transfer model (model III)

Water transfer is another significant mass transfer issue for PEFC and HT-PEFC. For the Nafion system with an operating condition below 100 ℃, water is in both gaseous and liquid state. It is shifted between anode and cathode, depending on the pressure, temperature and flow field design. The performance of a Nafion membrane strongly depends on the water content: it offers a high proton conductivity only when there is an amount of free water inside. Therefore, humidification is required. In recent years, some modelling work of PEFC include a water transfer module, to simulate the water balance between gaseous and liquid state and the water content in the Nafion membrane [112–114]. However, the most CFD-modelling work of HT-PEFC has neglected the water-crossover effect [82, 83, 90].

In HT-PEFC, under the typical operating conditions (T = 160 ℃, p = 1 atm), water is only in the gaseous state in gas channels and GDL. Similar as PEFC, it was observed that a part of produced water was shifted from the cathode side to the anode side, the flux of the water crossover increased with increasing of the mean current density [115, p.59,67] [116]. On the other hand, according to the in-situ synchrotron X-ray radiography experiment of the cross section of the MEA by Maier et al. [117], it was found that the concentration of the phosphoric acid in the membrane is also changed during the operation.

The water balance has a significant influence on the cell performance, because:

- The proton conductivity of HT-PEFC membrane strongly depends on the concentration of phosphoric acid in it [13].
- The partial pressure of water vapor at the anode and cathode catalyst layers may affect the Nernst potential (Eq. (2.19)) and the kinetics (Eq. (2.17)).

Therefore, a water transfer model is developed for solving the water balance of HT-PEFC. Figure 2.8 presents the schematic model of water transfer. The electrolyte is considered as a binary solution of phosphoric acid and water, and the PBI membrane is considered as a porous matrix.

In the previous research, the crossover of water of PEFC is assumed to be caused by the following processes: the electro-osmotic drag, the diffusion, and the hydraulic permeation [118]. For HT-PEFC, the electro-osmotic drag could be neglected [119]. In this model, the diffusion is considered as the main reason for the water transfer. As shown in Figure 2.8, the transfer process of water can be divided into four steps:

1. Water is generated at the membrane-GDE interface.

2. The absorption-evaporation of the water molecules occurs at membrane-GDE interface of the cathode side.

3. Due to the concentration gradient, the liquid water shifts to the other side of the electrolyte.

4. The absorption-evaporation of the water molecules occurs at membrane-GDE interface of the anode side.

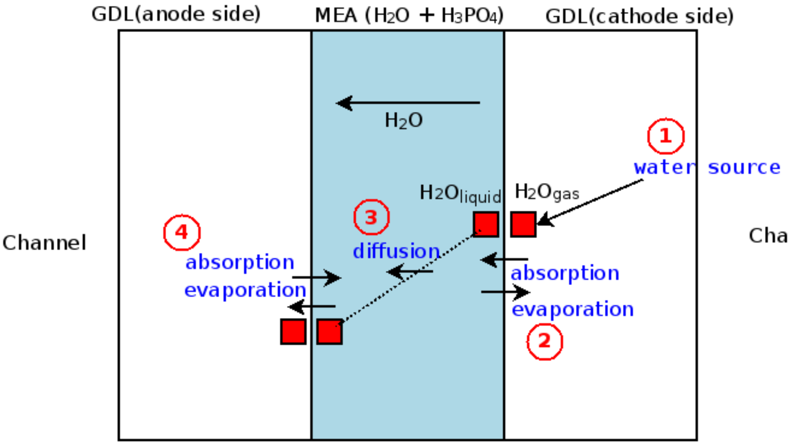
GDL(anode side)
MEA (H2O + H3PO4)
GDL(cathode side)
H2O
1
water source
H2Oliquid
H2Ogas
Channel
4
3
absorption
evaporation
diffusion
absorption
evaporation
2
Channel

Figure 2.8: Schematic model of water transfer in electrolyte.

In this section, the water transfer model consists of two submodels: the basic water transfer model and the modified water transfer model. They are introduced in the following subsections.

Basic water transfer model As shown in Figure 2.8, the transfer of water from the cathode to anode consists of two physical phenomena: i) absorption-evaporation at the membrane-GDE interfaces; ii) diffusion from the cathode side to the anode side.

In the basic water transfer model, these two phenomena are treated as one effective transfer process. A constant value, the effective mass transfer coefficient of water $k_{H_2O}^{eff}$, is used to present the transport property of water in the membrane.

The diffusion flux of the water in electrolyte is given by Fick's law:

$$j_{H_2O} = -k_{H_2O}^{eff} \nabla Y_{H_2O}^{g} \tag{2.35}$$

where

j_{H_2O} = mass based diffusion flux of water (kg m^{-2} s^{-1})

$k_{H_2O}^{eff}$ = effective mass transfer coefficient of water (kg m^{-1} s^{-1})
$Y_{H_2O}^{g}$ = mass fraction of water vapor (-)

Since the thickness of the electrolyte is small compared to the in-plane scale, it is reasonable to neglect the in-plane diffusion of water in electrolyte. Eq. 2.35 can be reduced as follows according to film theory:

$$j_{H_2O} = -D_{H_2O}^{eff} M_{H_2O} (c_{H_2O}^{gas,c} - c_{H_2O}^{gas,a})/l_e \tag{2.36}$$

where
$D_{H_2O}^{eff}$ = effective diffusivity of water (m^2 s^{-1})
M_{H_2O} = molar mass of water (kg mol^{-1})
$c_{H_2O}^{gas,c}$ = molar concentration of water vapor at cathode (mol m^{-3})
$c_{H_2O}^{gas,a}$ = molar concentration of water vapor at anode (mol m^{-3})
l_e = thickness of electrolyte (m)

The molar concentration of water vapor is given by:

$$c_{H_2O}^{gas} = \frac{p_{H_2O}^{gas}}{RT} \tag{2.37}$$

where
$p_{H_2O}^{gas}$ = partial pressure of water vapor (Pa)

The effective diffusivity $D_{H_2O}^{eff}$ is in a range from 1×10^{-7} m^{2}s^{-1} to 3×10^{-7} m^{2}s^{-1} [116, 120].

For steady state, the quantity of water which crosses the membrane is equal to the diffusion flux of water i.e. j_{H_2O} in Eq. 2.36. The cross over rate of water is given by:

$$\gamma = \frac{j_{H_2O} \cdot nF}{M_{H_2O} \cdot I} \tag{2.38}$$

where
γ = water cross over rate (-)

Modified water transfer model In the basic model, the coupling of the local water partial pressure on the electrolyte-GDE interface and the H_3PO_4 concentration in the membrane is not presented. For simulating the H_3PO_4 concentration in the membrane, a modified water transfer model is developed. In this model, the diffusion of water and the absorption-evaporation of water is separately solved. The diffusion flux of the water in the electrolyte is proportional to the gradient of the mass fraction of the liquid water in the electrolyte. The diffusion flux is given by:

$$j_{H_2O} = -k^{eff}_{H_2O,l} \nabla Y^{l}_{H_2O} \tag{2.39}$$

where

j_{H_2O} = mass based diffusion flux of water (kg m^{-2} s^{-1})

$k^{eff}_{H_2O,l}$ = effective mass transfer coefficient of liquid water in the water-acid-PBI system (kg m^{-1} s^{-1})

$Y^{l}_{H_2O}$ = mass fraction of liquid water in the liquid water in the water-acid-PBI system (-)

Eq. 2.39 can be reduced as follows according to film theory:

$$j_{H_2O} = \psi k^{eff}_{H_2O,l} (Y^{liq,c}_{H_2O} - Y^{liq,a}_{H_2O})/l_e \tag{2.40}$$

where

ψ = empirical factor of the effect of the mean current density (-)

$Y^{liq,c}_{H_2O}$ = mass fraction of liquid water at cathode (-)

$Y^{liq,a}_{H_2O}$ = mass fraction of liquid water at anode (-)

The reason of introducing of the empirical factor ψ in Eq. 2.40 is that, the density of the water-acid solution changes by different mean current densities. Consequently, the effective mass transfer coefficient of liquid water in the electrolyte should be corrected by a function of mean current density. In this study, ψ is given by an empirical equation (2.41), the number of 0.75 is fitted from an in-house experiment, the experimental data are listed in Appendix 6.2.

$$\psi = \frac{i_m}{i_{ref,w}} + 0.75 \tag{2.41}$$

where

i_m = mean current density (A m^2)

$i_{ref,w}$ = reference current density (A m^2)

The boundary values of mass fraction of liquid water, $Y^{liq,c}_{H_2O}$ and $Y^{liq,a}_{H_2O}$, are governed by thermodynamic state of water vapor near the liquid-gas interface. Using the experimental data from Schechter et al. [121], an empirical equation can be written (the numbers of 0.517 and 0.046 are fitting numbers):

$$Y^{liq,b}_{H_2O} = 0.517 \frac{p_{H_2O}}{p_{sat}} + 0.046 \tag{2.42}$$

where

$Y^{liq,b}_{H_2O}$ = mass fraction of liquid water of the liquid-gas interface (-)

p_{H_2O} = partial pressure of water vapor (Pa)
p_{sat} = saturation vapor pressure of water (Pa)

The partial pressure of water vapor at the interface p_{H_2O} is obtained by solving Eq.(2.10) in the gas region (Figure 2.1, domain I). The value of the saturation vapor pressure ζ in Pascal is determined by solving Antoine equation:

$$\zeta = 133.322 \cdot 10^{a-b/(c+\tau_0-273.15)} \tag{2.43}$$

where a, b, c are empirical coefficients according to Dortmund Data Bank [122], τ_0 is the value of temperature in Kelvin. The generic form of Eq.(2.43) is the Clausius-Clapeyron equilibrium formulation, that is discussed in [123].

For solving the mass fraction of phosphoric acid and water in the membrane, we may recall the species transfer equation 2.10:

$$\nabla \cdot (\rho \mathbf{U} Y_i) + \nabla \cdot j_i = 0 \tag{2.44}$$

The convection term of the species transfer equation can be neglected in this water transfer model, since it is assumed that there is no pressure gradient in the electrolyte.

Eq. 2.10 is therefore reduced to:

$$\nabla \cdot j_i = 0 \tag{2.45}$$

Substitute Eq. 2.11 into Eq. 2.45, a Laplace's equation is obtained, which accounts for solving the mass fraction of phosphoric acid and water:

$$\nabla^2 Y_i = 0 \tag{2.46}$$

Besides the parameters of Table 2.4, the additional physical parameters of the water transfer model are listed in Table 2.6. These parameters $D^{eff}_{H_2O}$, $k^{eff}_{H_2O,l}$ and $i_{ref,w}$ are fitted from the measured water flux of an in-house experiment, the experimental data are listed in Appendix 6.2.

Table 2.6: Physical parameters used in the water transfer model.

Parameter	Symbol	Value	Unit
Effective diffusivity of water in Eq. 2.36	$D_{H_2O}^{eff}$	2.4×10^{-7} (assumed)	m^2 s^{-1}
Effective mass transfer coefficient in Eq. 2.40	$k_{H_2O,l}^{eff}$	2×10^{-6} (assumed)	kg m^{-1} s^{-1}
reference current density	$i_{ref,w}$	1×10^4 (assumed)	A m^2
Coefficient of Antoine equation	a	8.14019 [122]	
Coefficient of Antoine equation	b	1810.94 [122]	
Coefficient of Antoine equation	c	244.485 [122]	

Numerical algorithm The numerical algorithm of the water transfer model is shown in the following figure. The dashed red box indicates the difference between the water transfer model and the basic model.

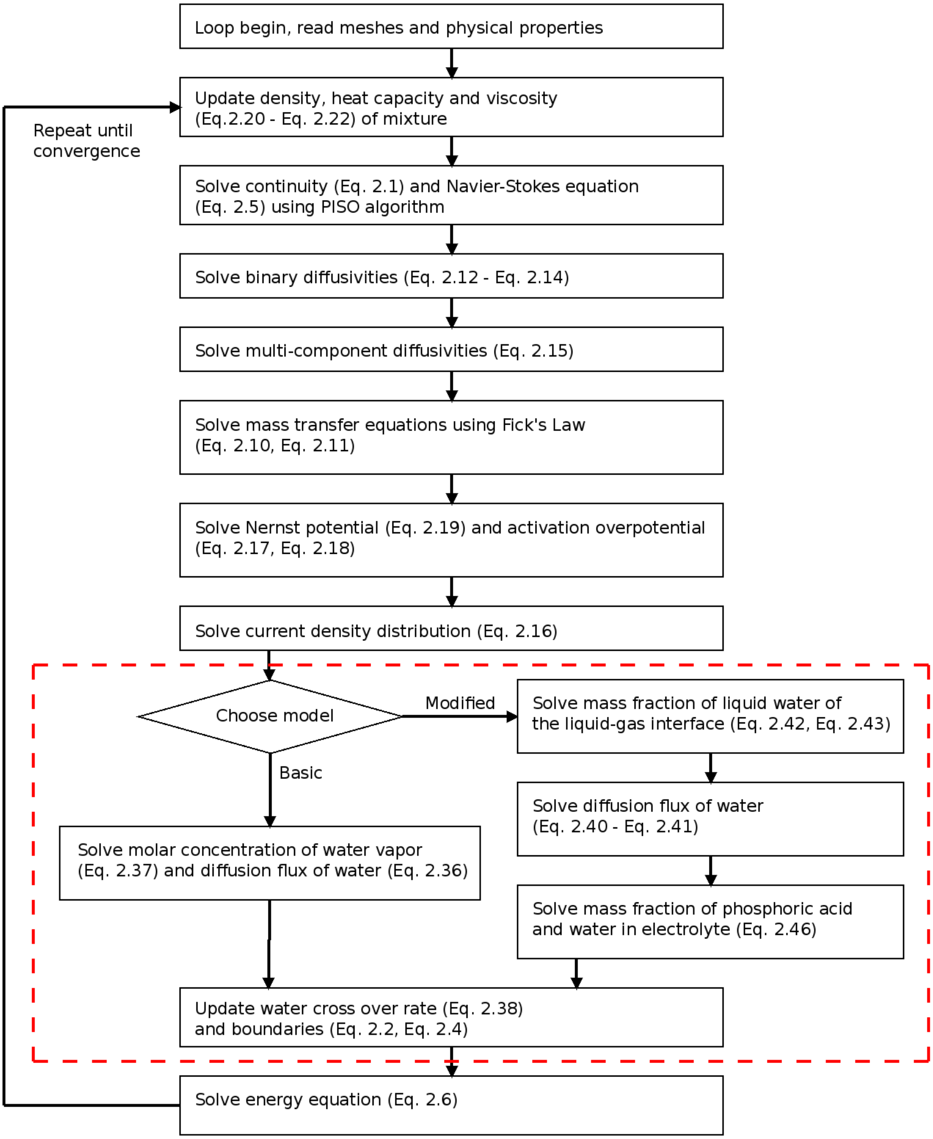
Loop begin, read meshes and physical properties
Update density, heat capacity and viscosity (Eq.2.20 - Eq. 2.22) of mixture
Repeat until convergence
Solve continuity (Eq. 2.1) and Navier-Stokes equation (Eq. 2.5) using PISO algorithm
Solve binary diffusivities (Eq. 2.12 - Eq. 2.14)
Solve multi-component diffusivities (Eq. 2.15)
Solve mass transfer equations using Fick's Law (Eq. 2.10, Eq. 2.11)
Solve Nernst potential (Eq. 2.19) and activation overpotential (Eq. 2.17, Eq. 2.18)
Solve current density distribution (Eq. 2.16)
Choose model
Modified
Solve mass fraction of liquid water of the liquid-gas interface (Eq. 2.42, Eq. 2.43)
Basic
Solve diffusion flux of water (Eq. 2.40 - Eq. 2.41)
Solve molar concentration of water vapor (Eq. 2.37) and diffusion flux of water (Eq. 2.36)
Solve mass fraction of phosphoric acid and water in electrolyte (Eq. 2.46)
Update water cross over rate (Eq. 2.38) and boundaries (Eq. 2.2, Eq. 2.4)
Solve energy equation (Eq. 2.6)

Figure 2.9: Numerical algorithm of the water transfer model.

2.5 Multicomponent diffusion model using Maxwell-Stefan equations (model IV)

A relevant issue of HT-PEFC is the multicomponent diffusion. The basic model is using Fick's law (Eq.(2.11)) for solving the diffusion flux of the species. Following Fick's law, the species always diffuses from the high concentration to low concentration. This equation is commonly used in many engineering applications. It is important to note that, for ternary and higher-order mixtures, Fick's law is suitable only when the binary diffusion coefficients of all components are identical, or else for very dilute mixtures [124, p.88-89]. The reason is that Fick's law neglects the interaction between the species. But, on the pathway of diffusion, the species might be pushed or dragged by other species in the gas mixture.

As shown in Figure 2.10, in a control volume at the cathode side of the HT-PEFC, oxygen (reactant) moves towards the membrane side (reaction zone) while water (product) moves towards the channel side due to their concentration gradient. The internal forces between the species occur and they may not be ignored. For the modelling work, one question needs to be answered: Is Fick's law precise enough for modelling of multicomponent diffusion in HT-PEFC?

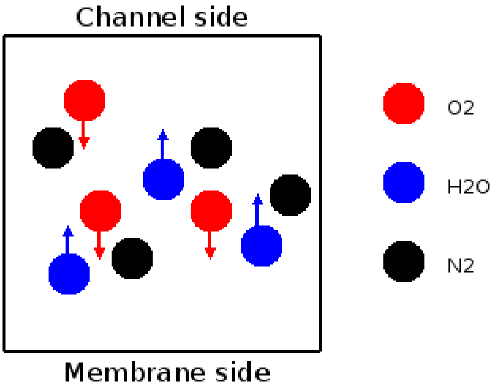

Figure 2.10: The movement of species inside a control volume. The control volume is chosen as the reference. Red points: Oxygen; blue points: water; black points: nitrogen.

To answer this question, another mathematical model is implemented to compare with the Fick's law, which is the Maxwell-Stefan equations. The idea of Maxwell-Stefan equations is that the driving force on a species i equals to the sum of the friction between species i and species j [124, p.39]:

$$F_i = \sum_{j \neq i} \zeta_{i,j} X_j (u_i - u_j) \tag{2.47}$$

where

F_i = diffusion driven force of species i (kg m s^{-2})
$\zeta_{i,j}$ = friction coefficient between species i and j (kg s^{-1})
X_j = mole fraction of species j (-)
u_i, u_j = relative velocity of species (m s^{-1})

After some mathematical manipulation, Eq. (2.47) can be rewritten as [125, p.538]:

$$-c\nabla X_i = \sum_{j=1, j\neq i}^{n} \frac{X_j J_i - X_i J_j}{D_{ij}} \tag{2.48}$$

where
X_i, X_j = mole fraction of species (-)
J_i, J_j = molar based diffusion flux of species (mol m^{-2} s^{-1})
D_{ij} = Maxell-Stefan binary diffusivity for species i and j (m^2 s^{-1})
c = molar concentration of mixture (mol m^{-3})

The derivation of Eq. 2.48 is presented in Appendix 6.3. The Maxell-Stefan binary diffusivity D_{ij} is obtained from Eq. 2.12 in the channels and from Eq. 2.13 in the GDLs. Easy to obtain that Eq. 2.48 is a coupled system, a method of decoupling is required to solve the individuel diffusion flux of each species.

According to Taylor and Krishna [126, p.25], Eq. 2.48 may formally be considered as a relationship between a diffusion flux vector and a mole fraction vector, with the diffusivities represented by a matrix (or more correctly a field of matrices), namely:

$$\frac{\rho}{M}\nabla\vec{X} = -[B]\vec{j} \tag{2.49}$$

where
ρ = density of mixture (kg m^{-3})
M = molar mass of mixture (kg mol^{-1})
$\vec{X}$ = mole fraction vector of species (-)
$\vec{j}$ = mass based diffusion flux vector of species (-)
$[B]$ = $(n-1)\times(n-1)$ diffusivity matrix (-)

Mass-based diffusion flux vector $\vec{j}$ contains all of the individual fluxes from j_1 to j_n. The elements of the diffusivity matrix $[B]$ can be written as

$$B_{ii} = \frac{X_i}{D_{in}} \frac{1}{M_n} + \sum_{j=1, j \neq i}^{n} (\frac{X_j}{D_{ij}} \frac{1}{M_i}), \quad i = 1, 2, ...n-1 \tag{2.50}$$

$$B_{ij} = -X_i(\frac{1}{D_{ij}} \frac{1}{M_j} - \frac{1}{D_{in}} \frac{1}{M_n}), \quad i = 1, 2, ...n-1; i \neq j \tag{2.51}$$

where the binary diffusivities are obtained from Eq. 2.12 or Eq. 2.13, depending on the region to be calculated.

The relationship between gradient of mass fraction and gradient of mole fraction is introduced by Whitaker [127]:

$$\nabla \vec{X} = [W] \nabla \vec{Y} \tag{2.52}$$

where $[W]$ is a $(n-1) \times (n-1)$ matrix. The elements of this matrix can be written as

$$W_{ii} = \frac{M}{M_i} + X_i(\frac{M}{M_n} - \frac{M}{M_i}), \quad i = 1, 2, ...n-1 \tag{2.53}$$

$$W_{ij} = X_i(\frac{M}{M_n} - \frac{M}{M_j}), \quad i = 1, 2, ...n-1; i \neq j \tag{2.54}$$

Combine Eq. 2.52 and Eq. 2.49, the mass-based diffusion flux is given by:

$$\vec{j} = -\frac{\rho}{M} [B]^{-1} [W] \nabla \vec{Y} \tag{2.55}$$

Finally, Eq. 2.55 can be substituted into Eq. 2.10 for solving the mass transfer. The derivation of Eq. 2.49 - Eq. 2.55 are presented in Appendix 6.3.

Numerical algorithm The numerical algorithm of the multicomponent diffusion model is shown in the following figure. The dashed red box indicates the difference between the multicomponent diffusion model and the basic model.

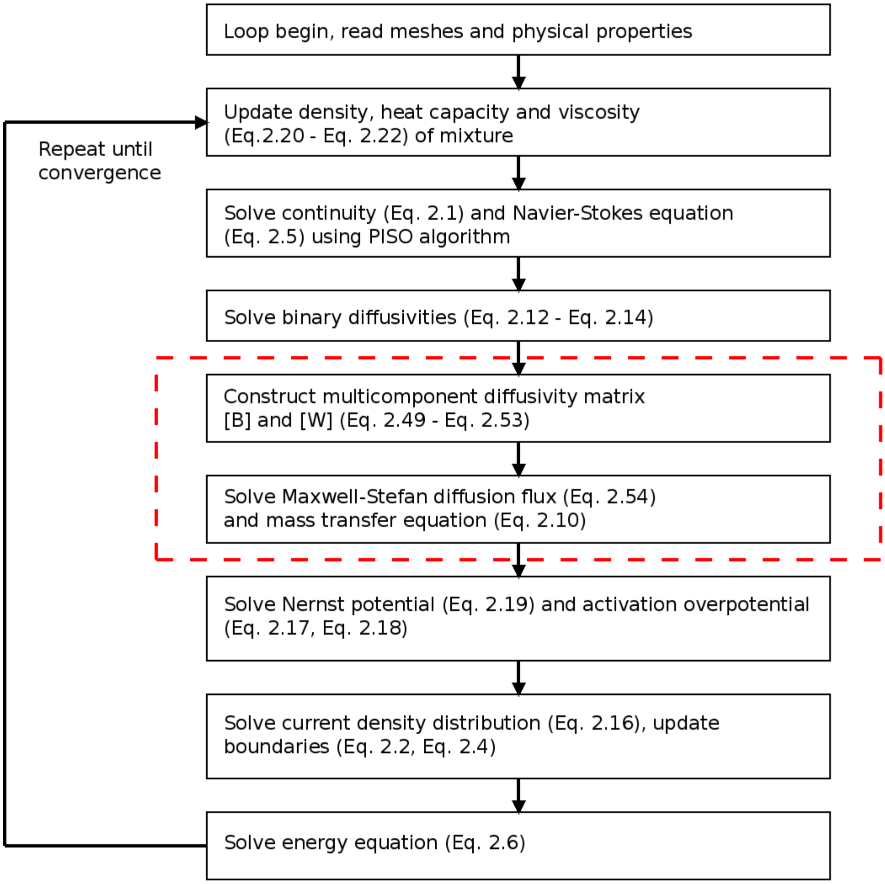
Loop begin, read meshes and physical properties
Update density, heat capacity and viscosity (Eq.2.20 - Eq. 2.22) of mixture
Repeat until convergence
Solve continuity (Eq. 2.1) and Navier-Stokes equation (Eq. 2.5) using PISO algorithm
Solve binary diffusivities (Eq. 2.12 - Eq. 2.14)
Construct multicomponent diffusivity matrix [B] and [W] (Eq. 2.49 - Eq. 2.53)
Solve Maxwell-Stefan diffusion flux (Eq. 2.54) and mass transfer equation (Eq. 2.10)
Solve Nernst potential (Eq. 2.19) and activation overpotential (Eq. 2.17, Eq. 2.18)
Solve current density distribution (Eq. 2.16), update boundaries (Eq. 2.2, Eq. 2.4)
Solve energy equation (Eq. 2.6)

Figure 2.11: Numerical algorithm of the multicomponent diffusion model.

2.6 Discretization methods

The governing equations shown in the preceding models (Eq.(2.1), Eq.(2.5), Eq.(2.7) and Eq.(2.10)) are partial differential equations (PDEs). These PDEs can not be solved directly. In the scope of CFD, three main discretization approaches are available to transform the PDEs into a corresponding system of algebraic equations: the finite differences method (FDM), the finite volume method (FVM) and the finite element method (FEM). In this thesis, FVM is chosen to solve the problem, because the employed software OpenFOAM is based on FVM.

The implementation of FVM has two steps: the discretization of space and the discretization of equations.

Discretization of space The solution domain is discretized into the mesh. In OpenFOAM, the mesh can be arbitrarily unstructured, which means that cells can have a polyhedral shape with a variable number of neighbours. The cells of the mesh are called control volumes. The typical control volumes are presented in Figure 2.12. The point P is sitting in the centroid of a control volume, and point N is located in the centroid of the "neighbour" control volume. The distance vector between P and N is marked with $\mathbf{D}$, and the face between this two control volumes is marked with F. The face area vector $\mathbf{S_F}$ is normal to the face F. The magnitude of $\mathbf{S_F}$ equals to the area of F. In the numerical calculation, the properties are principally stored at the cell centers. However, they may also be stored in the internal face F or the face area vector $\mathbf{S_F}$.

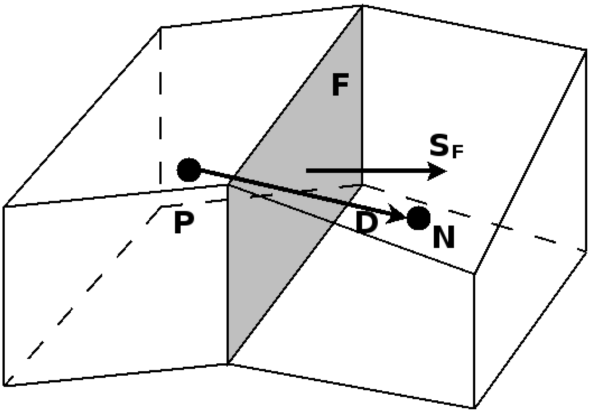

Figure 2.12: Sketch of the finite volume discretization.

Discretization of equations All the PDEs in this thesis can be written as the standard form for a scalar property ϕ:

$$\underbrace{\nabla \cdot (\rho \mathbf{U} \phi)}_{\text{convection term}} - \underbrace{\nabla \cdot (\rho \Gamma_\phi \nabla \phi)}_{\text{diffusion term}} = \underbrace{S_\phi}_{\text{source term}} \tag{2.56}$$

where Γ_ϕ is the diffusivity and S_ϕ is the source term. It is worth to note that there is no temporal term because all the models of this thesis are in steady state.

The FVM is based on the integral form of governing equations over each control volume. The integral form of Eq.(2.56) is given by:

$$\underbrace{\int_V \nabla \cdot (\rho \mathbf{U} \phi) dV}_{\text{convection term}} - \underbrace{\int_V \nabla \cdot (\rho \Gamma_\phi \nabla \phi) dV}_{\text{diffusion term}} = \underbrace{\int_V S_\phi dV}_{\text{source term}} \tag{2.57}$$

where V denotes the volume of a control volume. To solve this equation numerically, the convection term, the diffusion term and the soure term should be linearized one by one.

The convection term, the diffusion term and the source term are linearized as follows:

$$\int_V \nabla \cdot (\rho \mathbf{U} \phi) dV = \sum_F \mathbf{S_F} \cdot (\rho \mathbf{U})_F \phi_F \tag{2.58}$$

$$\int_V \nabla \cdot (\rho \Gamma_\phi \nabla \phi) dV = \sum_F (\rho \Gamma_\phi)_F \mathbf{S_F} \cdot (\nabla \phi)_F \tag{2.59}$$

$$\int_V S_\phi dV = S_{\phi,P} V \tag{2.60}$$

where F denotes the faces surrounding a control volume, $\mathbf{S_F}$ is the area vector showed in Figure 2.12, ϕ_F is the value of property ϕ at the internal face F, $S_{\phi,P}$ is the source at the point P.

For determining the face field ϕ_F, the Gamma differencing scheme [128] is used. This scheme is an automatically and smooth blending between the first-order upwind differencing scheme and the second-order central differencing scheme. For all the faces of the mesh, the boundedness requirements are first checked. If the requirements are satisfied, the central differencing scheme is used. Otherwise, the upwind differencing scheme is used. The smooth blending between the central differencing scheme and the upwind differencing scheme is governed by a blending factor β_m, the useful range of β_m between 0.2 and 0.5. In this thesis, β_m = 0.2 has been used.

After the linearization, Eq.(2.57) becomes the system of algebraic equations, which ignores the non-linearity of the underlying PDEs. This equation system can be commonly expressed as:

$$[A][\phi] = [b] \tag{2.61}$$

where $[A]$ is a square sparse matrix, $[\phi]$ is the column vector of dependent variable ϕ and $[b]$ is the source vector. This system is then solved by the linear equation system solvers provided by OpenFOAM [15]. These solvers, preconditioners and tolerances of the transfer equations are listed in Table 2.7.

Table 2.7: The solution methods of the transfer equations. PCG: preconditioned conjugate gradient solver; PBiCG: preconditioned bi-conjugate gradient solver; DIC: diagonal incomplete-Cholesky; DILU: diagonal incomplete LU.

Equation	Solver	Preconditioner	Tolerance
p equation	PCG	DIC	1e-09
U equation	PBiCG	DILU	1e-09
Y_i equation	PBiCG	DILU	1e-09
T equation	PBiCG	DILU	1e-10

3 Numerical results

3.1 Mesh independence study

The simulation using CFD is based on discretization methods. Because of the discretization, numerical results always have errors compared to analytical results. Theoretically, these errors equal to zero only when the cells of the meshes are infinitely small. In practice, the meshes can not be too small, because decreasing of the cell size causes increasing of computing time and rounding error. Therefore, it is necessary to find the optimal size of the mesh, for guaranteeing the accuracy and speed of the simulation.

In this work, two geometries are used in the simulations: the single channel pair and the single cell with serpentine flow field. For each geometry, meshes of different sizes can be employed. Mesh independence studies are carried out to find the optimal mesh size. Simulations were performed with these meshes under the same operating condition, as shown in Table 3.1. The basic model was applied in these simulations.

Figure 3.1 shows the mesh independence studies for the single channel pair with an active area of 0.2 cm^2. The mean current density of these simulations were set to be 4000 A/m^2. Four meshes were produced with various number of hexahedra units: 1.2×10^3, 46.7×10^3, 94.4×10^3 and 188.8×10^3. The cell voltages were calculated and compared. It shows that the cell voltage increases non-linearly with increasing of the mesh size. Before point A (94.4×10^3), the cell voltage ranges from 0.4946 V to 0.5004 V; after point A, the cell voltage is almost constant. The deviation between points A and B is only 0.8 mV (0.16% of point A), which is caused possibly by numerical error and is acceptable for engineering application.

Figure 3.2 presents the mesh independence test for the single cell with serpentine flow field with an active area of 50 cm^2. Similar to the single channel pair, four meshes were studied with the following number of hexahedra units: 6×10^3, 47×10^3, 741×10^3 and 3000×10^3, with the mean current density of 4000 A/m^2. The cell voltages were calculated and compared. Again, when the mesh size is larger than point a, the cell voltage stays almost constant. The deviation between points a and b is only 0.6 mV (0.09% of point a), this small deviation is neglectable.

The above mesh independence studies for both geometries were carried out again with the mean current density of 6000 A/m^2. The calculated cell voltages showed the same trends as the mean current density of 4000 A/m^2

Consequently, for the single channel pair, the mesh with the size of 94.4×10^3 is considered as the suitable mesh for the following simulations. For the single cell with serpentine flow field, the mesh with the size of 741×10^3 is chosen for the following simulations.

Table 3.1: Operating conditions of the mesh independence studies for both single channel pair and single cell with serpentine flow field. The mean current density was 4000 A/m^2.

Parameter	Symbol	Value	Unit
Operating temperature	T	433	K
Pressure at anode outlet	p_a	101325	Pa
Pressure at cathode outlet	p_c	101325	Pa
Mass fraction of H_2 at anode inlet	Y_{H_2}	1.00	
Mass fraction of O_2 at cathode inlet	Y_{O_2}	0.23	
Mass fraction of N_2 at cathode inlet	Y_{N_2}	0.77	
Anode stoichiometric ratio	λ_a	2	
Cathode stoichiometric ratio	λ_c	2	

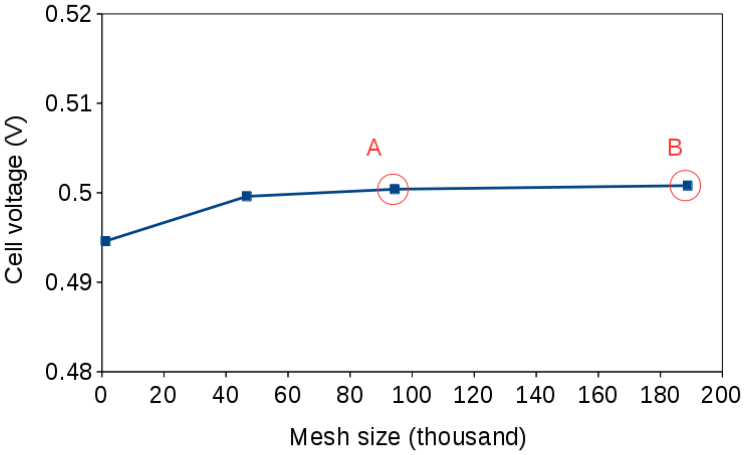

Figure 3.1: Mesh independence studies of the single channel pair geometry. The mean current density was 4000 A/m^2.

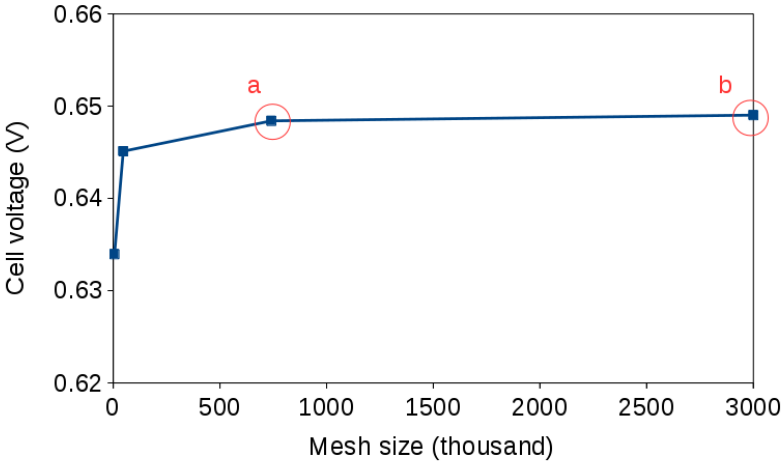

Figure 3.2: Mesh independence studies of the single cell geometry with serpentine flow field. The mean current density was 4000 A/m^2.

3.2 Simulations with the single channel pair

As mentioned in Section 2.1.2, two geometries were used in this thesis: the single channel pair and the single cell with serpentine flow field. For simulations of the single channel pair, the geometry is relative simple compared to another one: the total length of the single straight channel is 17 mm with two offsets on the inlet side (5 mm) and the outlet side (2 mm). The active area of the cell is 0.2 cm^2 (2 mm $\times$ 10 mm). For simulations of the single cell with serpentine flow field, the geometry corresponds to an existing in-house HT-PEFC cell: the cell with 5-fold serpentine flow field, the active area of the cell is 50 cm^2.

In this section, the results of the basic model and the multicomponent diffusion model are shown, with the single channel pair geometry. The compression effect of GDL is also discussed.

3.2.1 Basic model (model I)

In this section, the numerical results of the basic model are shown. The operating conditions of the simulations are listed in Table 3.2.

The physical parameters are listed in Table 2.4. The sensitive parameters to the overall performance are the electrochemical parameters: the symmetry factor α, the specific ohmic resistance R_Ω and the reference exchange current density i_0^{ref}. In this work, α = 0.5, R_Ω = 2×10^{-5} Ωm^{-2} and i_0^{ref} = 3.0 A m^{-2}. These three parameters are fitted from the polarization curve of an in-house experiment, the experimental data are listed in Appendix 6.1. For the curve fitting, the initial guesses of these electrochemical parameters are first proposed. These values are adjusted during the repeat simulations, until the optimal curve fitting is shown.

Table 3.2: Operating conditions for the basic model with the single channel pair geometry. The mean current densities were 1000 - 8000 Am^{-2}.

Parameter	Symbol	Value	Unit
Operating temperature	T	433	K
Pressure at anode outlet	p_a	101325	Pa
Pressure at cathode outlet	p_c	101325	Pa
Mass fraction of H_2 at anode inlet	Y_{H_2}	1.00	
Mass fraction of O_2 at cathode inlet	Y_{O_2}	0.23	
Mass fraction of N_2 at cathode inlet	Y_{N_2}	0.77	
Anode stoichiometric ratio	λ_a	2	
Cathode stoichiometric ratio	λ_c	2	

Polarisation curve

For a fuel cell, the polarisation curve shows the overall performance. In this work, eight operating conditions with the mean current densities from 1000 A/m^2 to 8000 A/m^2 were taken to simulate the main operation area of an HT-PEFC.

The numerical result of the polarisation curve is compared with the experimental data, as shown in Figure 3.3. It is worth to note that, the experimental cell used for comparison was under the same operating conditions as the simulations (Table 3.2). However, the geometry was different: the experimental cell was a single cell with serpentine flow field, the active area was 50 cm^2.

One can see that the simulations fit the experimental data. The shape of the simulated curve was similar to Figure 1.6: it consists of an activation loss region and an ohmic loss region. However, the dramatical drop of the cell voltage by high mean current density was not presented. Because in the high-current region, there is a numerical problem with the algorithms of the basic model: when the consumption of reactants is too high, the mole fraction of reactants of some grids at the electrolyte-GDE interface might be quite close to zero or even negative during the iterative loop. It will cause the huge fluctuation of the Nernst potential and the activation overpotential. The code was consequently unstable. Therefore, the basic model is not appropriate for the simulation of the high current region (I > 8000 A/m^2).

The basic model allows to separate the total overpotential to two loss mechanisms: the activation overpotential and the ohmic overpotential, as shown in Figure 3.4. The numerical result suggests that, with the prescribed parameters in Table 2.4, the activation loss is at least four times of the ohmic loss. The activation overpotential increases from 0.48 V to 0.65 V with increase of the mean current density. This increase is not linear in the low current region (up to 3000 A/m^2). On the other hand, the ohmic overpotential (from 0.02 V to 0.16 V) grows linearly with the mean current density.

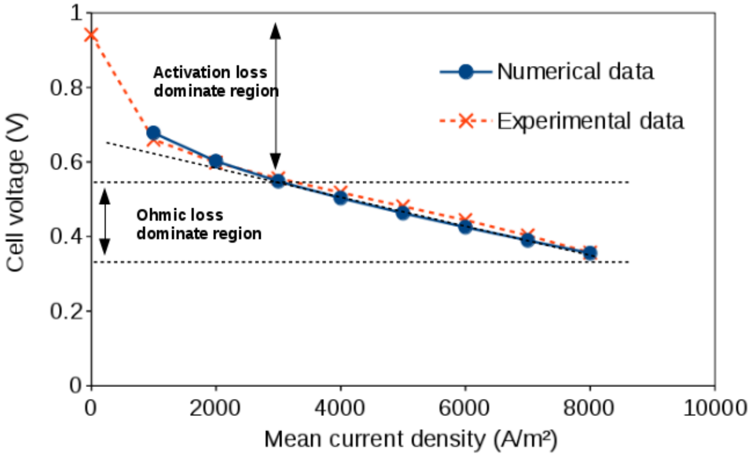

Figure 3.3: Polarisation curve: comparison of numerical results of the basic model (blue solid line) and experimental data (red dash line).

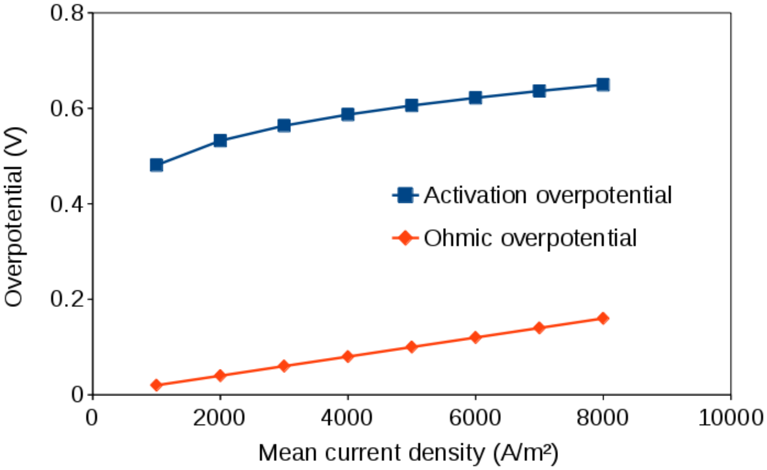

Figure 3.4: Overpotential of numerical results of the basic model.

Local distribution of properties

The polarisation curve only reflects the overall performance of a model. The obvious benefit of a CFD model is that the local information of the flow fields can be presented. The local distributions of the physical properties, such as mole fraction of species, velocity, temperature, and current density are presented and discussed in this paragraph.

Two operating points are taken to compare the distribution of properties at the low mean current density and high mean current density: 2000 Am^{-2} and 8000 Am^{-2}.

The mass balances of the species for the anode side and the cathode side are checked. For the reactants (O_2 and H_2), the relative mass transfer error is given by:

$$\delta_i = \frac{(\phi_{in,i} - \phi_{cons,i} - \phi_{out,i})}{\phi_{in,i}} \times 100\% \tag{3.1}$$

where

δ_i = relative mass transfer error of species i

$\phi_{in,i}$ = mass flux of species i on the inlet of the channel (kg s^{-1})

$\phi_{cons,i}$ = mass flux of species i which is consumed by the electrochemical reaction, calculated by using Faraday's law (kg s^{-1})

$\phi_{out,i}$ = mass flux of species i on the outlet of the channel (kg s^{-1})

For the products (H_2O), the relative mass transfer error is given by:

$$\delta_i = \frac{(\phi_{prod,i} - \phi_{out,i})}{\phi_{prod,i}} \times 100\% \tag{3.2}$$

where

$\phi_{prod,i}$ = mass flux of species i which is produced by the electrochemical reaction (kg s^{-1})

For the inert species (N_2), the relative mass transfer error is given by:

$$\delta_i = \frac{(\phi_{in,i} - \phi_{out,i})}{\phi_{in,i}} \times 100\% \tag{3.3}$$

At 2000 Am^{-2}, the relative mass transfer errors of the species are: δ_{O_2} = 0.29 %, δ_{H_2} = 0.04 %, δ_{H_2O} = 0.09 %, δ_{N_2} = -0.21 %. At 8000 Am^{-2}, the relative mass transfer errors of the species are: δ_{O_2} = 0.11 %, δ_{H_2} = 0.01 %, δ_{H_2O} = 0.08 %, δ_{N_2} = -0.007 %.

The numerical calculation gives the local information for both anode side and cathode side. However, only the results at the cathode side are presented here, since: i) in the basic model, the pure hydrogen is used as the fuel, and it is assumed that there is no water at the anode side. Therefore, the mole fraction is always 100 % at the anode side; ii) in the basic model, the distributions of species at the cathode side determine the performance of the fuel cell, since the activation overpotential (Eq.(2.17)) is calculated according to the mole fraction of oxygen on the membrane-electrolyte interface and the Nernst voltage (Eq.(2.19)) is calculated according to the mole fraction of oxygen and water on that interface. In the modelling literature for hydrogen/air HT-PEFC [78], the cathode side was also chosen for presenting the numerical results.

Since the 3-D fields of properties are not straightforward to show, two cross-sectional planes at the cathode side are used to display the local information. As shown in Figure 3.5, plane A is in the center of the channel and perpendicular to the MEA. Plane B is the electrolyte-GDE interface, which is located between the channel offsets. Plane A provides the information of the distributions of the physical parameters in the channel and GDL, while plane B provides the information of the distributions of the physical parameters in the reaction area.

The mole fraction of oxygen on plane A of these two operating points are presented in Figure 3.6. As shown, the oxygen mole fraction distributions on plane A of the both operating points have similar trends:

- The maximum value occurs in the inlet region, and the mole fraction decreases along the flow direction. This result is expected because the oxygen is consumed along the flow direction.

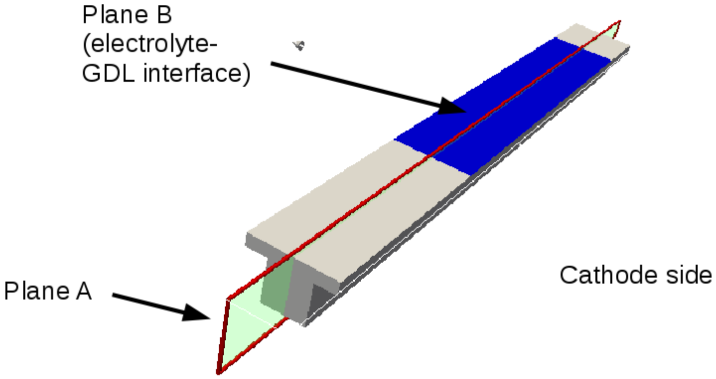

Figure 3.5: Cross-sectional planes for presenting the local distribution of properties at the cathode side.

- The mole fraction in the channels is higher than that in the GDL. This result is expected because the electrochemical reaction is assumed to occur on the electrolyte-GDE interface, the mole fraction of oxygen at this interface is lower than that in the channel.

However, one can observe that the distributions of the oxygen mole fraction in the active zones at these two operating points are different. At 2000 Am^{-2}, the value of the oxygen mole fraction in the active zones of plane A is between 9.0 % and 18.8 %; at 8000 Am^{-2}, this range is larger: from 7.5 % to 20.4 %. For analysing this difference precisely, four sampling lines are created, as shown in Figure 3.7. The sampling line 1 locates in the middle of the channel on plane A, which is used to present the mole fraction in the flow direction (X-direction). The sampling line 2-4 locate in the active zone on plane A, which are used to introduce the mole fraction in the channel-to-GDE direction (Z-direction).

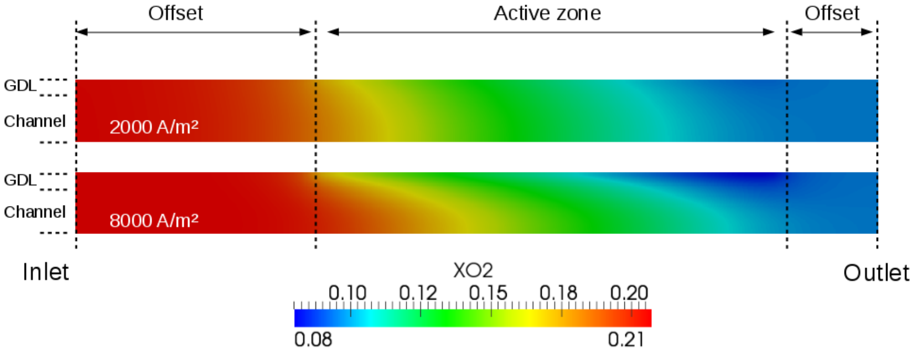

Figure 3.6: Comparison of mole fraction distribution of oxygen at low- (2000 Am^{-2}) and high (8000 Am^{-2}) mean current densities on Plane A.

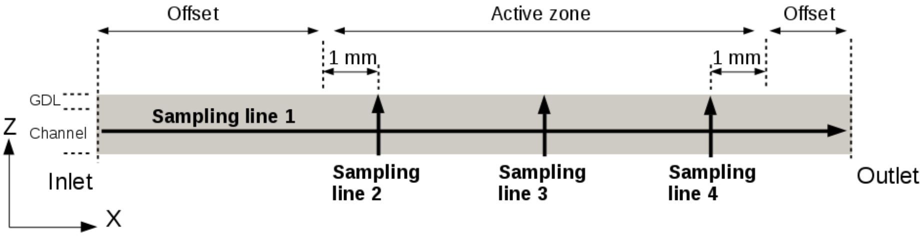
Offset
Active zone
Offset
1 mm
1 mm
GDL
Z
Channel
Sampling line 1
Inlet
Sampling line 2
Sampling line 3
Sampling line 4
Outlet
X

Figure 3.7: Sketch of sampling lines to present the distributions of the oxygen mole fraction on Plane A.

The mole fractions of oxygen in the channel (sampling line 1) are plotted and compared with the analytical solution in Figure 3.8. The analytical solution of the mole fractions of oxygen in the channel is given by [129]:

$$X_{O_2}(x) = X^0_{O_2}(1-\frac{1}{\lambda})^{x/x^0} \tag{3.4}$$

where

$X_{O_2}(x)$ = mole fractions of oxygen along the x direction

$X^0_{O_2}$ = mole fractions of oxygen at the beginning of the active zone

λ = stoichiometric factor

x = displacement (m)

x^0 = total length of the active zone (m)

As shown, the numerical and the analytical results have similar trends: the mole fractions decrease along the flow direction. The similar concentration profile of oxygen was reported in the literature [130]. However, the numerical results in the active zone are lower than the analytical results. The deviations between the numerical and the analytical results can be explained as:

- The analytical solution (Eq. (3.4)) assumed plug flow, ideal mixed gases and no transfer loss in the porous media, X_{O_2} along the channel is only the function of distance and stoichiometrical factor.
- The numerical results are local values along the sampling line in the middle of the channel. The analytical result is a 1-D solution, which neglectes the 3-D effect of the geometry.

The difference between the numerical and the analytical results for 2000 Am^{-2} is between 0.8 % and 2.4 %, for 8000 Am^{-2} is between 0.6 % and 0.7 %: the numerical results at high current is closer to the analytical results than low current. This effect is not reported in the modelling works of HT-PEFC so far. To explain this effect, a dimensionless number, Péclet number (Pe), is calculated to determine the ratio of convection and diffusion:

$$\mathrm{Pe} = \frac{U_x L}{D_i} \tag{3.5}$$

where

Pe = Péclet number (-)
U_x = velocity of the gas in the flow direction (m s^{-1})
L = geometric characteristic length (m)
D_i = multi-component diffusivity of species i (m^2 s^{-1})

In the channel, at the beginning of the active zone, U_x for 2000 Am^{-2} is 0.07 m/s and for 8000 Am^{-2} is 0.28 m/s. L is 0.017 m and D_i is calculated as 2.98 $\times$10^{-5} m^2 s^{-1}. Hence, for 2000 Am^{-2}, Pe is 41; for 8000 Am^{-2}, Pe is 164. This calculation shows that the influence of the diffusion on the total mass transfer in the flow direction is small. However, this influence at the low current (2000 Am^{-2}) is four times higher than high current (8000 Am^{-2}). The numerical result at the high current is closer to the analytical result, since the analytical result neglects completely the diffusion effect. One can see that by the analytical result, the mole fraction starts going down exactly at the entry of the active zone; by the numerical results, the decreasing of the mole fraction occurs earlier. This effect can be explained as the back diffusion.

The mole fractions of oxygen in the channel-to-GDE direction (sampling line 2-4) are presented in Figure 3.9. As shown, the mole fractions decrease along the channel-to-GDE direction (from the BPP side to the membrane side). The gradients of the oxygen mole fraction at 2000 Am^{-2} are lower than that at 8000 Am^{-2}, in all three positions. In Figure 3.9, breaks in all curves take place at the position $Z/Z^0 = 0.769$, because that position is the boundary between the channel and GDL. One can observe that the gradients of the oxygen mole fraction in the GDL are higher than that in the channel. This simulation shows that the higher the mean current density is, the larger deviation of X_{O_2} presents between the channel (bulk side) and the area under the GDL (reaction zone). In practice, although X_{O_2} at the inlet is usually around 21 % (in the air), the X_{O_2} at the reaction zone changes with the mean current densities.

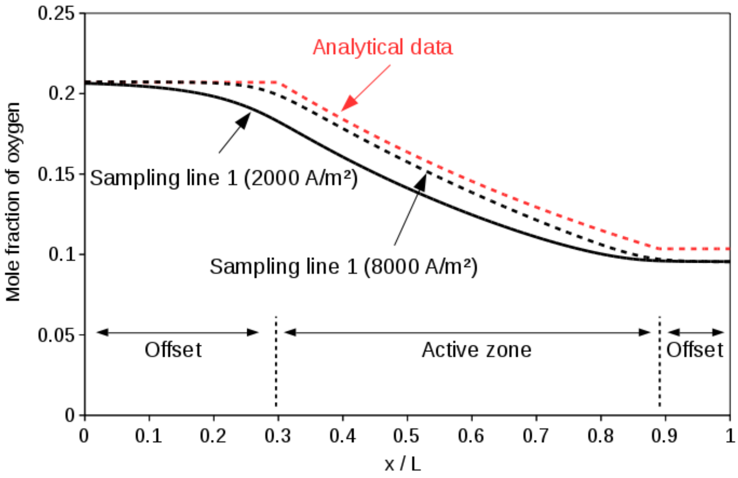

Figure 3.8: Comparison of mole fraction distribution of oxygen along sampling line 1 at low- (2000 Am^{-2}) and high (8000 Am^{-2}) mean current densities on Plane A. λ = 2/2. The index 0 indicates the channel inlet while the index 1 indicates the channel outlet. L = 17 mm (the total length of the channel).

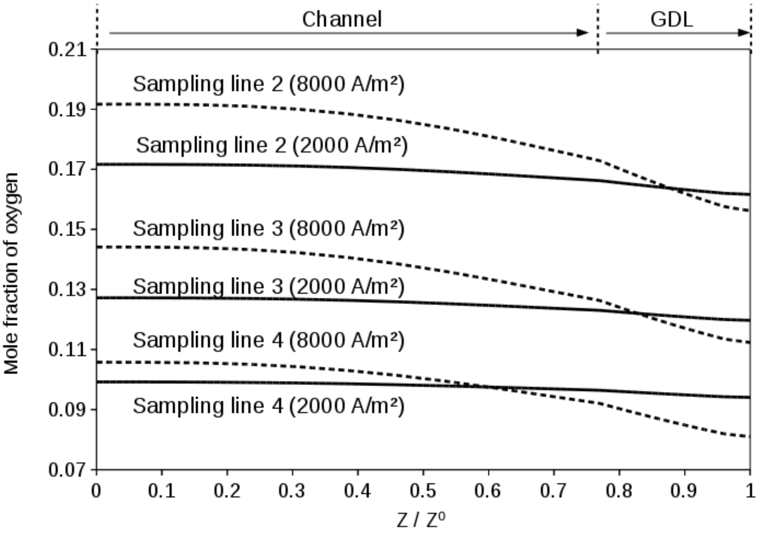

Figure 3.9: Comparison of mole fraction distribution of oxygen along sampling lines 2-4 at low- (2000 Am^{-2}) and high (8000 Am^{-2}) mean current densities on Plane A. λ = 2/2. The index 0 indicates the BPP side while the index 1 indicates the membrane side. Z^0 = 1.3 mm (the height of the channel + GDL).

Figure 3.10 presents the water vapour mole fraction distributions on plane A. Opposite to oxygen, the mole fraction increases along the flow direction and the mole fraction in the GDL is higher than which in the channel. This result is expected, because when more oxygen is consumed, more water is also produced according to the reaction. One can also see that by the both numerical results, the increasing of the mole fraction of water occurs before the entry of the active zone, this can be explained as the diffusion effect.

The magnitude of the velocity distribution of these two operating points on plane A is shown in Figure 3.11. On the wall, the boundary condition of the velocity is assumed to be zero; on the electrolyte-GDE interface, the boundary condition is calculated according to Eq. (2.4) and updated by every iteration. The inlet boundary is calculated according to:

$$\mathbf{U}_{inlet} = \frac{IM_{air}\lambda}{nF\rho_{air}} \tag{3.6}$$

where
I = current density (A m^{-2})
M_{air} = molar mass of air (g mol^{-1})

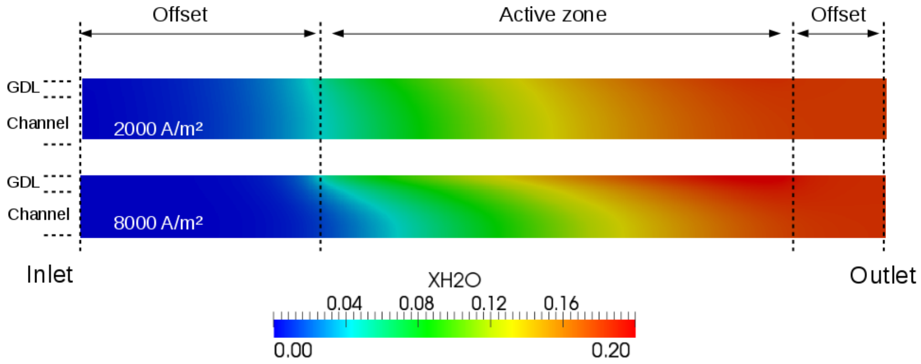

Figure 3.10: Comparison of mole fraction distribution of water vapour at low- (2000 Am^{-2}) and high (8000 Am^{-2}) mean current densities on Plane A.

ρ_{air} = density of air at 160 °C (g m^{-3})
λ = stoichiometrical factor (-)
F = Faraday constant (C mol^{-1})
n = number of electron (-)

In the simulations, $\mathbf{U}_{inlet}$ at 2000 Am^{-2} is 0.036 m/s; at 8000 Am^{-2} is 0.144 m/s. The mass balance between inlet and outlet is checked according to Eq. (3.1) to Eq. (3.3). As shown in in Figure 3.11, the velocity at 2000 Am^{-2} is lower than at 8000 Am^{-2}. Because with the same stoichiometric factor λ = 2/2, the inlet velocity at 8000 Am^{-2} is four times of which at 2000 Am^{-2}. However, the velocity distributions of the both operating points have similar trends: the largest velocity occurs in the middle of the channel and decreases towards the wall. This parabolic velocity profile in the gas channel is as expected. In the GDL, the velocity is almost zero. The typical direction profile of the velocity in the GDL is shown in Figure 3.12, the magnitude of the velocity in the GDL is in the range of 1×10^{-4} m/s - 3×10^{-4} m/s at 8000 Am^{-2}, which is three orders of magnitude lower than which in the channel. The Péclet number of Eq. (3.5) in the GDL is in the range of 0.001 - 0.003 (with the geometric characteristic length of 0.3 mm and multi-component diffusivity of 2.98 $\times10^{-5}$ m^2 s^{-1}), which means that the convection term is neglectable in the GDL.

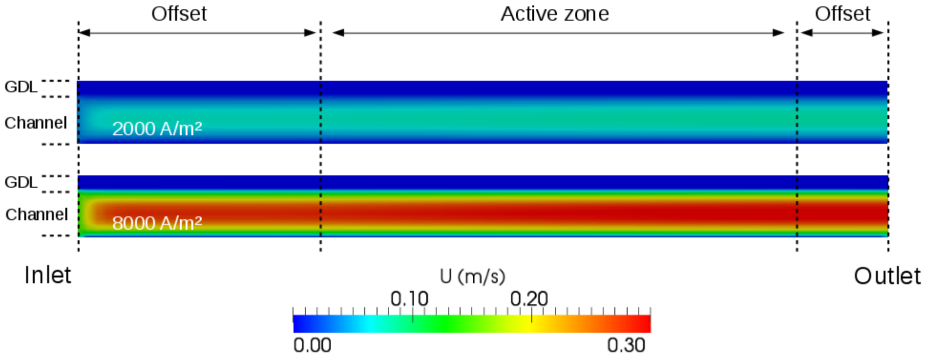

Figure 3.11: Comparison of magnitude of velocity distribution of gas mixture at low- (2000 Am^{-2}) and high (8000 Am^{-2}) mean current densities on Plane A.

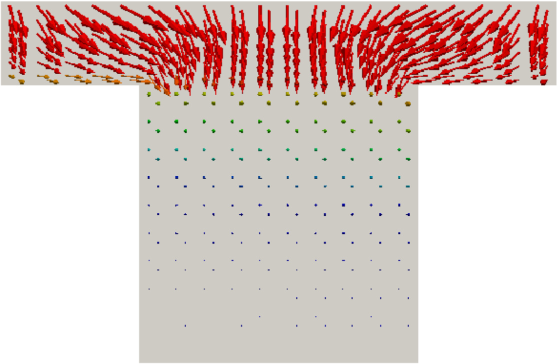

Figure 3.12: The velocity vectors in the GDL at low- (2000 Am^{-2}) mean current density. Position: the cross section in the middle of the channel.

Figure 3.13 shows the temperature profiles of plane A. The fixed value boundaries (433 K) are assumed on the outer walls. At 2000 Am^{-2}, the temperature on plane A varies from 433 K to 433.8 K. The heat source is at the electrolyte-GDE interface due to the exothermic reaction and the Joule heating. The little difference of temperature shows that, for low mean current densities, if the fixed temperature can be held on the outer wall of the cell, the internal field of an HT-PEFC will be in the quasi-isothermal state. On the other hand, the temperature on plane A varies from 433 K to 436.7 K at 8000 Am^{-2}. This result is expected because more heat is produced when more current is generated. One can also see that by the both simulations, increasing of the temperature occurs before the entry of the active zone, this can be explained as the heat transfer: the reaction zone is warmer than the inlet boundary, a part of heat flows from the reaction zone towards the inlet zone. It is worth to note that, in the simulations, the heat is produced in the electrolyte, the heat flux flows towards both anode and cathode outer walls. However, the results on the anode side are not shown in this section.

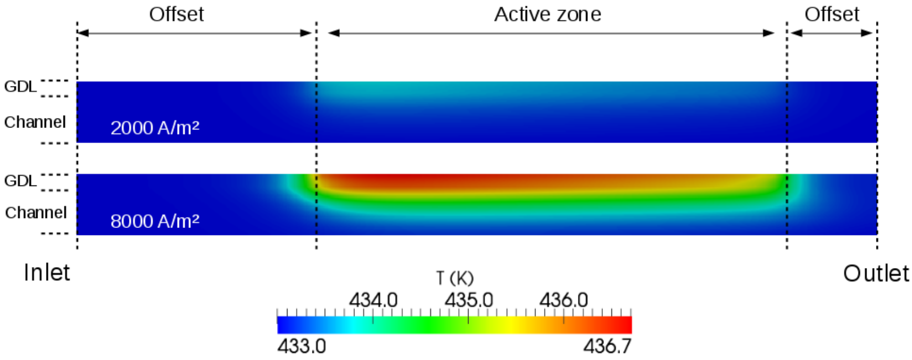

Figure 3.13: Comparison of temperature distribution at low- (2000 Am^{-2}) and high (8000 Am^{-2}) mean current densities on Plane A.

In the basic model, the local distribution of oxygen on the electrolyte-GDE interface (plane B) has a significant influence on the cell performance since the ORR is assumed to occur there. According to Equation 2.19 and Equation 2.17, both Nernst potential and activation overpotential are functions of the mole fraction of oxygen. The mole fraction of oxygen on plane B of the low- and high operating points are presented in Figure 3.14.

The oxygen mole fraction distributions of both operating points have similar trends:

- The mole fraction decreases along the flow direction.
- The mole fraction under the channels is higher than that under the ribs. This result is

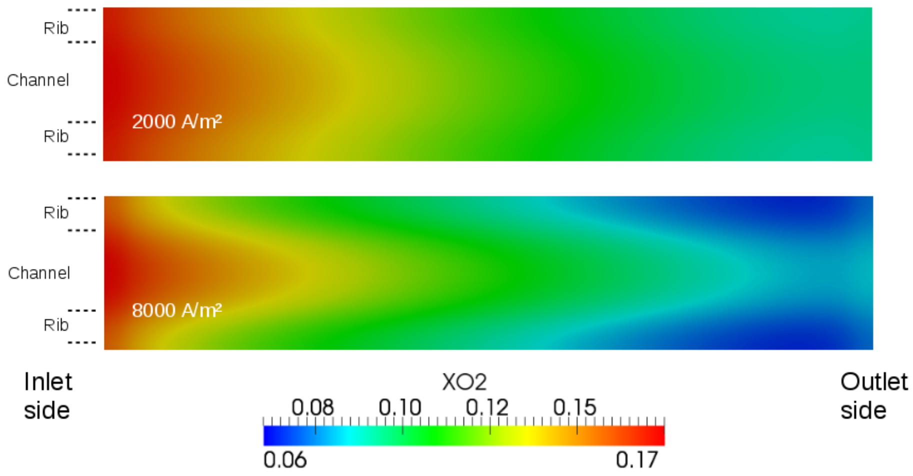

Figure 3.14: Comparison of mole fraction distribution of oxygen at low- (2000 Am^{-2}) and high (8000 Am^{-2}) mean current densities on Plane B.

expected because the diffusion distance under the channels is shorter than that under the ribs. This effect was reported by the previous modelling works of PEFC [70, 112] and HT-PEFC [80, 81].

However, the oxygen mole fraction at 2000 Am^{-2} is generally higher than at 8000 Am^{-2}: at 2000 Am^{-2}, the maximum value is $17.5\,\%$, the minimum value is $9.0\,\%$, and the mean value is $12.1\,\%$; at 8000 Am^{-2}, the maximum value is $17.4\,\%$, the minimum value is $6.4\,\%$, and the mean value is $10.5\,\%$. This result is expected. To satisfy the mass balance, the flux of oxygen must equal the consumed flux of oxygen of the electrochemical reaction. For instance, the diffusion flux of oxygen at 8000 Am^{-2} is four times of which at 2000 Am^{-2}, because the reaction requires four times of oxygen molecules. According to Fick' law, the concentration gradient in a diffusion media dominates the diffusion flux. In the cathode GDL of an HT-PEFC, the oxygen molecules diffuse from the bulk side to the reaction side. If the mole fractions on the bulk side are the same, the higher the current is, the lower the mole fraction on the reaction side is, to guarantee a greater gradient. Therefore, the reaction side oxygen mole fraction at 8000 Am^{-2} is lower than at 2000 Am^{-2}. This phenomenon was also reported by the previous research [131]. By the extremely high mean current density, X_{O_2} will go down to the near-zero value and can not further reduce. In practice, it may lead a large concentration overpotential because of the shortage of oxygen.

Another result is that, on plane B, the distributions of the oxygen mole fraction at these two operating points are different. For analysing this difference, four sampling lines are created, as shown in Figure 3.15. The sampling line 1 is used to present the mole fraction of oxygen on the electrolyte-GDE interface in the flow direction, the sampling line 2-4 are used to introduce the mole fraction of oxygen on the electrolyte-GDE interface in the in-plane direction (channel-to-rib direction).

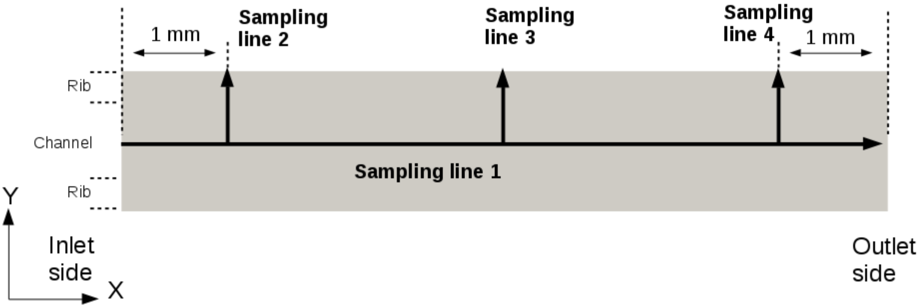

Figure 3.15: Sketch of sampling lines to present the distributions of the oxygen mole fraction on Plane B.

The mole fractions of oxygen in the flow direction (sampling line 1) are presented in Figure 3.16. As shown, the oxygen mole fraction at 2000 Am^{-2} is higher than that at 8000 Am^{-2}. The mole fractions of oxygen in the channel-to-rib direction (sampling line 2-4) are presented in Figure 3.17. As shown, at the both operating points, the oxygen mole fraction in the channels is higher than that in the ribs. However, this channel-rib effect on the distribution of oxygen at high current is more obvious than that at low current: the gradients of the oxygen mole fraction at 8000 Am^{-2} are higher than that at 2000 Am^{-2}, in all three positions.

Figure 3.18 and Figure 3.19 show the current density distributions on plane B, at the low- and high current densities. At the operating point of 2000 Am^{-2}, the calculated mean value of the current density on plane B is 1999.92 Am^{-2}; at the operating point of 8000 Am^{-2}, the calculated mean value of the current density on plane B is 7999.98 Am^{-2}. The errors are below 0.08 Am^{-2}.

The distribution of current density has the similar trends as oxygen mole fraction distribution. One can see the current density decreases along the flow direction. One can also find the channel-rib effect: more current is generated under the channel than ribs because the mole fraction of oxygen under the channel is higher than ribs. Additionally, the local current densities are not evenly distributed around the mean current density: at 2000 Am^{-2}, the current densities of 57 % area are below the mean current density; at 8000 Am^{-2}, the current densities of 52 %

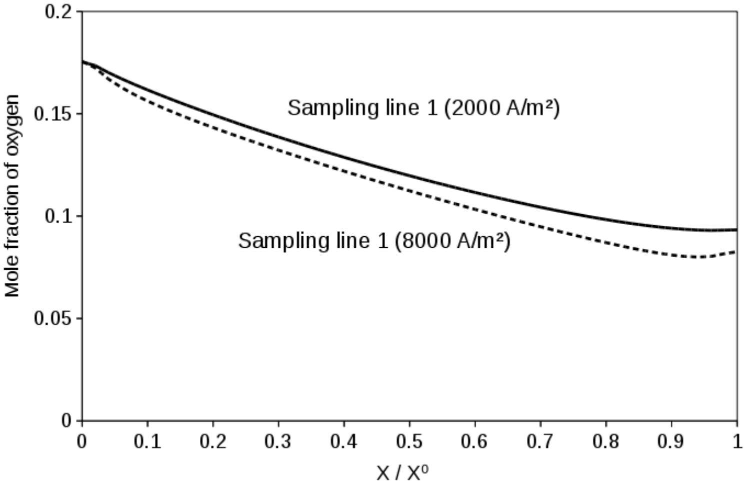

Figure 3.16: Comparison of mole fraction distribution of oxygen along sampling line 1 at low- (2000 Am^{-2}) and high (8000 Am^{-2}) mean current densities on Plane B. λ = 2/2. The index 0 indicates the inlet side while the index 1 indicates the outlet side. X^0 = 10 mm (the length of the active area).

area are below the mean current density. This effect is caused by the different distributions of the species at the electrolyte-GDE interface at low and high current.

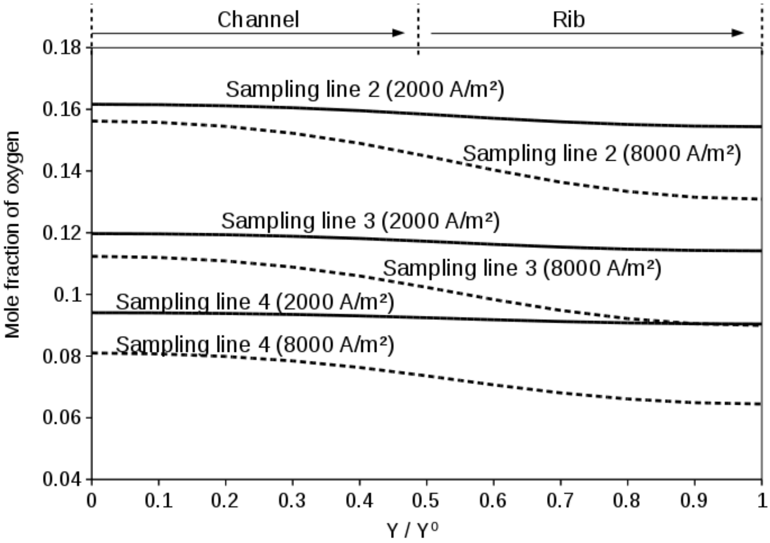

Figure 3.17: Comparison of mole fraction distribution of oxygen along sampling lines 2-4 at low- (2000 Am^{-2}) and high (8000 Am^{-2}) mean current densities on Plane B. λ = 2/2. The index 0 indicates the middle of the channel while the index 1 indicates the side of the rib. Y^0 = 1 mm (the half width of the channel + the width of one rib).

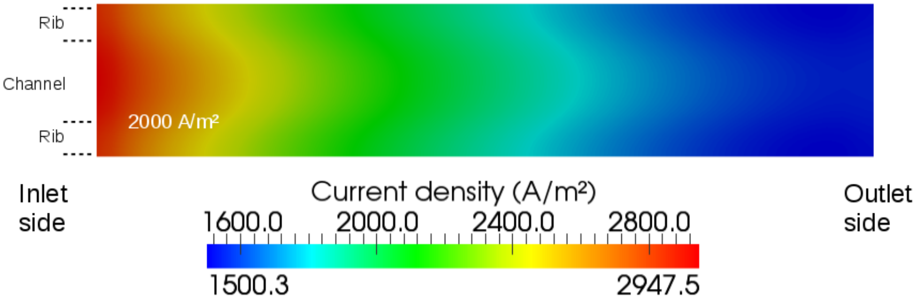

Figure 3.18: Current density distribution at low (2000 Am^{-2}) mean current densities on Plane B.

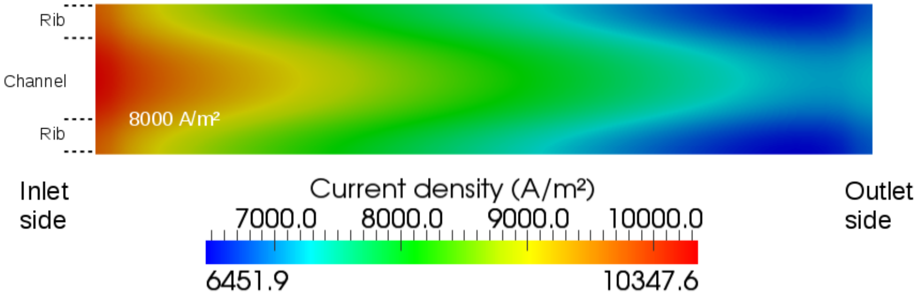

Figure 3.19: Current density distribution at high (8000 Am^{-2}) mean current densities on Plane B.

Summary

The numerical results of the basic model were presented in this section. The activation loss and the ohmic loss are shown in the polarisation curve. However, the diffusive limitation is not shown with the basic model.

The local distributions of the species mole fraction, velocity, temperature and current density were presented on two cross-sectional planes on the cathode side. On the plane which was in the middle of the channel and perpendicular to the MEA, the operation with high current had a higher velocity and higher temperature compared to the low current. The mole fraction of oxygen in the middle of the channel at the both high- and low current decrease along the channel, the numerical results showed the similar trend as the analytical results. On the electrolyte-GDE interface, the high current case had a lower concentration of oxygen compare to the low current case. The channel-rib effect on current density distribution was also presented in both cases.

These results showed the benefit of the 3-D CFD simulation: the local information of the whole flow field can be achieved. That provides the knowledge to understand the physical aspects and to optimise the design of the fuel cell.

3.2.2 Compression effect of GDL (model I)

As mentioned in section 1.3, during the assembly of an HT-PEFC, the GDL is usually compressed by the ribs of the bipolar plates, depending on the clamping pressure. For identifying this compresstion effect, we may first define the engineering strain:

$$\Lambda = 1 - \frac{l_G}{l_{G0}} \tag{3.7}$$

where
Λ = engineering strain (-)
l_G = average thickness of the GDL after compression (m)
l_{G0} = average thickness of the GDL before compression (m)

In this section, the single channel pair geometries with the different engineering strains Λ were constructed to simulate the compressing effect of the GDL. Figure 3.20 shows a synchrotron X-ray tomographic study of the GDLs, with the different values of Λ: $0\,\%$, $10\,\%$, $18\,\%$ and $29\,\%$. Four meshes were created according to the profiles of these GDLs. The cross sections of these meshes are showed in Figure 3.21. The blue regions indicate the GDL, the grey regions indicate the gas channel. The thickness of the GDL under the ribs in these four meshes were set to 300μm, 270μm, 246μm and 213μm. The curves between GDL and channel of these four meshes were fitted from Figure 3.20. The GDL was split into two regions: the region under the channel and the region under the rib, as shown in Figure 3.22. The porosities and permeabilities of different engineering strains in these two regions are presented in Tabel 3.3 and Table 3.4. The previous research reported that the value of the mean geometric tortuosity of the GDL ranges between 1.42 and 1.50 [107]. In this work, the mean geometric tortuosity was assumed to be constant: τ=1.50. The operating conditions of the simulations were same as the Table 3.2. The basic model was employed for the calculations.

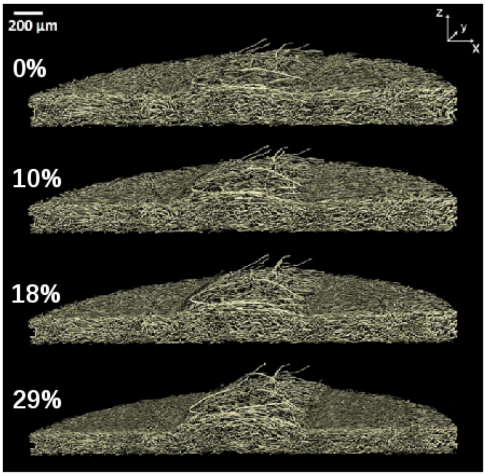

Figure 3.20: GDL sample compressed by a channel-rib profile. From top to bottom, the engineering strain are 0 %, 10 %, 18 %, and 29 %. Reprinted from [107], with permission from Elsevier.

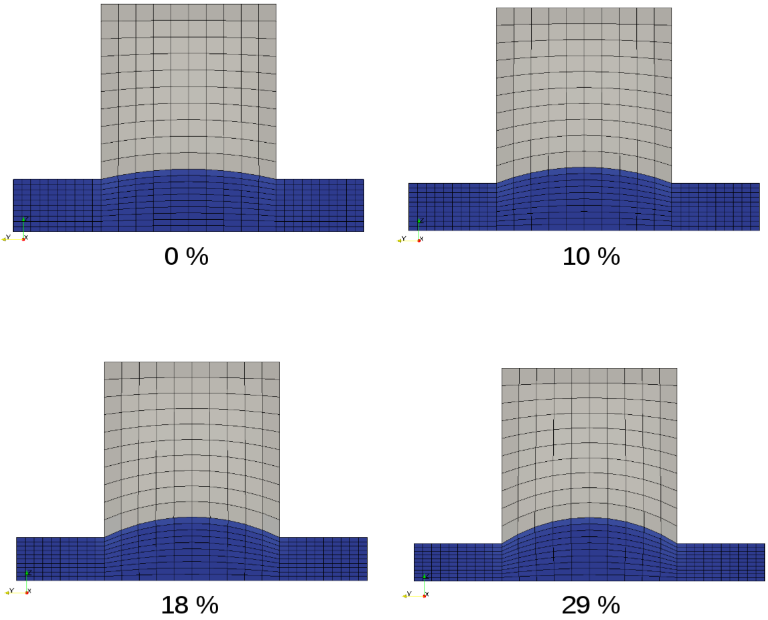

Figure 3.21: Cross section of the meshes corresponding to the engineering strains: 0 %, 10 %, 18 %, and 29 %.

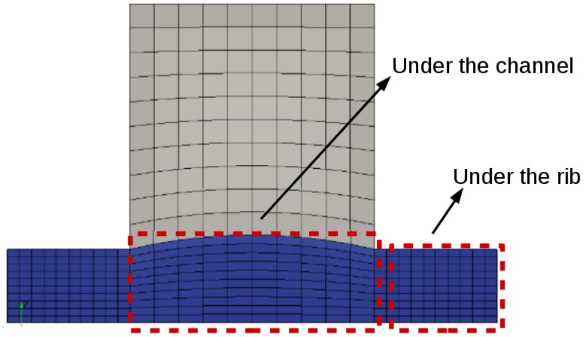
Under the channel
Under the rib

Figure 3.22: The regions of GDL under the channel and the rib.

Table 3.3: Porosities of the GDL by different engineering strains [107].

Engineering strain	Porosity (under the channel)	Porosity (under the rib)
0 %	80.2	76.3
10 %	79.5	74.2
18 %	79	71.6
29 %	78.8	69.5

Table 3.4: Aninsotropic permeabilities under the channel/rib [132].

	Permeability under the channel (m^2)		Permeability under the rib (m^2)	
Engineering strain	In-plane	Through-plane	In-plane	Through-plane
0 %	16.93×10^{-12}	8.22×10^{-12}	16.93×10^{-12}	8.22×10^{-12}
10 %	16.93×10^{-12}	8.22×10^{-12}	13.82×10^{-12}	6.59×10^{-12}
18 %	16.93×10^{-12}	8.22×10^{-12}	11.10×10^{-12}	5.16×10^{-12}
29 %	16.93×10^{-12}	8.22×10^{-12}	8.49×10^{-12}	3.82×10^{-12}

The mass balances of the species for the anode side and the cathode side of the simulations with the different engineering strains are checked according to Eq. (3.1) to Eq. (3.3). The relative mass transfer errors of the species are presented in Table 3.5.

Two planes at the cathode side are employed to display the local information: one is the electrolyte-GDE interface, another is the cross-sectional plane at the middle position of the channel length. Figure 3.23 shows the current density distributions on the electrolyte-GDE interface of the geometries with the engineering strains of 0 %, 10 %, 18 % and 29 %. The mean current densities of these four cases were the same: I_{mean} = 6000 Am^{-2}. It can be seen that, at the inlet region, the current density with the high engineering strain is greater than that with the low engineering strain; at the outlet region, the current density with the high engineering strain is lower than that with the low engineering strain. This trend is also presented in Table 3.6: the deviation of the minimum value and the maximum value by engineering strain 0 % is 5374 Am^{-2}, this deviation from engineering strain 29 % is 6983 Am^{-2}. However, simulations show that the cell voltage with the high engineering strain 29 % presented no significant difference with the low high engineering strain 0 %, the concentration overpotential may not occur by a engineering strain below 29 % at 6000 Am^{-2}.

Figure 3.24 presents the mole fraction of oxygen (X$_{O_2}$) distribution on the cross-sectional plane

Table 3.5: Relative mass transfer errors of the species by different engineering strains. The mean current density of cases was 6000 Am^{-2}.

Engineering strain	δ_{O_2}	δ_{H_2}	δ_{H_2O}	δ_{N_2}
0%	1.29%	0.16%	0.08%	-1.31%
10%	1.30%	0.16%	0.08%	-1.32%
18%	1.32%	0.17%	0.07%	-1.34%
29%	1.35%	0.17%	0.08%	-1.37%

at the middle position of the channel length. It is observed that, with increasing of the engineering strain:

- X$_{O_2}$ in the gas channels of the four cases are nearly identical.
- With the higher engineering strain the thickness of the GDL is smaller. It leads to the shortage of the oxygen under the rib. That explains the big deviation of the current density by high engineering strain.

These effects on the oxygen distribution are in agreement with previous modelling work [89]. In [89], at 6000 Am^{-2}, the cell voltage of the cell with a engineering strain of $15\,\%$ is around 0.05 V lower than the uncompressed cell, that difference was considered as the concentration overpotential due to the compressed GDL.

Figure 3.25 presents the mole fraction of oxygen distribution on the other cross-sectional plane, which is in the middle of the channel and perpendicular to the MEA. One can see that the distributions of X$_{O_2}$ of the four cases are similar. To present the compression effect on the mole fraction of oxygen precisely, three sampling lines (A) at the middle of the channel (B) at the bottom-middle of the GDL and (C) at the bottom-corner of the GDL were taken at the cathode side, as shown in Figure 3.26. The mole fraction of oxygen was plotted over these sampling lines and presented from Figure 3.27 to Figure 3.29. It is observed that:

- X$_{O_2}$ over the sampling line A of the four cases are nearly identical.
- X$_{O_2}$ over the sampling line B of the four cases are again nearly identical.
- X$_{O_2}$ over the sampling line C of the four cases are different, the mole fractions of oxygen decrease with the increasing of the engineering strain.

It shows that the mole fraction in the GDL under the rib is influenced more significantly rather than other places by engineering strain.

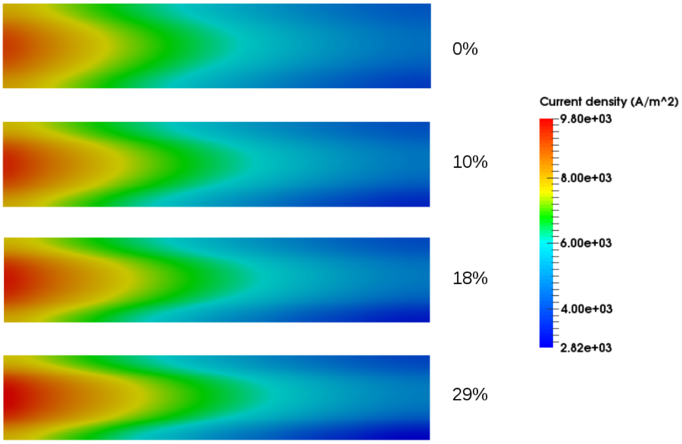

Figure 3.23: Current density distributions at the electrolyte-GDE interfaces with the GDL engineering strains of $0\,\%$, $10\,\%$, $18\,\%$ and $29\,\%$. The mean current density of cases was 6000 Am^{-2}.

Table 3.6: Current densities and cell voltages at the electrolyte-GDE interfaces with the GDL engineering strains of $0\,\%$, $10\,\%$, $18\,\%$ and $29\,\%$.

Engineering strain	Current density (Am^{-2})			Cell voltage (V)
	min	mean	max	
0%	3744	6000	9118	0.595
10%	3378	6000	9401	0.592
18%	3172	6000	9559	0.589
29%	2821	6000	9804	0.586

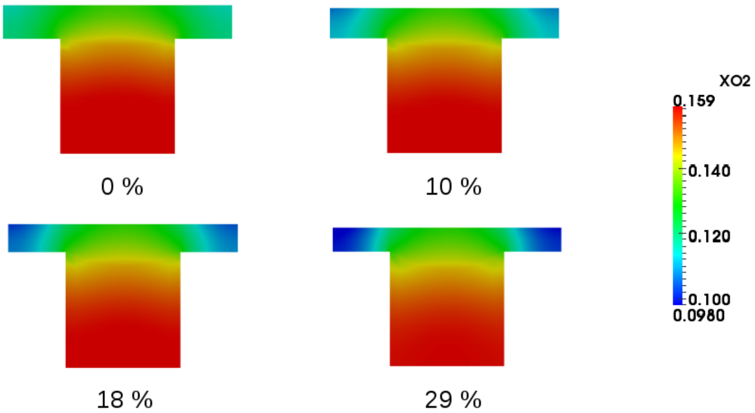

Figure 3.24: Mole fraction of oxygen on the cross sections of the cathode channel and GDL with the GDL engineering strains of $0\,\%$, $10\,\%$, $18\,\%$ and $29\,\%$. The mean current density of cases was 6000 Am^{-2}.

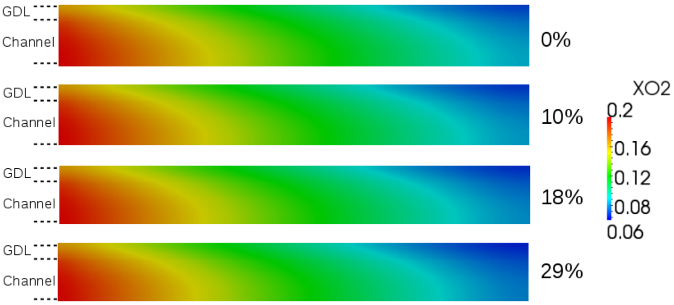

Figure 3.25: Mole fraction of oxygen on the cross-sectional plane, which is in the middle of the channel and perpendicular to the MEA, with the GDL engineering strains of $0\,\%$, $10\,\%$, $18\,\%$ and $29\,\%$. The mean current density of cases was 6000 Am^{-2}.

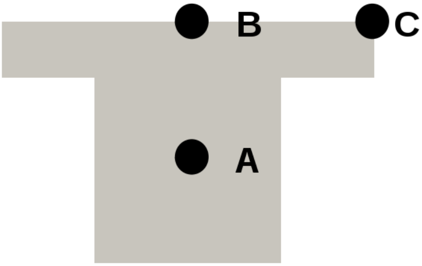

Figure 3.26: Three sampling lines in the flow field of the cathode side: (A) at the middle of the channel (B) at the top-middle of the GDL and (C) at the top-corner of the GDL.

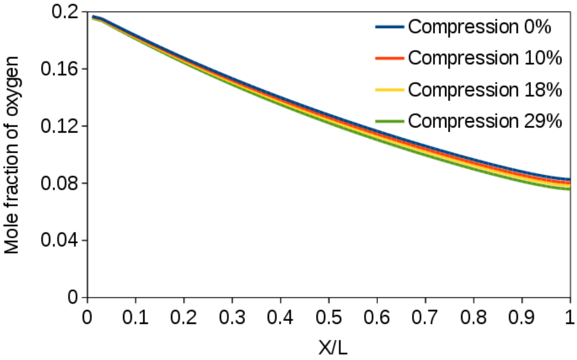

Figure 3.27: The mole fraction of oxygen over the sampling line A.

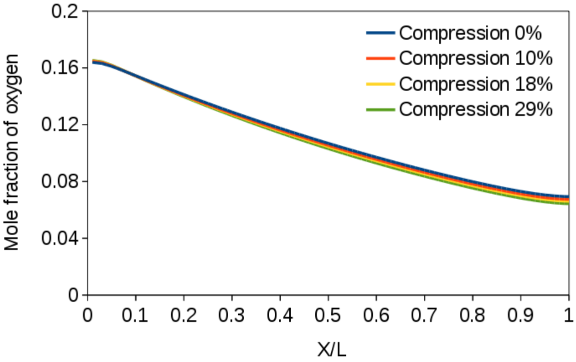

Figure 3.28: The mole fraction of oxygen over the sampling line B.

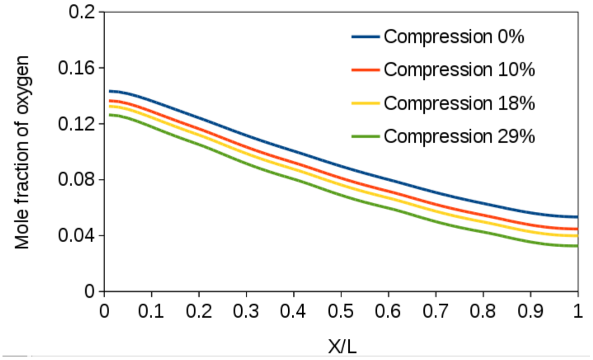

Figure 3.29: The mole fraction of oxygen over the sampling line C.

Summary

The compression effect of the GDL is examined with the basic model in this section. Four meshes with a single straight channel geometry were made corresponding to X-ray tomographic photograph of the GDL samples. The properties of the GDL under the channel and that under the rib were taken from the literature. With the numerical calculation, it was found that the engineering strain affects the distribution of the oxygen and current density. With the high engineering strain, the range of the current density distribution is wider. However, the cell voltage with the high engineering strain showed no big difference with the low high engineering strain.

In the middle of the channel or under the channel, the mole fractions of oxygen has no obvious correlation with the engineering strain; under the ribs, the mole fractions of oxygen decreases with the increasing of the engineering strain.

3.2.3 Multicomponent diffusion model (model IV)

As mentioned in section 2.5, the diffusion flux of one species in the gas mixture in the flow field of the HT-PEFC can be calculated either by Fick's law or by a Maxwell-Stefan formulation. In this section, the local performances of the two models are presented.

Validation of Maxwell-Stefan model on 1-D Stefan tube problem

The matrix form of the Maxwell-Stefan equations (Eq. 2.55) can be validated by solving a 1-D Stefan tube problem, for a ternary mixture. The schematic diagram of the Stefan tube problem is shown in Figure 3.30. The mixture in the Stefan tube has two phases: the gas phase and the liquid phase. The binary liquid is at the bottom of the tube. This liquid consists of acetone and methanol. The vapour of acetone and methanol diffuses along x direction due to evaporation. At the top of the tube, acetone and methanol are taken by air flow. The mole fractions of acetone and methanol are zero at the top boundary.

In this study, the mole fraction distributions of acetone, methanol and air inside the Stefan tube are solved using the multicomponent diffusion model and compared with the numerical solution given by Taylor and Krishna [126, p.23]. Physical properties and boundary conditions are given in Table 3.2.3. The values of binary diffusion coeffients are: D_{12} = 8.48×10^{-6} m^{2}s^{-1}, D_{13}= 13.72×10^{-6} m^{2}s^{-1} and D_{23}= 19.91×10^{-6} m^{2}s^{-1}, which are taken from [126, p.22].

Molar fractions for the 3 species are shown in Figure 3.31. One can see that the model in this work using the Maxwell-Stefan formulation shows the agreement with the numerical results from Taylor and Krishna.

Table 3.7: Labels and boundary conditions of Stefan tube simulation

Component	Label	X_i on top	X_i on bottom
Acetone	1	0	0.319
Methanol	2	0	0.528
Air	3	1	0.153

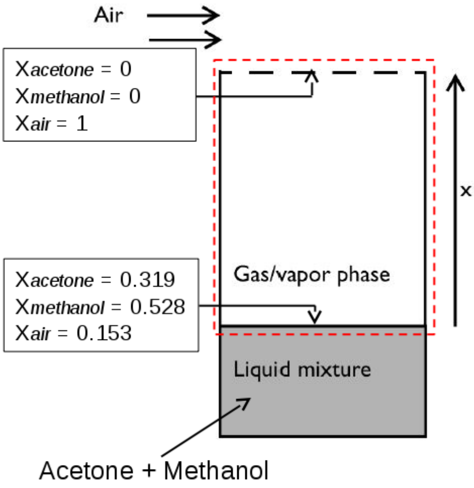
Air
Xacetone = 0
Xmethanol = 0
Xair = 1
x
Xacetone = 0.319
Xmethanol = 0.528
Xair = 0.153
Gas/vapor phase
Liquid mixture
Acetone + Methanol

Figure 3.30: Schematic diagram of a Stefan tube [133].

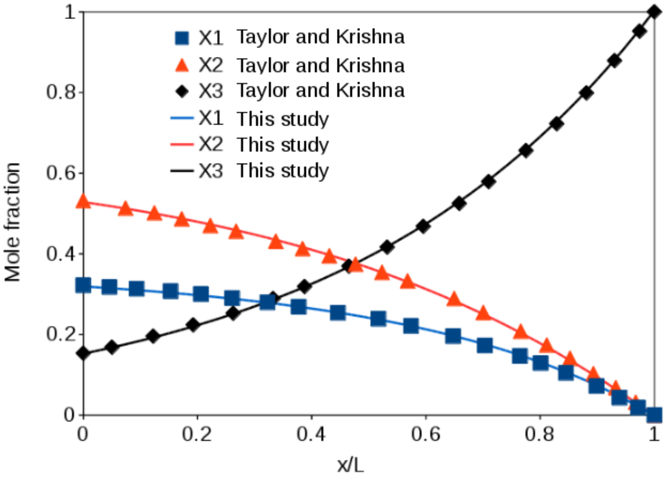

Figure 3.31: Comparison of mole fractions in Stefan tube with numerical solution from Taylor and Krishna. Components: acetone($X1$), methanol($X2$) and air($X3$).

Comparison of Fick's law and Maxwell-Stefan formulations on the single channel pair with the H_2/air system

In this section, the numerical results of the basic model (with Fick's law) and the multicomponent diffusion model on the single channel pair geometry are compared. The operating conditions of the simulations are the same as the Table 3.2. The operating point corresponds to a mean current density of 4000 Am^{-2}. These two models use the same electrochemical equations, the parameters are listed in Table 2.4.

The mass balances of the species for the anode side and the cathode side of the two models are checked according to Eq. (3.1) to Eq. (3.3). For the basic model, the relative mass transfer errors of the species are: δ_{O_2} = 0.12 %, δ_{H_2} = 0.02 %, δ_{H_2O} = 0.04 %, δ_{N_2} = -0.02 %. For macro-homogeneous model, the relative mass transfer errors of the species are: δ_{O_2} = 0.48 %, δ_{H_2} = 0.01 %, δ_{H_2O} = 0.08 %, δ_{N_2} = -0.37 %.

As mentioned before, the mole fraction of oxygen on the cathode side is important as it affects the activation overpotential for an HT-PEFC. Therefore, this quantity is employed in this section to compare the results of the simple Fickian and Maxwell-Stefan (generalized Fick's law) formulations. Figure 3.32 shows the numerical results of the mole fraction distribution of oxygen obtained using the Fick's law and the Maxwell-Stefan equations. One can see that the results for the Fick's law and the Maxwell-Stefan formulation are similar. The calculations suggest that there is little difference between the numerical results of Fick's law and those of Maxwell-Stefan equations (generalized Fick's law), the difference in mean mole fraction at the electrolyte-GDE interface being only around 0.32 %.

Figure 3.33 shows the numerical results of the current density distribution obtained using the Fick's law and the Maxwell-Stefan equations. Similar to the mole fraction distribution of oxygen, the current density distribution for the Fick's law and the Maxwell-Stefan formulation are also near-identical.

The magnitude of the off-diagonal term of the multi-component diffusion coefficients is indicative of the deviation from Fick's law. If these terms, Equation 2.51, are zero; the Maxwell-Stefan equations reduce to Fick's law. This happens when all of the binary diffusivities are equal. For convenience, labelling oxygen, water and nitrogen as 1, 2 and 3, respectively, calculated average binary diffusion coefficients in the channel and GDL are presented in Table 3.8.

As shown, the binary diffusivities are not identical but deviate by around 21 %. Using these binary diffusivities, the multi-component diffusion coefficients can be obtained either by Wilke's formulation Equation 2.15 or by the matrix form of the Maxwell-Stefan formulation Equations 2.55.

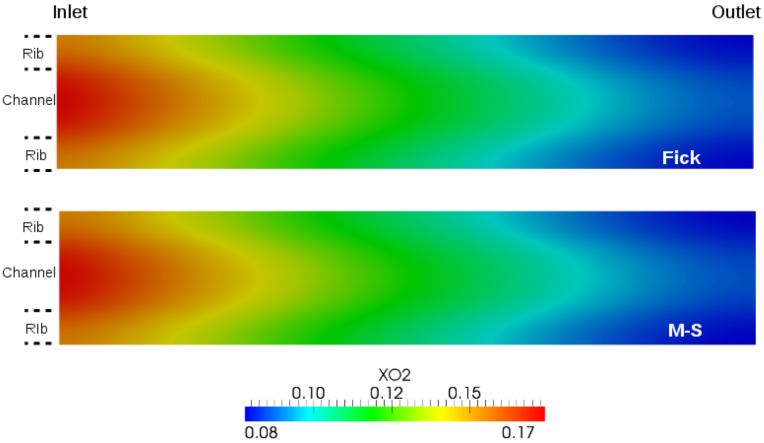

Figure 3.32: Mole fraction of oxygen at the electrolyte-GDE interfaces: comparison of Fick's law and Maxwell-Stefan formulation.

Table 3.8: Binary diffusivities in the channel and GDL at the cathode side. Components of the mixture: oxygen (1), water (2) and nitrogen (3).

	Channel	GDL
D_{12}	3.98×10^{-5} m^2s^{-1}	1.96×10^{-5} m^2s^{-1}
D_{13}	4.99×10^{-5} m^2s^{-1}	2.45×10^{-5} m^2s^{-1}
D_{23}	5.08×10^{-5} m^2s^{-1}	2.49×10^{-5} m^2s^{-1}

In the case of HT-PEFC cathode, the multi-component diffusion coefficients obtained by Wilke's formulation in the channel and GDL are presented in Table 3.9. The multi-component diffusion coefficients obtained by Maxwell-Stefan formulation in the channel and GDL are presented in Table 3.10. It is important to note that only two fluxes are required for a ternary mixture.

So off-diagonal values in the channels are typically 6 % or less of diagonal values, and even less so within the GDL. Both sets of results (Fick and Stefan Maxwell) generated essentially the same global and local concentrations profile of oxygen: decreasing in the main direction of the flow; with the under the channel higher than that under the rib.

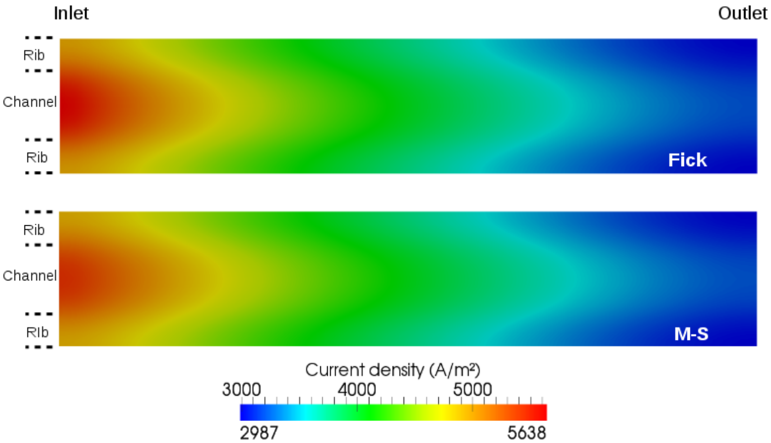

Figure 3.33: Current density distribution at the electrolyte-GDE interfaces: comparison of Fick's law and Maxwell-Stefan formulation.

Table 3.9: Multi-component diffusion coefficients of Fick's law in the channel and GDL at the cathode side. Components of the mixture: oxygen (1), water (2) and nitrogen (3).

	Channel	GDL
D^0_{11}	4.09×10^{-5} m^{2}s^{-1}	1.94×10^{-5} m^{2}s^{-1}
D^0_{22}	5.00×10^{-5} m^{2}s^{-1}	1.81×10^{-5} m^{2}s^{-1}

Table 3.10: Diagonal and off-diagonal terms of Maxwell-Stefan formulation in the channel and GDL at the cathode side. Components of the mixture: oxygen (1), water (2) and nitrogen (3).

	Channel	GDL
	diagonal	diagonal
D^0_{11}	3.20×10^{-5} m^{2}s^{-1}	1.51×10^{-5} m^{2}s^{-1}
D^0_{22}	4.01×10^{-5} m^{2}s^{-1}	1.81×10^{-5} m^{2}s^{-1}
	off-diagonal	off-diagonal
D^0_{12}	-1.96×10^{-6} m^{2}s^{-1}	-3.52×10^{-7} m^{2}s^{-1}
D^0_{21}	3.39×10^{-8} m^{2}s^{-1}	5.64×10^{-9} m^{2}s^{-1}

Comparison of Fick's law and Maxwell-Stefan formulations on single channel HT-PEFC with the reforming gas/air system

In this section, the performances of Fick's law and Maxwell-Stefan formulations on HT-PEFC with the reforming gas/air system are presented. Similar to the last section, the single channel pair geometry was employed. The reforming gas is fed from the inlet of the anode channel, and the air is fed from the inlet of the cathode channel, both the stoichiometrical factor on both sides is 2. The boundary of temperature with a fixed value of 160 ℃ is set on the outer walls on both anode and cathode sides. The reforming gas consists essentially of hydrogen, nitrogen, water vapour, carbon dioxide and carbon monoxide. However, in this study, the carbon monoxide is not considered since the CO poisoning effect is not modelled in this thesis and the mole fraction of CO at the entry of the anode of the HT-PEFC with the reforming gas/air system is usually small (in the order of $1\,\%$ [5]). In this study, the nitrogen, water vapour and carbon dioxide are considered as inert gases. The operating conditions of the simulations are listed in Table 3.11. The boundaries of the gases are calculated from [5]. The operating point corresponds to a mean current density of 4000 Am^{-2}.

Table 3.11: Operating conditions for the comparison of Fick's law and Maxwell-Stefan formulations with the reforming gas/air system.

Parameter	Symbol	Value	Unit
Operating temperature	T	433	K
Pressure at anode outlet	p_a	101325	Pa
Pressure at cathode outlet	p_c	101325	Pa
Mass fraction of H_2 at anode inlet	Y_{H_2}	0.034	
Mass fraction of H_2O at anode inlet	Y_{H_2O}	0.212	
Mass fraction of N_2 at anode inlet	Y_{N_2}	0.416	
Mass fraction of CO_2 at anode inlet	Y_{CO_2}	0.338	
Mass fraction of O_2 at cathode inlet	Y_{O_2}	0.230	
Mass fraction of N_2 at cathode inlet	Y_{N_2}	0.770	
Anode stoichiometric ratio	λ_a	2	
Cathode stoichiometric ratio	λ_c	2	

The mass balances of the species for the anode side and the cathode side of the two models are checked according to Eq. (3.1) to Eq. (3.3).

For the basic model, the relative mass transfer errors of the species are: δ_{O_2} = 0.06 %, δ_{H_2} = 0.01 %, δ_{H_2O} = 0.05 %, δ_{N_2} = -0.01 %, δ_{CO_2} = 0.00 %. For macro-homogeneous model, the relative mass transfer errors of the species are: δ_{O_2} = 0.27 %, δ_{H_2} = -0.01 %, δ_{H_2O} = 0.03 %, δ_{N_2} = 0.25 %, δ_{CO_2} = -0.03 %.

Different with the last section, the numerical results on the anode side are presented. In the HT-PEFC with the reforming gas/air system, the mole fraction of hydrogen (X_{H_2}) is not always 100 %. The local distribution of X_{H_2} on the electrolyte-GDE interfaces of the anode side is important since it affects the Nernst potential (2.19). It is worth to note that, in this thesis, it is assumed that X_{H_2} does not affect the kinetics. In practice, the kinetics of the hydrogen oxidation reaction (HOR) affects the kinetics seriously when the presence of the CO poisoning. However in this thesis, the CO poisoning effect is not modelled. In this case, the HOR becomes neglectable compared to ORR [29, p.582].

Figure 3.34 shows the results of the mole fraction distribution of hydrogen, water, carbon dioxide and nitrogen at the electrolyte-GDE interfaces obtained using the two diffusion models. Similar to the last section, the calculations suggest that there is a little difference between the numerical results of Fick's law and those of Maxwell-Stefan equations. The difference in the mean mole fraction of hydrogen, water, carbon dioxide and nitrogen at the electrolyte-GDE interface are shown in Table 3.12. One can see that the biggest difference is only 0.4 % by X_{N_2}.

Table 3.12: The mole fraction of hydrogen, water, carbon dioxide and nitrogen at the electrolyte-GDE interface.

	X_{H_2}	X_{H_2O}	X_{CO_2}	X_{N_2}
Fick's law	23.830 %	26.106 %	17.056 %	33.001 %
Maxwell-Stefan	23.836 %	26.489 %	17.071 %	32.604 %

We may label hydrogen, water, carbon dioxide and nitrogen as 1, 2, 3 and 4. The calculated average binary diffusion coefficients in the channel and GDL on the anode side are presented in Table 3.13. It is observed that the binary diffusivities are not identical but deviate by around 82 %. This significant deviation is due to the high diffusivity of hydrogen.

The multi-component diffusion coefficients obtained by Wilke's formulation in the channel and GDL are presented in Table 3.14 and the multi-component diffusion coefficients obtained by Maxwell-Stefan formulation in the channel and GDL are presented in Table 3.15. For the case of the quaternary mixture, three fluxes are required. The off-diagonal values in the channels are typically 28 % or less of diagonal values, and even less so within the GDL.

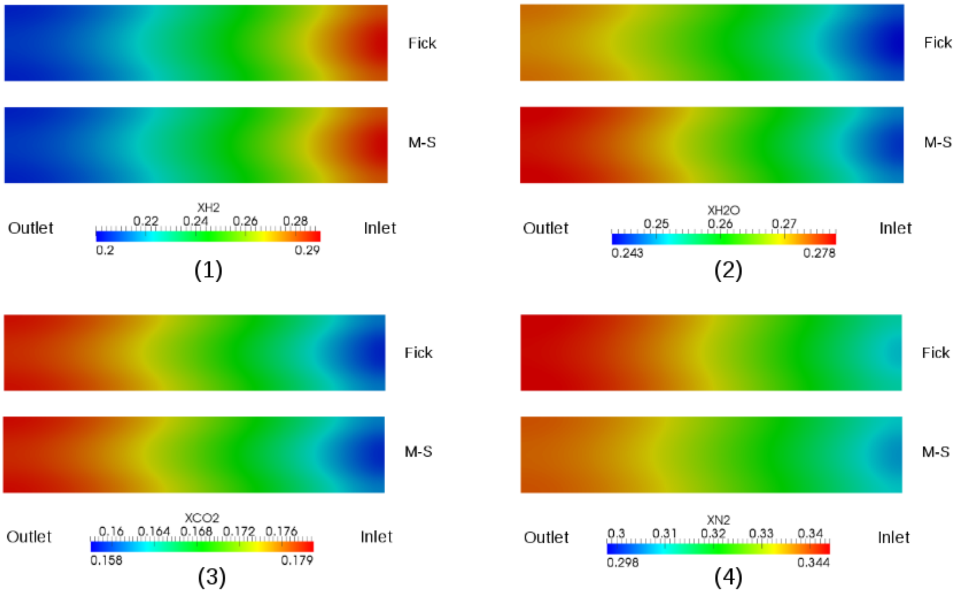

Figure 3.34: Mole fraction of (1) hydrogen, (2) water, (3) carbon dioxide and (4) nitrogen at the electrolyte-GDE interfaces: comparison of Fick's law and Maxwell-Stefan formulation.

Table 3.13: Binary diffusivities in the channel and GDL at the anode side. Components of the mixture: hydrogen (1), water (2), carbon dioxide (3) and nitrogen (4).

	Channel	GDL
D_{12}	1.75×10^{-4} m^{2}s^{-1}	8.59×10^{-5} m^{2}s^{-1}
D_{13}	1.28×10^{-4} m^{2}s^{-1}	6.31×10^{-5} m^{2}s^{-1}
D_{14}	1.50×10^{-4} m^{2}s^{-1}	7.40×10^{-5} m^{2}s^{-1}
D_{23}	4.04×10^{-5} m^{2}s^{-1}	1.99×10^{-5} m^{2}s^{-1}
D_{24}	4.98×10^{-5} m^{2}s^{-1}	2.45×10^{-5} m^{2}s^{-1}
D_{34}	3.14×10^{-5} m^{2}s^{-1}	1.54×10^{-5} m^{2}s^{-1}

Table 3.14: Multi-component diffusion coefficients in the channel and GDL at the anode side. Components of the mixture: hydrogen (1), water (2), carbon dioxide (3) and nitrogen (4).

	Channel	GDL
D^0_{11}	1.52×10^{-4} m^2s^{-1}	7.46×10^{-5} m^2s^{-1}
D^0_{22}	6.67×10^{-5} m^2s^{-1}	2.45×10^{-5} m^2s^{-1}
D^0_{33}	4.81×10^{-5} m^2s^{-1}	2.00×10^{-5} m^2s^{-1}

Table 3.15: Diagonal and off-diagonal terms of Maxwell-Stefan formulation in the channel and GDL at the anode side. Components of the mixture: hydrogen (1), water (2), carbon dioxide (3) and nitrogen (4).

	Channel	GDL
	diagonal	diagonal
D^0_{11}	1.51×10^{-4} m^2s^{-1}	7.45×10^{-5} m^2s^{-1}
D^0_{22}	6.21×10^{-5} m^2s^{-1}	2.71×10^{-5} m^2s^{-1}
D^0_{33}	4.43×10^{-5} m^2s^{-1}	1.94×10^{-5} m^2s^{-1}
	off-diagonal	off-diagonal
D^0_{12}	-2.08×10^{-6} m^2s^{-1}	-5.41×10^{-7} m^2s^{-1}
D^0_{13}	1.49×10^{-6} m^2s^{-1}	3.85×10^{-7} m^2s^{-1}
D^0_{21}	-4.27×10^{-5} m^2s^{-1}	-1.78×10^{-5} m^2s^{-1}
D^0_{23}	2.68×10^{-6} m^2s^{-1}	1.32×10^{-6} m^2s^{-1}
D^0_{31}	-1.54×10^{-5} m^2s^{-1}	-4.26×10^{-6} m^2s^{-1}
D^0_{32}	-2.82×10^{-6} m^2s^{-1}	-1.32×10^{-6} m^2s^{-1}

Summary

The numerical results of the multicomponent diffusion model were presented in this section. The Maxwell-Stefan formulation was validated with the Stefan-tube case. The numerical results showed good agreement with the numerical solution from Taylor and Krishna.

The single channel pair geometry was employed in the simulations. For the H_2/air system, it was found that the difference between Fick's law and Maxwell-Stefan formulation is small. For the reforming gas/air system, the simulations showed that there is still a tiny difference between this two diffusion models.

The binary diffusivities between the gases were calculated in this study. It was found that the binary diffusivities are not identical. However, it did not create a significant difference on the mass transfer equations (2.10) between Fick's model and Maxwell-Stefan model. The diagonal and off-diagonal terms of Maxwell-Stefan formulation were also given in this study. It was found that the off-diagonal terms are small compared to the diagonal terms which mean that the impact of the interaction between species was little on the diffusion flux.

Overall, this study suggested that at the typical operating point of HT-PEFC, the interaction between the gas species is small, both Fick's law (modified by Wilke's formulation) and Maxwell-Stefan formulation can be used to calculate the diffusion flux.

3.3 Simulations with the single cell with serpentine flow field

In Chapter 3.2, the single channel pair geometry is used to present the basic analysis of the local mass transfer of HT-PEFC. In this Chapter, the single cell with serpentine flow field is employed to run the simulations on the existing in-house HT-PEFC cell. The active area of the cell is 50 cm^2. First, the results of the basic model and the Macro-homogeneous model are validated and compared. Then, the results of the water transfer model are validated and discussed.

3.3.1 Basic model (model I) and Macro-homogeneous model (model II)

Polarisation curve

In this section, the polarisation curves of the basic model and the macro-homogeneous model are validated with the experimental data. Eight operating points with the mean current densities from 1000 A/m^2 to 8000 A/m^2 are taken to simulate the polarisation curve. The operating conditions of the simulations are same as the Table 3.2. The physical parameters of the basic model are listed in Table 2.4.

The sensitive electrochemical parameters of the macro-homogeneous are: the proton conductivity of the catalyst layer σ_t, the effective diffusivity of oxygen in the catalyst layer D_{CL}, and the thickness of the catalyst layer l_t. All these three parameters are fitting parameters since they are hard to measure in the in-situ situation. These parameters of the macro-homogeneous model are listed in Table 2.5. The experimental data are listed in Appendix 6.1.

Figure 3.35 compares the polarisation curves of the basic model, the macro-homogeneous model and experimental data. One can see that both basic model and macro-homogeneous model fit the experimental data well. The biggest deviation between the basic model and the experimental results is 2.2 $\times$ 10^{-2} V, it occurs at the lowest mean current density, i.e. 1000 A/m^2. The biggest deviation between the macro-homogeneous model and the experimental results is 1.5 $\times$ 10^{-2} V, it also occurs at 1000 A/m^2.

The above comparisons show that the macro-homogeneous model can predict the overall performance of the HT-PEFC as well as the basic model. Additionally, one can make a more detailed analysis on the overpotentials with the macro-homogeneous model. Here we recall

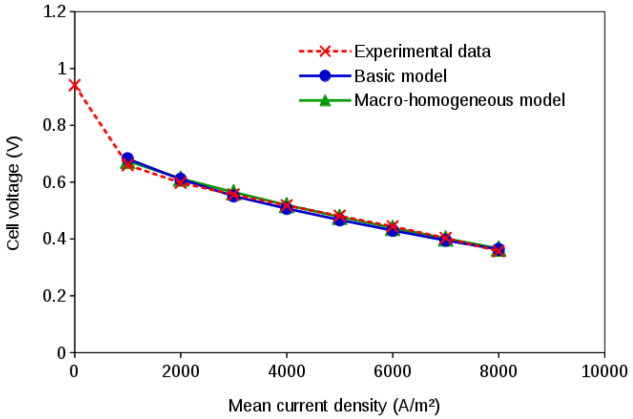

Figure 3.35: Polarisation curve: comparison of numerical results of the basic model (blue), the macro-homogeneous model (green) and experimental data with the serpentine flow field (red).

Equation 2.30:

$$\eta_0 = \underbrace{b \cdot \text{arcsinh}(\frac{(i/j_\sigma)^2}{2(c_{O_2}/c_{ref})(1-\exp(-i/(2j_*)))})}_{\text{activation + proton transfer loss}} + \underbrace{\frac{\sigma_t b^2}{4FD_{CL}c_{O_2}}(\frac{i}{j_*} - ln(1+\frac{i^2}{{j_*}^2\beta^2}))}_{\text{oxygen transfer loss}} \tag{3.8}$$

Besides the ohmic loss, the overpotential can be spilt into two parts: 1) the combination of the activation overpotential and the proton transfer loss; 2) the oxygen transfer loss. The values of these two losses are plotted in Figure 3.36 and compared with the activation overpotential calculated in the basic model. It is worth to note that, the ohmic overpotentials of the both case are not shown in Figure 3.36.

As shown, the solid blue line indicates the activation overpotential of the basic model; the solid green line indicates the sum of the activation overpotential and the proton transfer loss in the catalyst layer of the macro-homogeneous model; the green dash line indicates the oxygen transfer loss of the macro-homogeneous model; the red solid line indicates the sum of the values of the two green lines. All curves increase with the increasing of the mean current density. The values of red line equal approximately the values of the blue line: the biggest difference (0.02 V) occurs in 1000 A/m^2.

The macro-homogeneous model can estimate the proportion of the oxygen transfer loss in the total overpotential. As shown in Figure 3.37, with the increasing of the mean current density, the proportion of the oxygen transfer loss in the total overpotential increases from $2.1\,\%$ to $11.4\,\%$.

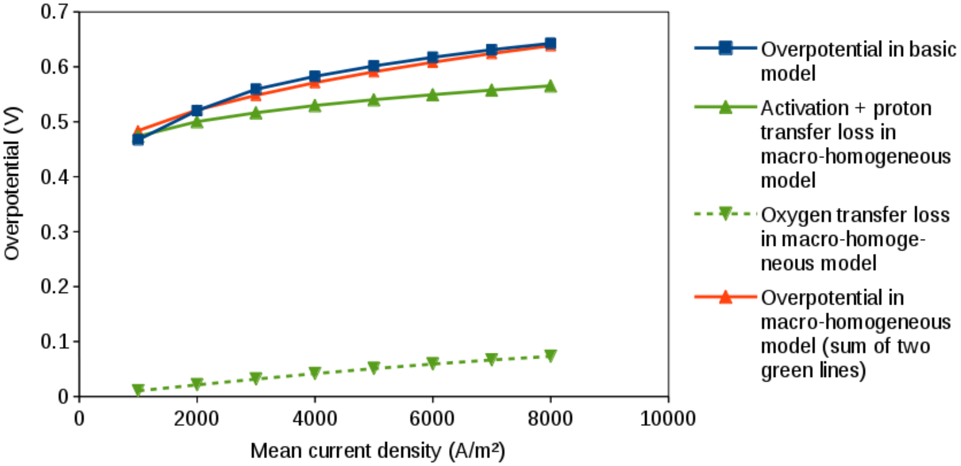

Figure 3.36: Overpotential: comparison of numerical results of the basic model (blue) and the macro-homogeneous model (green). The ohmic overpotentials of the both case are not shown.

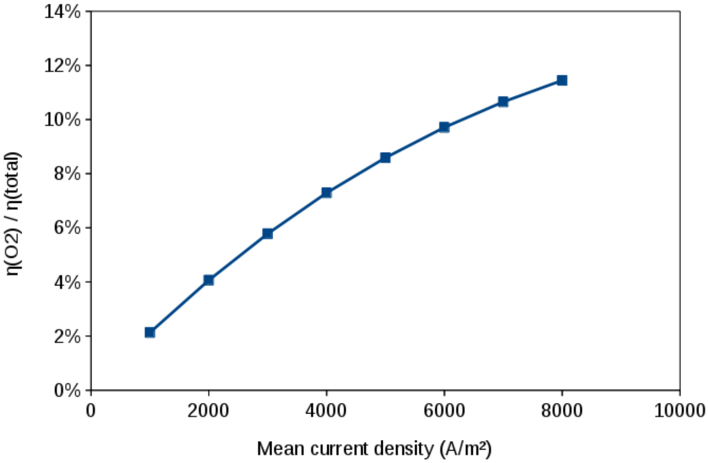

Figure 3.37: The proportion of the oxygen transfer loss in the total overpotential as a function of the mean current density.

Local distribution of properties

In this paragraph, the local distributions of the physical properties, such as mole fraction of species, current density, velocity and temperature of the basic model and the macro-homogeneous model are presented. Both of these two simulations were under a mean current density of 4000 Am^{-2}.

The mass balances of the species for the anode side and the cathode side of the two models are checked according to Eq. (3.1) to Eq. (3.3).

For the basic model, the relative mass transfer errors of the species are: δ_{O_2} = 0.11 %, δ_{H_2} = 0.01 %, δ_{H_2O} = 0.14 %, δ_{N_2} = 0.01 %. For macro-homogeneous model, the relative mass transfer errors of the species are: δ_{O_2} = 0.11 %, δ_{H_2} = 0.01 %, δ_{H_2O} = 0.10 %, δ_{N_2} = -0.01 %.

Figure 3.38 compares the distributions of the mole fraction of oxygen (X_{O_2}) on the electrolyte-GDE interface, which were determined by the basic model (left) and the macro-homogeneous model (right). The distributions of X_{O_2} in these two figures have similar trends:

- The maximum value of X_{O_2} occurs in the inlet region, and decreases along the serpentine flow direction.
- X_{O_2} under the channels is higher than which under the ribs.

However, small differences are still observed: at the inlet, X_{O_2} of the macro-homogeneous model (19.63 %) is slightly higher than the basic model (18.99 %); at the outlet, the mean value of X_{O_2} of the macro-homogeneous model (8.23 %) is slightly lower than the basic model (8.46 %). The mean vlaue of X_{O_2} of the basic model on the electrolyte-GDE interface is 12.43 %; for the macro-homogeneous model, this value is 12.74 %.

Interestingly, although the numerical results of the distributions of X_{O_2} of these two models were similar, the current distribution of these two models still showed a significant difference. As shown in Figure 3.39, the current densities of both models have the serpentine shape. However, the current density calculated by the basic model varies from 2622 Am^{-2} to 6081 Am^{-2}, while the current density calculated by the macro-homogeneous model varies from 3681 Am^{-2} to 4340 Am^{-2}. The percentage based histogram of current density distributions of these two models is shown in Figure 3.40, with 100×100 sampling points on the electrolyte-GDE interface. One can see that the current density of the macro-homogeneous model varies in a much smaller range than the basic model. Most of the current densities (80%) of the macro-homogeneous model are distributed in the range of 3900 Am^{-2} to 4100 Am^{-2}, that distribution is more homogeneous than the basic model. The reason is that, in this thesis, X_{O_2} on the electrolyte-GDE interface is the mole fraction of oxygen when the oxygen just passes through the GDL. In the basic model, it is assumed that the transfer of oxygen in the CL is very fast and there is no additional overpotential due to the oxygen transfer in the CL. The macro- homogeneous model assumes a limited transfer of oxygen in the CL, that brings the additional local overpotential (Eq. (2.30)). Compared to the Tafel equation (2.17), the calculation of the overpotential in Eq. (2.30) is more complex but has less sensitivity of the local oxygen mole fraction. Therefore, the impact of the oxygen mole fraction distribution on current distribution is smaller in the macro-homogeneous model than the basic model.

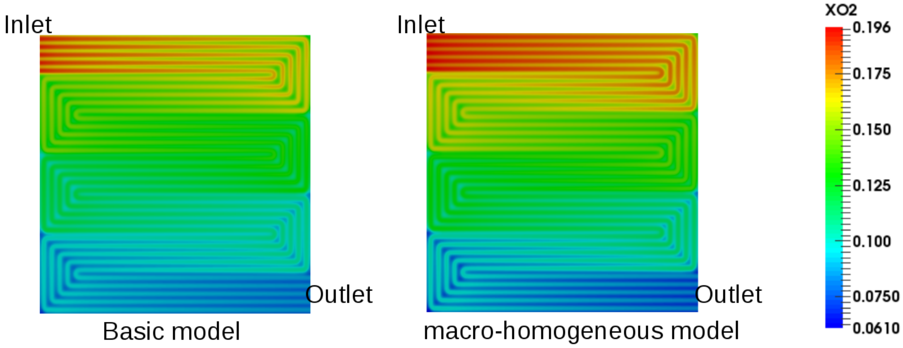

Figure 3.38: Comparison of mole fraction distribution of oxygen calculated by the basic model and the macro-homogeneous model at 4000 Am^{-2} mean current densities.

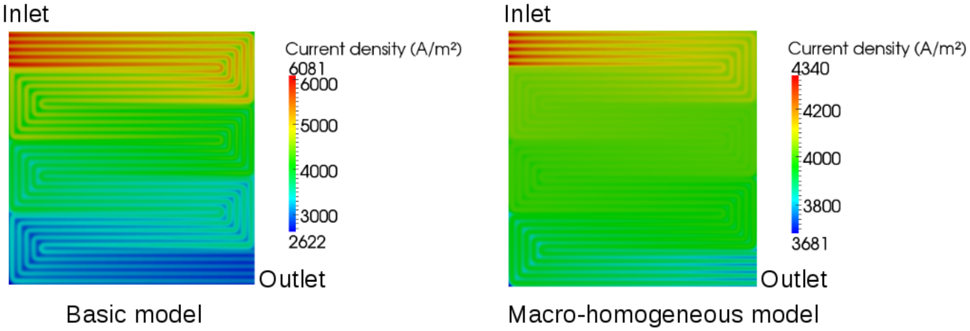

Figure 3.39: Comparison of current density distribution calculated by the basic model and the macro-homogeneous model at 4000 Am^{-2} mean current densities.

The numerical results show the similar distributions of the velocity and temperature for these

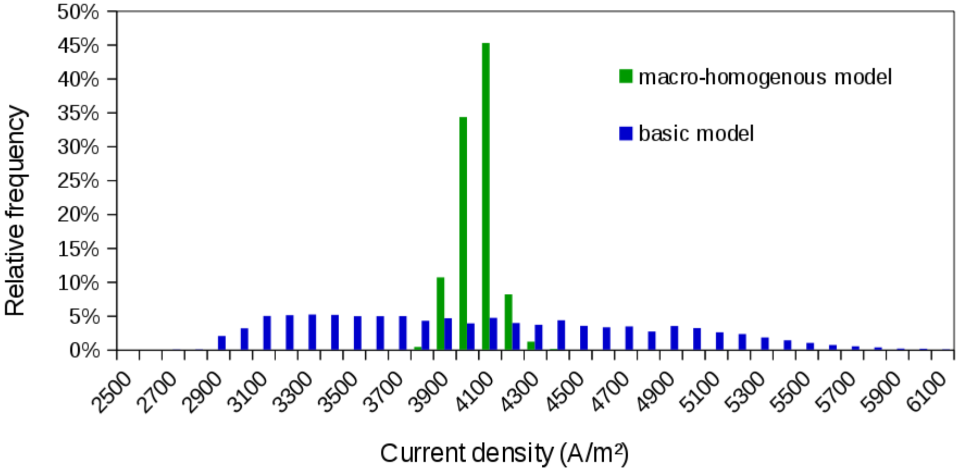

Figure 3.40: Percentage based histogram of current density distribution of the basic model (blue) and the macro-homogeneous model (green) at 4000 $\mathrm{Am^{-2}}$ mean current densities.

two models. Therefore, only the result of the basic model is taken to present the velocity and temperature distribution of the single cell with serpentine flow field. Since the 3-D fields of velocity and temperature are not straightforward to show, two cross-sectional planes are used to display the local information. As shown in Figure 3.41, plane A is in the middle of the cell, and plane B is in the middle of the channel and perpendicular to the MEA.

Figure 3.42 shows the magnitude of the velocity under an operating point 4000 $\mathrm{Am^{-2}}$ of plane A. Since the whole cross-section is too narrow to present, only the first five channels near the outlet are shown. Figure 3.43 shows the magnitude of the velocity of plane B. Since the channel is too long, only the first 25 mm are shown. Both figures suggest that the largest velocity occurs in the middle of the channel and decreases towards the wall.

Figure 3.44 shows the temperature profile of plane A and Figure 3.45 shows the temperature profile of plane B. The perfect cooling is assumed, which means the fixed value boundaries (433 K) are applied on the outer walls. As shown, the temperature on both planes varies from 433K to 435K. This little difference shows that if the fixed temperature can be hold on the outer wall of the cell, the internal field of an HT-PEFC will be in the quasi-isothermal state. The heat source is at the electrolyte-GDE interface due to the exothermic reaction and ohmic heating. Figure 3.44 also shows that the temperature under the gas channel is higher than under the

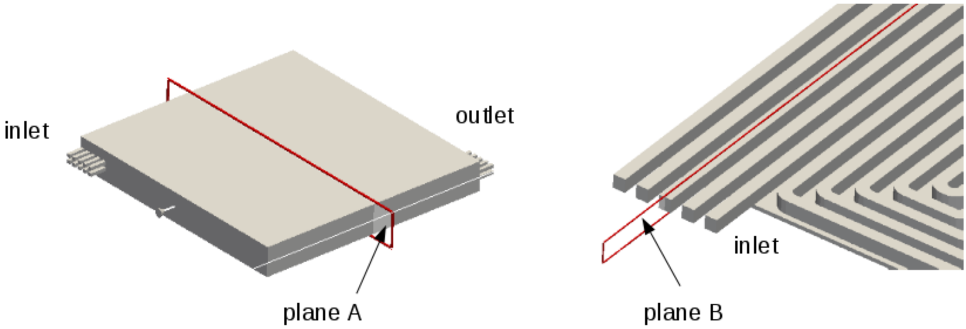

Figure 3.41: Cross-sectional planes for presenting the velocity and temperature distribution. Left: plane A, which is in the middle of the cell; Right: plane B, which is in the middle of the channel and perpendicular to the MEA.

rib.

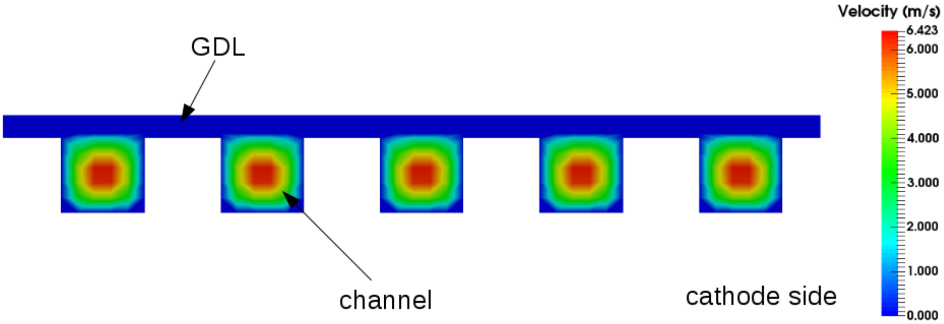

Figure 3.42: Velocity profile on the cross-sectional plane A (only five channels are showed).

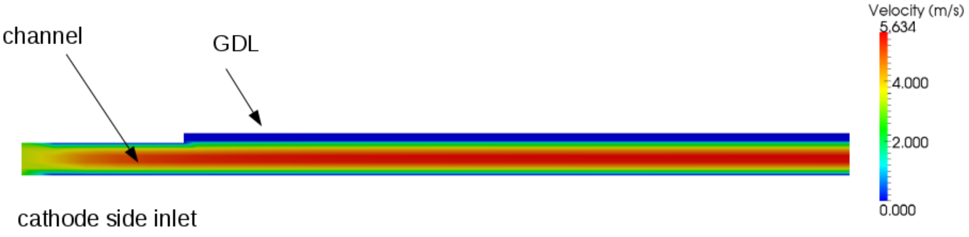

Figure 3.43: Velocity profile on the cross-sectional plane B (only the first 25 mm are showed).

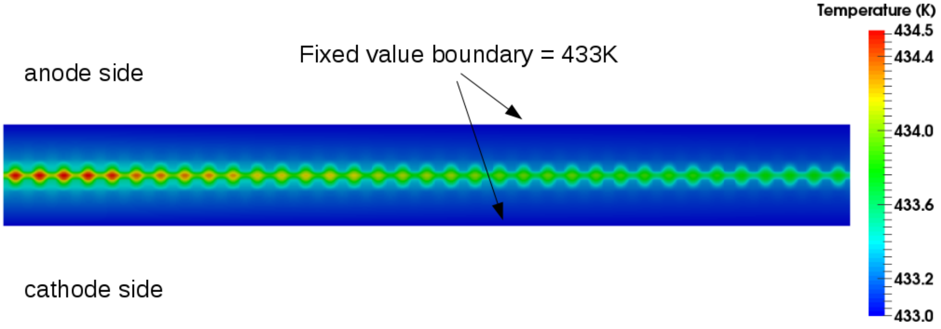

Figure 3.44: Temperature profile on the cross-sectional plane A. The left part is the inlet side and the right part is the outlet side.

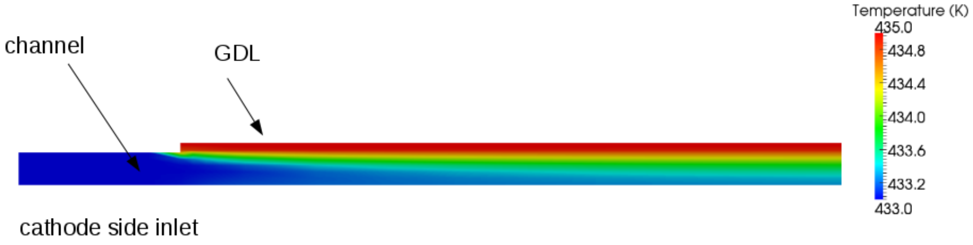

Figure 3.45: Temperature profile on the cross-sectional plane B (only the first 25 mm are showed).

Summary

The numerical results with the single cell with serpentine flow field of the basic model and the macro-homogeneous model were presented in this section. The electrochemical parameters of these models are fitted from the experimental data. Compared to the numerical results of the basic model, the macro-homogeneous model considered the proton transfer loss and the oxygen transfer loss in the catalyst layer. This model requires three more fitting parameters, which are hard to measure in the practice. However, this model provides the possibility to include the effects of the catalyst layer properties on the cell performance.

The local distributions of the oxygen mole fraction, current density, velocity, and temperature were also showed. By macro-homogeneous model, the distribution of the oxygen mole fraction are similar to the basic model, and the distribution of the current density is more homogenous than the basic model.

3.3.2 Water transfer model (model III)

As introduced in Section 2.4, the water-crossover is a significant issue on the fuel cell performance. In this work, two water transfer models are implemented in the HT-PEFC solver and validated with the experiment: the basic water transfer model (model III-a) and the modified water transfer model (model III-b). The simulations were under the operating conditions which were presented in Table 3.2. The experimental data was taken from [116]. In that work, an HT-PEFC with a commercial MEA was operated under the same conditions as Table 3.2. The water was condensed by condensers and then collected using glass bottles.

The active area in the simulation was fixed as 52.62 cm^2. This value was directly calculated according to the sketch of the flow field design. However, in the experiment, the sealing covers a part of the reaction surface. The active area is therefore smaller. This area of the experimental cell is around 45 cm^2. For making an appropriate comparison, in this work, all the water fluxes from the experiment were modified by a factor $52.62/45$, i.e 1.17. The local distributions of properties of the two models are also presented in the following subsections.

Validation of the model III-a

The governing equations and numerical algorithms of the model III-a are already showed in Section 2.4. The sensitive parameter to the overall performance is the effective diffusivity of water $D_{H_2O}^{eff}$. In the literature, this value was assumed to be 2.7$\times$10^{-7} m^2 s^{-1} in [116] and 1 $\times$10^{-7} m^2 s^{-1} in [120]. In this work, $D_{H_2O}^{eff}$ was estimated as 2.4$\times$10^{-7} m^2 s^{-1}. This value is fitted from the measured water flux of an in-house experiment, the experimental data are listed in Appendix 6.2. Three mean current densities were taken to simulate the water transfer and calculate the quantities of water at the anode and cathode side: 2000 Am^{-2}, 4000 Am^{-2} and 6000 Am^{-2}.

Figure 3.46 compares the numerical results and the experiment results. The flux of water at the outlets was plotted as a function of mean current densities. As shown, the solid black lines indicate the numerical outcomes of the anode and cathode side, the red points indicate experiment results of the anode and cathode side. At the anode, the numerical results increase linearly with the increasing of the mean current density and fits the experiment data. The largest deviation between the simulation and the experiment is 0.58 g/h, which occurs at 6000 Am^{-2}. At the cathode, the numerical results also increase linearly with the increasing of the mean current density. It shows the same trends as the experiment. However, the deviations between the simulation and the experiment at cathode side are higher than anode side. At the current densities of 2000 Am^{-2}, 4000 Am^{-2} and 6000 Am^{-2}, the deviations of the water flux of the cathode side are 0.25 g/h, 0.71 g/h and 1.26 g/h. The deviations are 9.3 %, 13.0 % and 15.3 % of the experimental data.

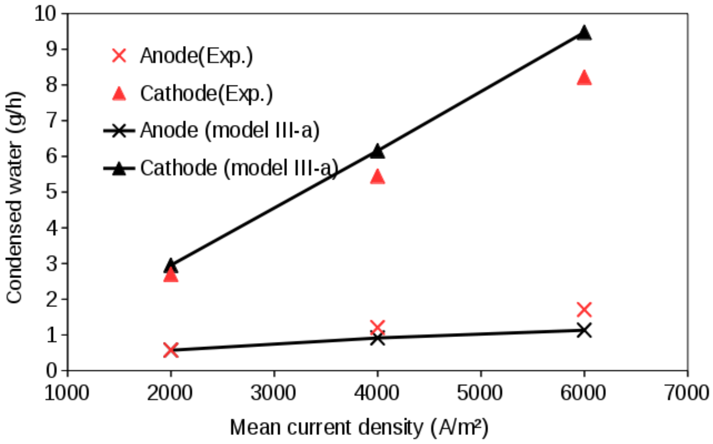

Figure 3.46: Generated water at the cathode side and anode side: comparison of the CFD simulation and the experiment.

Table 3.16 presents the comparison of the calculated total water flux and the total water quantity collected by experiment. The calculated total mass flux of water is proportional to the mean current density:

$$\phi_{total} = AM_{H_2O}\frac{i}{nF} \tag{3.9}$$

where

ϕ_{total} = total mass flux of the generated water (kg s^{-1})

A = active area (m^2)

One can see that there is 6 %- 7 % deviation between the calculation and the experiment. It can be explained as the experimental error.

The other critical result in the model III-a is the crossover rate γ (Equation 2.38). It indicates that how many percents of the generated water will cross the membrane. This parameter was first introduced in the modelling works of PEFC from Bernardi et al. [134] and Springer et al. [42] to characterise the crossover effect of water.

The comparison of the simulation and the experiment on γ is showed in Figure 3.47. The solid black line indicates the mean value of γ. One can observe that by the experiment, the crossover rate is nearly constant ($\approx$ 18 %). By the simulation, the crossover rate decreases with

Table 3.16: Total mass flux of the generated water: comparison of the CFD simulation and the experiment.

	Total flux of water (g/h)		
I (Am^{-2})	Numerical	Experiment	Deviation
2000	3.52	3.27	7.08 %
4000	7.07	6.65	5.93 %
6000	10.61	9.93	6.41 %

the increasing of the mean current density. The reason for this deviation is that the effective diffusivity of water $D_{H_2O}^{eff}$ was a fixed number in the simulation. However, in practice, this might vary with the mean current density, because the density of the water-acid solution changes with the mean current density.

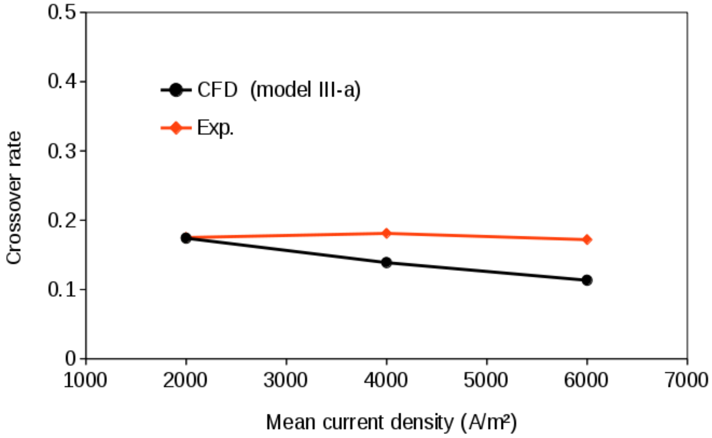

Figure 3.47: Cross over rate of the generated water: comparison of the model III-a and the experiment.

Local distribution of properties of the model III-a

The local distributions of the water vapour at the anode and the cathode side are calculated using the model III-a. The mean current density was 4000 Am^{-2}.

The mass balances of the species for the anode side and the cathode side for model III-a are checked according to Eq. (3.1) to Eq. (3.3). The relative mass transfer errors of the species are: δ_{O_2} = 1.39 %, δ_{H_2} = 0.17 %, δ_{H_2O} = 0.09 %, δ_{N_2} = 0.002 %.

The mole fractions of water vapour (X_{H_2O}) at the electrolyte-GDE interfaces are presented in Figure 3.48.

At the anode side, X_{H_2O} varies from 0 to 11.5 %, at the cathode side, X_{H_2O} varies from 0 to 20 %. The distributions of X_{H_2O} give the following trends:

- X_{H_2O} at the cathode side is higher than anode side. This result is as expected because the water is first produced at the cathode side. For the ideal gas, the mole fraction is proportional to the partial pressure. Accordingly, the partial pressure of the water vapour at the cathode side is higher than anode side. This deviation of the water vapour partial pressure between anode and cathode is considered as the driving force of the water crossover in this water transfer model.

- At both sides, the maximum value of X_{H_2O} occurs in the outlet region. The mole fraction increases along the flow direction. This result is expected because the water is generated continuously along the flow direction.

- At both sides, X_{H_2O} under the channels is lower than that under the ribs. Because the reactants depletion is strongest under the ribs, which would mean that X_{H_2O} under the ribs increases.

- On the picture of the X_{H_2O} distribution at the anode side, the dividing line between the channel region and the rib region is not clear. This result is as expected. Because the gases on the anode side are hydrogen and water, the mean binary diffusivity of these two gases is 1.18×10^{-4} m^2s^{-1}. It is an order of magnitude higher than the binary diffusivities at the cathode side. A high diffusivity means the gas diffuses easier from high concentration to low concentration. Consequently, the variation between X_{H_2O} under the channel and the rib is small.

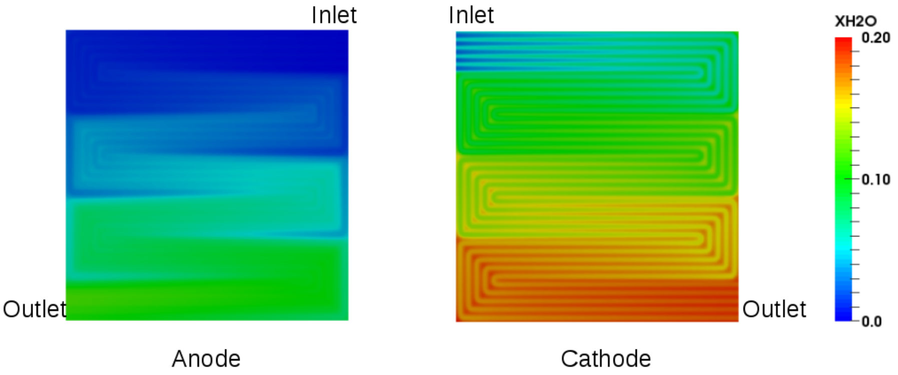

Figure 3.48: Mass fraction of water vapour at the electrolyte-GDE interface: comparison of anode side and the cathode side (the model III-a).

Validation of the model III-b

In the model III-b, the absorption-evaporation processes of water are considered. The governing equations and numerical algorithms are already showed in Section 2.4. An empirical Equation 2.42 was used to correspond the mass fraction of water in the electrolyte and the partial pressure of the water vapour in the GDL.

The sensitive parameters of this model is the Effective mass transfer coefficient $k^{eff}_{H_2O,l}$ and the reference current density $i_{ref,w}$. In this work, $k^{eff}_{H_2O,l}$ was estimated as 2×10^{-6} kg m^{-1} s^{-1} and $i_{ref,w}$ is assumed to be 1×10^{4} A m^{2}. These values are fitted from the measured water flux of an in-house experiment, the experimental data are listed in Appendix 6.2.

Similar to the model III-a, three mean current densities were taken to estimate the quantities of water at the anode and cathode side: 2000 Am^{-2}, 4000 Am^{-2} and 6000 Am^{-2}.

Figure 3.49 compares the numerical results of the model III-a, the numerical results of the model III-b and the experiment results. The flux of water at the outlets was plotted as a function of mean current densities.

As shown, the solid black lines indicate the numerical results of the model III-a, the solid blue lines indicate the numerical results of the model III-b and the red points indicate experiment results. By both models, it is observed that, not only the total water flux increase linear with the increasing of the mean current density. This linear relationship also occurs separately at the anode side and the cathode side (Figure 3.49). The models suggest that the flux of the water crossover of an HT-PEFC is proportional to the mean current density, this effect is modelled in the previous research [116].

It can also be observed that the agreement between the model III-b and experiment is better than the agreement between the model III-a and experiment. At both anode and cathode, the numerical results of the model III-b increase linearly with the increasing of the mean current density. At the anode, the deviation between the simulation and the experiment ranges between 0.04 g/h and 0.15 g/h; at the cathode, the deviation between the simulation and the experiment ranges between 0.21 g/h and 0.83 g/h.

However, for the model III-b, there is still 6 %-7 % deviation of the total water flux between the simulation and the experiment, because of the experimental error.

Figure 3.50 compares the water crossover rate of the model III-a, the model III-b and experiment. It can be seen that the agreement between the model III-b and experiment is also better than the agreement between the model III-a and experiment. This result is as expected because the model III-b introduces an additional empirical equation (Equation 2.41) to correct the density change of the water-acid solution with the change of mean current density.

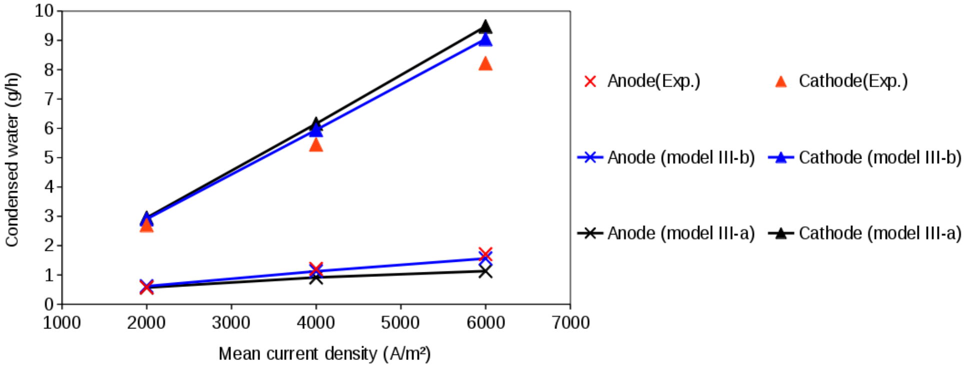

Figure 3.49: Generated water at the cathode side and anode side: comparison of the model III-a, model III-b and the experiment.

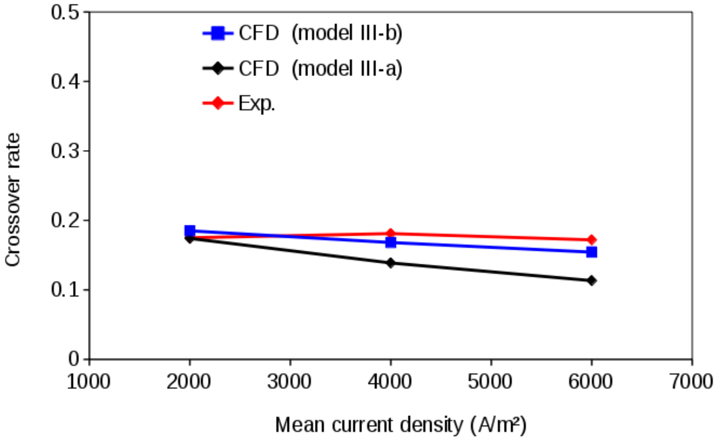

Figure 3.50: Cross over rate of the generated water: comparison of the model III-a, model III-b and the experiment.

Local distribution of properties of the model III-b

The mass balances of the species for the anode side and the cathode side for model III-b are checked according to Eq. (3.1) to Eq. (3.3). The mean current density was 4000 Am^{-2}. The relative mass transfer errors of the species are: δ_{O_2} = 1.70 %, δ_{H_2} = 0.21 %, δ_{H_2O} = 0.07 %, δ_{N_2} = 0.004 %.

The mole fractions of water vapour (X$_{H_2O}$) at the electrolyte-GDE interface determined by the model III-b are displayed in Figure 3.51. One can see that Figure 3.51 is near-identical to Figure 3.48. The only difference is that X$_{H_2O}$ of the model III-b at the anode outlet is slightly higher than that of the model III-a. The difference is around 2.1 %.

Different from the model III-a, the mass fraction (wt %) of the phosphoric acid can be solved by using the model III-b. Figure 3.52 shows the mass fraction of the phosphoric acid (Y$_{H_3PO_4}$) on the anode and the cathode sides of the electrolyte. One can see that Y$_{H_3PO_4}$ varies in the whole electrolyte region. The concentration of the phosphoric acid of the anode side is higher than that of the cathode side. In other words, the concentration of liquid water on the anode side is lower than that of the cathode side. This concentration gradient of liquid water is assumed to be the driven force of the water crossover. In the electrolyte, the numerical calculation indicates that Y$_{H_3PO_4}$ is between 93.9 % and 95.3 %. This is in agreement with the measurement using synchrotron-based X-ray tomographic microscopy of an HT-PEFC: at 160 ℃, Y$_{H_3PO_4}$ is reported as 96.5 ± 1.5 wt % [135].

The calculated value of $Y_{H_3PO_4}$ from CFD is higher than the original state of the membrane. By the in-house experiment, $Y_{H_3PO_4}$ in the membrane was 85 % when it just assembled from the lab. The CFD simulation determines a quasi dry-out state of the membrane. It will lead to a decreasing of the cell performance. The proton conductivity of the phosphoric acid is a function of phosphoric acid composition. By the typical operating temperature of an HT-PEFC (160 ℃), the highest proton conductivity was reported in the range of 62 - 65 wt % of P_2O_5 [136, p.118], which are 85 % - 90 % of $Y_{H_3PO_4}$. When $Y_{H_3PO_4}$ is bigger than 90 %, the proton conductivity decreases rapidly with the increasing of $Y_{H_3PO_4}$.

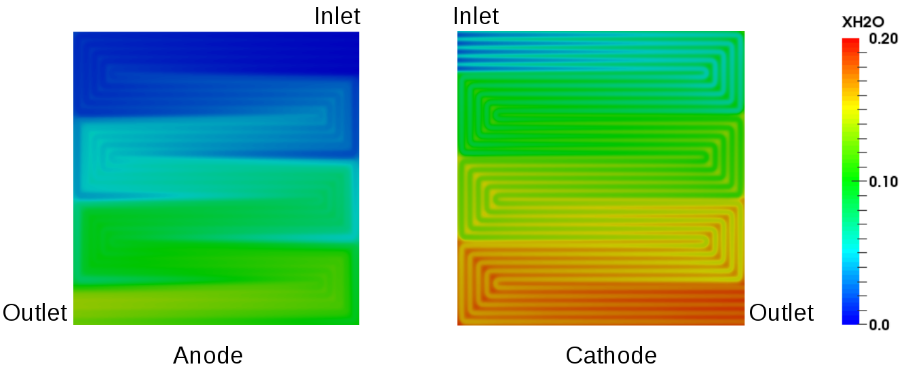

Figure 3.51: Mass fraction of water vapour at the electrolyte-GDE interface: comparison of anode side and the cathode side (the model III-b).

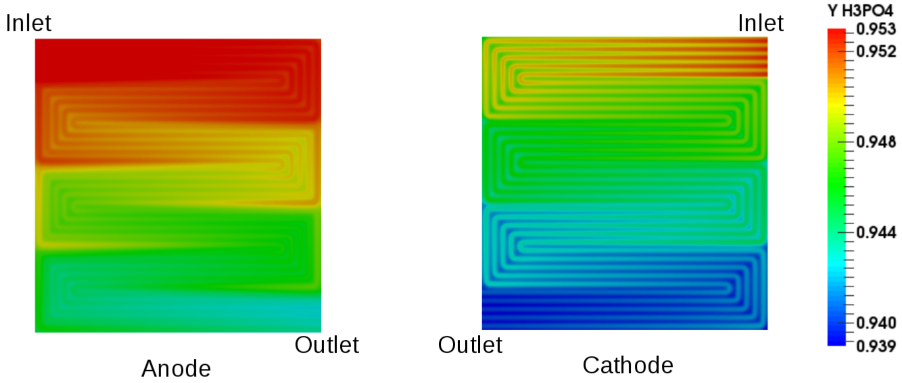

Figure 3.52: Mass fraction of phosphoric acid at the electrolyte-GDE interface: comparison of anode side and the cathode side (the model III-b).

Summary

The numerical results of the water transfer model were presented in this section. Two versions of the water transfer model (the model III-a and the model III-b) were validated with the experiment data.

In the model III-a, the absorption-evaporation and diffusion are treated as one effective transfer process. The numerical result of the flux of water at the outlets fitted the experiment data well. The deviation of the total water flux between the simulation and the experiment is 6 %-7 %, which is probably caused by the incomplete condensation of water vapour by experiment. The local distributions of water vapour at the electrolyte-GDE interfaces were also showed.

The model III-b solved the absorption-evaporation and the diffusion separately. The numerical result of the water flux at the outlets and the water crossover rate of this model fitted the experiment data better than that of the model III-a. However, the deviation of the total water flux between the simulation and the experiment is still the same. Additionally, this model can determinate the concentration of the phosphoric acid in the membrane. In the later work, the model for solving the local distribution of the proton conductivity of the membrane can be integrated into this model.

4 Discussion

The objective of this thesis is the 3D-modelling of HT-PEFC on the cell level for improving the understanding of the physical phenomena in the cell. In the scope of the chemical engineering, the HT-PEFC is usually considered as a membrane reactor, which can continuously produce electricity from the chemical energy of the fuel. This membrane reactor mainly consists of bipolar plates (BPPs), Gas diffusion layers (GDLs), catalyst layers (CLs) and a phosphoric acid doped membrane. In this thesis, conservation equations are created and solved using the CFD technology, to calculate the physical variables in these components or the spaces between these components (gas channels or pores). Compare to the analytical model, the 3-D CFD model takes the 3-D effect into account and offers detailed local information inside the cell. In this thesis, the following phenomena are solved: the mass transfer, the momentum transfer and the species transfer in the gas channels and GDLs; the heat transfer in the flow and the BPPs; the electrochemical reaction in the electrolyte-GDE interface; and the water transfer in the membrane.

The modelling of the mass transfer of the gas mixture employs the continuity equation. The modelling of the momentum transfer in the gas channels employs the Navier-Stokes equations. For the momentum transfer in the GDLs, the Navier-Stokes equations are modified by adding a Darcy term. This method offers a benefit: there is no need to separate the mesh of gas channels and the GDLs, since the momentum transfer of the both gas channels and GDLs are solved in one mesh. That brings the convenience of mesh creating and programming. However, Beale [137] has reported that this method is not strictly correct for highly permeable porous media. The calculations of the Reynolds number indicates that the flow in the HT-PEFC with the typical operating condition is laminar flow, it does not require to combine the turbulence model with the Navier-Stokes equations. The calculations of the Péclet number indicates that, in the gas channels, the convection dominates the mass transfer; in the GDLs, the convection is neglectable compared to the diffusion. Through the checking of the mass balances of the species for the anode side and the cathode side, it is observed that the meshes with offsets on both inlet and outlet side provide the better mass balances.

The modelling of the species transfer of the reactants employs the species conservation-equations. A key issue is the solving of the mass based diffusion flux of the species. This thesis provides two ways to do that: using Fick's law or Maxwell-Stefan formulation. From a classical point of view of the multicomponent mass transfer, the Fick's law is incomplete because it neglects the interaction between the species, in the case of three of more species in the mixture. On the other hand, the Maxwell-Stefan formulation considers that interaction between the species and may get a more precise calculation of the species distribution [124, p.34-52]. In the modelling works of HT-PEFC, different authors took the Maxwell-Stefan formulation into account [84, 90, 109]. However, this study suggests that at the typical operating point of HT-PEFC, the interaction between the gas species is small, both Fick's law (modified by Wilke's formulation) and Maxwell-Stefan formulation can be used to calculate the diffusion flux. With the both approaches, the local distributions of the species in the channel, in the GDL and on the electrolyte-GDE interface are solved. The channel-rib effect of the species distribution are observed: the mole fraction of oxygen under the channel is larger than which under the ribs. In practice, it may lead a large concentration overpotential because of the shortage of oxygen under the ribs. In the simulations, the local depletion of the reactant will crash the code in the extreme case. Additionally, the simulation shows that the mole fraction of oxygen in the channel along the flow direction presents a similar profile as the analytical solution in [129]. The deviation between the numerical and analytical results may be due to the diffusion effect.

The modelling of the heat transfer uses the energy conservation-equation. The simulations shows that the electrochemical reaction will heat up the reaction zone around less than 2K, which means that the cell is in a quasi-isothermal state in the operating. However, the simulations in this thesis assume a fixed boundary condition of temperature on the outer walls of the cell. In practice, this fixed boundary condition is not appropriate. The cell is heated up by the heating element and keep the temperature by using the cooling medium [38].

For the modelling of the electrochemistry, the catalyst layer is assumed to be an infinitely thin layer (2- D interface) in this thesis. It provides two ways to calculate the kinetic: using Tafel equation or the macro- homogeneous approach. Both electrochemical model are validated with the experimental data. However, each model requires the sensitive electrochemical parameters; these parameters are fitting values. They change by different cells, because they depend on the situation inside the catalyst layer: the acid loading, the Pt loading, the porosity, the local swelling, the operating condition, et al. In this work, these values are fitted from the in-house experiment of a single serpentine cell with the active area of 50 cm^2. In the Tafel approach, the overpotential of the CL is the activation overpotential, which is represented by the Tafel equation. In the macro- homogeneous approach, the effects of the CL on cell performance is taken into account. The idea of the macro- homogeneous model comes from the works [49, 50, 60]. The implementation of the macro- homogeneous model into CFD is not reported in the literature so far. The macro- homogeneous model allows to separate the overpotential of the CL into two parts: 1) the combination of the activation overpotential and the proton transfer loss; 2) the oxygen transfer loss in the CL. The numerical study suggests that the second part is below $11.4\,\%$ of the overall overpotential. That means the oxygen transfer loss in the CL does not dominate the potential loss in the CL. In the previous modelling works of HT-PEFC, for instance [78, 81, 90], the oxygen transfer loss in the CL is usually neglected.

The modelling of water transfer focuses on representing the water transfer phenomena in the phosphoric acid-doped PBI membrane. Two versions of the water transfer model are made in this thesis: one integrates the absorption-evaporation processes and diffusion of water in one effective transfer process while the other one calculates these two processes separately. Both approaches require the effective transfer coefficient of water in the acid-doped membrane, which is the fitting parameter. Theoretically, the absorption-evaporation (phase change) processes can be modelled by the Hertz-Knudsen equation. However, the partial pressure of the water vapour close to the electrolyte-GDE interface is hard to measure in the in-situ case. Therefore, the empirical equations are used in this thesis, to model this process on the electrolyte-GDE interface. In the previous modelling works [84, 138], other empirical equations are also used. The simulations suggest that the mass fraction of the phosphoric acid is between $93.9\,\%$ and $95.3\,\%$ at the in-situ situation. This case decreases the cell performance since the concentration of phosphoric acid in the membrane is not in the optimum situation. The humidification might be needed at the anode or cathode side.

5 Conclusion

In this thesis, the CFD models of HT-PEFC on the cell level were developed and implemented using an open source software OpenFOAM. With the developed solvers, it is possible to calculate the mass transfer, momentum transfer, species transfer and heat transfer in the whole region of the HT-PEFC. The electrochemical reaction was also implemented as the source term at the electrolyte-GDE interface. Two geometries were used in this thesis to construct the meshes. The first one is a single-channel pair with an active area of 0.2 cm^2 and the second one is a single cell with an active area of 50 cm^2. The first one is used to understand the basic performance of the mass transfer of HT-PEFC. The latter one corresponds to an in-house prepared HT-PEFC cell to validate the numerical results with the experimental data. Both of these two meshes have the composite structure.

Four mathematical models were applied: the basic model, the macro-homogeneous model, the water transfer model and the multicomponent diffusion model. The basic model provides the description of the basic mass transfer phenomena and electrochemistry in the cell. The later three correspond to other relevant mass transfer processes in the HT-PEFC: the oxygen and proton transfer in the catalyst layer, the water crossover in the electrolyte and the multicomponent diffusion in the gas channel and GDL.

The performance of the basic model with the single channel pair was presented in Section 3.2.1. The local distributions of mole fraction of species, velocity, temperature, and current density were shown. Two operating points were taken to compare the performance with low mean current density (2000 Am^{-2}) and high mean current density (8000 Am^{-2}). The performance of the basic model with the single cell geometry with serpentine flow field was presented in Section 3.3.1. The basic model was validated by comparing the numerical results and the experimental data on the polarisation curve. The local distributions of properties in the serpentine flow fields were also presented. Additionally, the compression effect of the GDL was examined using the basic model in Section 3.2.2. Four single channel pair meshes were created with the different engineering strain of the GDL: $0\,\%$, $10\,\%$, $18\,\%$ and $29\,\%$. The effects of the engineering strain of the distribution of oxygen and current density were discussed.

By the macro-homogeneous model, the analytical formulations was implemented in code, to describe the transport losses of oxygen and protons in the GDL. The performance of this model with single cell geometry was presented in Section 3.3.1. Similar to the basic model, it was observed that an agreement between numerical and experimental data on the polarisation curve. The local distributions of mole fraction of oxygen and current density were shown and compared with the basic model.

By the water transfer model, the absorption-evaporation processes and diffusion of water in the membrane are considered. The performance of this model with single cell geometry with serpentine flow field was presented in Section 3.3.2. The calculated water flux of anode side and cathode side were validated with the experimental data. The local distributions of mass fraction of the phosphoric acid were shown.

By the multicomponent diffusion model, the Maxwell-Stefan equations were transformed to a matrix form and then implemented in the solver. The performance of this model with single cell geometry with serpentine flow field was presented in Section 3.2.3.

Overall, this thesis focused on the modelling of the relevant mass transfer processes of an HT-PEFC. All the models were based on the modular programming techniques, and they can cooperate easily with each other and be loaded on demand in the praxis. In this thesis, several relevant results are observed:

- In the channel, the numerical results of the mole fraction of oxygen show the similar trends with the analytical result; on the electrolyte-GDE interface, the channel-rib effect of the current density and the mole fraction of oxygen are observed.
- The compression of GDL brings the limited transport of the oxygen towards the area under the ribs.
- There is no significant difference for using Fick's law (modified with Wilke's equation) or Maxwell-Stefan equations to solve the diffusion flux of the flow in the HT-PEFC.
- The macro-homogeneous model takes the properties of the catalyst layer into account and suggests the different current density distribution with the basic model.
- The water transfer model suggests that the mass fraction of the phosphoric acid in the membrane is between $93.9\,\%$ and $95.3\,\%$ at the in-situ situation.

6 Appendix

6.1 Experimental data for the parameter fitting of Model I and II

Table 6.1: Operating conditions for the serpentine single cell with the active area of 50 cm^2. The mean current densities were 0 - 8500 Am^{-2}. MEA: CELTEC P1000.

Parameter	Symbol	Value	Unit
Operating temperature	T	433	K
Pressure at anode outlet	p_a	101325	Pa
Pressure at cathode outlet	p_c	101325	Pa
Mass fraction of H_2 at anode inlet	Y_{H_2}	1.00	
Mass fraction of O_2 at cathode inlet	Y_{O_2}	0.23	
Mass fraction of N_2 at cathode inlet	Y_{N_2}	0.77	
Anode stoichiometric ratio	λ_a	2	
Cathode stoichiometric ratio	λ_c	2	

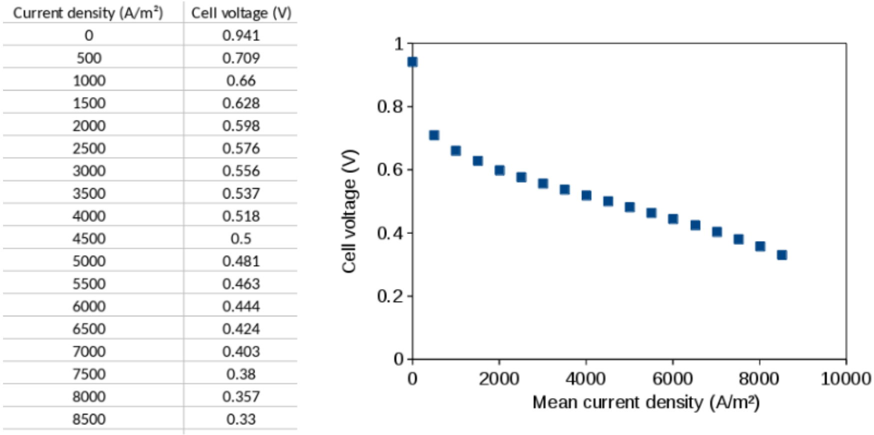

Current density (A/m²)	Cell voltage (V)
0	0.941
500	0.709
1000	0.66
1500	0.628
2000	0.598
2500	0.576
3000	0.556
3500	0.537
4000	0.518
4500	0.5
5000	0.481
5500	0.463
6000	0.444
6500	0.424
7000	0.403
7500	0.38
8000	0.357
8500	0.33

Figure 6.1: The experimental data of the polarization curve for the serpentine single cell with the active area of 50 cm^2. The mean current densities were 0 - 8500 Am^{-2}.

6.2 Experimental data for the parameter fitting of Model III

Table 6.2: Operating conditions for the serpentine single cell with the active area of 50 cm^2. The mean current densities were 2000 Am^{-2}, 4000 Am^{-2} and 6000 Am^{-2}. MEA: CELTEC P1000.

Parameter	Symbol	Value	Unit
Operating temperature	T	433	K
Pressure at anode outlet	p_a	101325	Pa
Pressure at cathode outlet	p_c	101325	Pa
Mass fraction of H_2 at anode inlet	Y_{H_2}	1.00	
Mass fraction of O_2 at cathode inlet	Y_{O_2}	0.23	
Mass fraction of N_2 at cathode inlet	Y_{N_2}	0.77	
Anode stoichiometric ratio	λ_a	2	
Cathode stoichiometric ratio	λ_c	2	

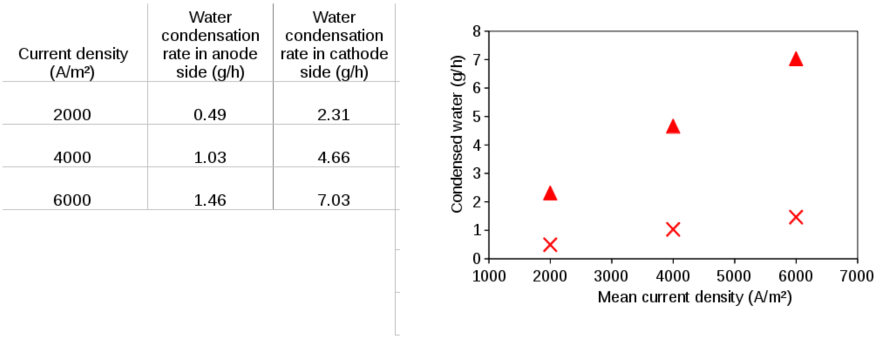

Current density (A/m²)	Water condensation rate in anode side (g/h)	Water condensation rate in cathode side (g/h)
2000	0.49	2.31
4000	1.03	4.66
6000	1.46	7.03

Figure 6.2: The experimental data of the water condensation rate for the serpentine single cell with the active area of 50 cm^2. The mean current densities were 2000 Am^{-2}, 4000 Am^{-2} and 6000 Am^{-2}.

6.3 Derivation of the matrix form of Maxwell-Stefan relationship

6.3.1 Basic equaitons

Before the deriving of the matrix form of Maxwell-Stefan relationship, some basic equations shoule be mentioned first. The following basic equations can be found in Beale [139] and Taylor et al. [126, p.3-5]. The mass density of a mixture is defined by

$$\rho = \sum_{i=1}^{n} \rho_i \tag{6.1}$$

where ρ_i is the mass density of species i. The molar density of a mixture is defined by

$$c = \sum_{i=1}^{n} c_i \tag{6.2}$$

where c_i is the molar density of species i. The mass fraction of species i can be written as

$$Y_i = \frac{\rho_i}{\rho} \tag{6.3}$$

Similarly, the molar fraction of species i can be written as

$$X_i = \frac{c_i}{c} \tag{6.4}$$

The mean molecular mass is defined by

$$M = \sum_{i=1}^{n} (X_i M_i) \tag{6.5}$$

where M_i is the molecular weight of species i. Easy to obtain that

$$M^{-1} = \sum_{i=1}^{n} (Y_i M_i^{-1}) \tag{6.6}$$

and

$$M = \frac{\rho}{c} \tag{6.7}$$

$$M_i = \frac{\rho_i}{c_i} \tag{6.8}$$

The sum of mass fraction and the sum of molar fraction of species i should be equal to unit, therefore

$$\sum_{i=1}^{n} X_i = \sum_{i=1}^{n} Y_i = 1 \tag{6.9}$$

The relationship between Y_i and X_i can be written as

$$Y_i = X_i \frac{M_i}{M} \tag{6.10}$$

We can define u_i as the velocity of species i with respect to a stationary coordinate reference frame. Then the mass flux of species i is

$$n_i = \rho_i u_i \tag{6.11}$$

The mass average velocity of a mixture is defined as

$$v = \sum_{i=1}^{n} Y_i u_i \tag{6.12}$$

The molar average velocity of a mixture is defined as

$$u = \sum_{i=1}^{n} X_i u_i \tag{6.13}$$

The mass diffusion flux with respect to the mass average velocity is

$$j_i = \rho_i (u_i - v) \tag{6.14}$$

with

$$\sum_{i=1}^{n} j_i = 0 \tag{6.15}$$

The molar diffusion flux with respect to the molar average velocity is

$$J_i = c_i (u_i - u) \tag{6.16}$$

with

$$\sum_{i=1}^{n} J_i = 0 \tag{6.17}$$

6.3.2 Molar-based matrix form of Maxwell-Stefan relationship

The momentum equation of species is given by

$$d = \sum_{j=1,j\neq i}^{n} \frac{X_iX_j}{D_{ij}}(u_j - u_i) + \sum_{j=1,j\neq i}^{n} \frac{X_iX_j}{D_{ij}}(\frac{D_j^T}{\rho_j} - \frac{D_i^T}{\rho_i})\nabla lnT, \quad i = 1, 2, ...n \tag{6.18}$$

where d is driving force of the motion of one species. Of right hand side of the above equation, the first term represents momentum caused by the intermolecular friction of species, the secend term represents the thermal diffusion momentum. According to Hirschfelder *et al.* [32], Eqs. (6.18) can be written as

$$\begin{aligned}\underbrace{\nabla X_i}_{\text{chemical potential}} + \underbrace{(X_i - Y_i)\frac{\nabla p}{p}}_{\text{pressure diffusion}} - \underbrace{(b_i - b)\frac{\rho_i}{p}}_{\text{forced diffusion}} =& \\ \underbrace{\sum_{j=1,j\neq i}^{n} \frac{X_iX_j}{D_{ij}}(u_j - u_i)}_{\text{friction}} + \underbrace{\sum_{j=1,j\neq i}^{n} \frac{X_iX_j}{D_{ij}}(\frac{D_j^T}{\rho_j} - \frac{D_i^T}{\rho_i})\nabla lnT}_{\text{thermal diffsion}}, &\quad i = 1, 2, ...n\end{aligned} \tag{6.19}$$

where the driven force is split into three parts: chemical potential, pressure diffusion and forced diffusion. In general case, the pressure diffusion, forced diffusion and thermal diffsion terms are small compared to other terms [127], therefore, Eqs.(6.19) can be simplified as

$$\begin{aligned}\nabla X_i = \sum_{j=1,j\neq i}^{n} \frac{X_iX_j}{D_{ij}}(u_j - u_i),& \\ i = 1, 2, ...n&\end{aligned} \tag{6.20}$$

which is the simplified Maxwell-Stefan relationship.

From Eqs. (6.16) we get

$$u_i = \frac{J_i}{c_i} + u \tag{6.21}$$

Substituting Eqs.(6.4) and (6.21) into Eqs. (6.20), then we find

$$\begin{aligned}\nabla X_i &= \sum_{j=1,j\neq i}^{n} \frac{X_iX_j(\frac{J_j}{c_j} + u - \frac{J_i}{c_i} - u)}{D_{ij}} \\ &= \sum_{j=1,j\neq i}^{n} \frac{X_iX_j(\frac{J_j}{c_j} - \frac{J_i}{c_i})}{D_{ij}} \times \frac{c}{c} \\ &= \sum_{j=1,j\neq i}^{n} \frac{X_iX_j\frac{J_j}{c_j}\frac{c_j}{X_j} - X_iX_j\frac{J_i}{c_i}\frac{c_i}{X_i}}{cD_{ij}}, \quad i = 1, 2, ...n\end{aligned}$$

$$\therefore \nabla X_i = \sum_{j=1, j\neq i}^{n} \frac{X_i J_j - X_j J_i}{c D_{ij}}, \quad i = 1, 2, ...n \tag{6.22}$$

To obtain the matrix form of Maxwell-Stefan relationship, Eqs. (6.22) can be written as

$$c\nabla X_i = -J_i \sum_{j=1, j\neq i}^{n} \frac{X_j}{D_{ij}} + J_j X_i \sum_{j=1, j\neq i}^{n} \frac{1}{D_{ij}}, \quad i = 1, 2, ...n \tag{6.23}$$

Eqs. (6.23) contain n equations, only $n-1$ of them are independent. To solve this equation system, a constrain (6.17) must to be included. Eqs. (6.17) can be expressed as

$$J_n = -J_i - \sum_{j=1, j\neq i}^{n-1} J_j \tag{6.24}$$

Split the last term of the right hand side of Eqs. (6.23) into two terms, we get

$$c\nabla X_i = -J_i \sum_{j=1, j\neq i}^{n} \frac{X_j}{D_{ij}} + J_j X_i \sum_{j=1, j\neq i}^{n-1} \frac{1}{D_{ij}} + J_n X_i \frac{1}{D_{in}}, \quad i = 1, 2, ...n \tag{6.25}$$

Substituting Eqs. (6.24) into Eqs. (6.25), then we obtain

$$c\nabla X_i = -J_i \sum_{j=1, j\neq i}^{n} \frac{X_j}{D_{ij}} + J_j X_i \sum_{j=1, j\neq i}^{n-1} \frac{1}{D_{ij}} + (-J_i - \sum_{j=1, j\neq i}^{n-1} J_j) X_i \frac{1}{D_{in}}, \quad i = 1, 2, ...n-1$$

Finally we get

$$c\nabla X_i = -J_i \underbrace{(\frac{X_i}{D_{in}} + \sum_{j=1, j\neq i}^{n} \frac{X_j}{D_{ij}})}_{\text{diagonal}} - J_j \underbrace{(-X_i \sum_{j=1, j\neq i}^{n-1} (\frac{1}{D_{ij}} - \frac{1}{D_{in}}))}_{\text{off-diagonal}}, \quad i = 1, 2, ...n-1 \tag{6.26}$$

Eqs. (6.26) contain $n-1$ independent equations, they can be written in matrix form as

$$c\nabla \vec{X} = -[B]\vec{J} \tag{6.27}$$

where $[B]$ is a $(n-1) \times (n-1)$ matrix. The elements of this matrix can be written as

$$B_{ii} = \frac{X_i}{D_{in}} + \sum_{j=1, j\neq i}^{n} \frac{X_j}{D_{ij}}, \quad i = 1, 2, ...n-1 \tag{6.28}$$

$$B_{ij(i\neq j)} = -X_i(\frac{1}{D_{ij}} - \frac{1}{D_{in}}), \quad i = 1, 2, ...n-1 \tag{6.29}$$

which is the matrix form from Taylor and Krishna [126, p.40]. The molar-based diffusion flux can be calculated as

$$\vec{J} = -c[B]^{-1}\nabla \vec{X} \tag{6.30}$$

6.3.3 Mass-based matrix form of Maxwell-Stefan relationship with respect of gradient of molar fraction

Here we recall the species transfer equation

$$\nabla\cdot(\rho U Y_i) - \nabla\cdot\vec{j_i} = 0 \tag{6.31}$$

To combine the Maxwell-Stefan diffusion and Eqs. (6.31), Eqs. (6.30) must be converted to mass-based equations. Here we recall Eqs. (6.20)

$$\nabla X_i = \sum_{j=1,j\neq i}^{n} \frac{X_i X_j}{D_{ij}}(u_j - u_i), \qquad i = 1,2,...n$$

From Eqs. (6.14) we get

$$u_i = \frac{j_i}{\rho_i} + v \tag{6.32}$$

Substituting Eqs.(6.4), (6.8) and (6.32) into Eqs. (6.20), then we find

$$\begin{aligned}
\nabla X_i &= \sum_{j=1,j\neq i}^{n} \frac{X_i X_j(\frac{j_j}{\rho_j} + v - \frac{j_i}{\rho_i} - v)}{D_{ij}} \\
&= \sum_{j=1,j\neq i}^{n} \frac{X_i X_j(\frac{j_j}{\rho_j} - \frac{j_i}{\rho_i})}{D_{ij}} \times \frac{c}{c} \\
&= \sum_{j=1,j\neq i}^{n} \frac{X_i X_j \frac{j_j}{\rho_j}\frac{c_j}{X_j} - X_i X_j \frac{j_i}{\rho_i}\frac{c_i}{X_i}}{cD_{ij}} \\
&= \sum_{j=1,j\neq i}^{n} \frac{X_i \frac{j_j c_j}{\rho_j} - X_j \frac{j_i c_i}{\rho_i}}{cD_{ij}}, \quad i = 1,2,...n
\end{aligned}$$

$$\therefore \nabla X_i = \sum_{j=1,j\neq i}^{n} \frac{X_i \frac{j_j}{M_j} - X_j \frac{j_i}{M_i}}{cD_{ij}}, \quad i = 1,2,...n \tag{6.33}$$

The above Equations can be also written as

$$c\nabla X_i = -j_i \sum_{j=1,j\neq i}^{n} (\frac{X_j}{D_{ij}}\frac{1}{M_i}) + j_j X_i \sum_{j=1,j\neq i}^{n} (\frac{1}{D_{ij}}\frac{1}{M_j}), \quad i = 1,2,...n \tag{6.34}$$

(6.15) can be expressed as

$$j_n = -j_i - \sum_{j=1,j\neq i}^{n-1} j_j \tag{6.35}$$

Split the last term of the right hand side of Eqs. (6.34) into two terms, we get

$$c\nabla X_i = -j_i \sum_{j=1,j\neq i}^{n} (\frac{X_j}{D_{ij}}\frac{1}{M_i}) + j_j X_i \sum_{j=1,j\neq i}^{n-1} (\frac{1}{D_{ij}}\frac{1}{M_j}) + j_n X_i \frac{1}{D_{in}}\frac{1}{M_n}, \quad i = 1,2,...n \tag{6.36}$$

Substituting Eqs. (6.35) into Eqs. (6.36), then we obtain

$$c\nabla X_i = -j_i \sum_{j=1,j\neq i}^{n} (\frac{X_j}{D_{ij}}\frac{1}{M_i}) + j_j X_i \sum_{j=1,j\neq i}^{n-1} (\frac{1}{D_{ij}}\frac{1}{M_j}) + (-j_i - \sum_{j=1,j\neq i}^{n-1} j_j) X_i \frac{1}{D_{in}}\frac{1}{M_n}, \quad i = 1,2,...n-1$$

Finally we get

$$c\nabla X_i = \underbrace{-j_i\,(\frac{X_i}{D_{in}}\frac{1}{M_n} + \sum_{j=1,j\neq i}^{n} (\frac{X_j}{D_{ij}}\frac{1}{M_i}))}_{\text{diagonal}} \underbrace{-j_j\,(-X_i \sum_{j=1,j\neq i}^{n-1} (\frac{1}{D_{ij}}\frac{1}{M_j} - \frac{1}{D_{in}}\frac{1}{M_n}))}_{\text{off-diagonal}}, \quad i = 1,2,...n-1 \tag{6.37}$$

Eqs. (6.37) contain $n-1$ independent equations, they can be written in matrix form as

$$c\nabla \vec{X} = -[B^*]\vec{j} \tag{6.38}$$

where $[B^*]$ is a $(n-1)\times(n-1)$ matrix. The elements of this matrix can be written as

$$B^*_{ii} = \frac{X_i}{D_{in}}\frac{1}{M_n} + \sum_{j=1,j\neq i}^{n} (\frac{X_j}{D_{ij}}\frac{1}{M_i}), \quad i = 1,2,...n-1 \tag{6.39}$$

$$B^*_{ij(i\neq j)} = -X_i(\frac{1}{D_{ij}}\frac{1}{M_j} - \frac{1}{D_{in}}\frac{1}{M_n}), \quad i = 1,2,...n-1 \tag{6.40}$$

which is the mass-based matrix form of Maxwell-Stefan relationship with respect of gradient of molar fraction. The mass diffusion flux can be calculated as

$$\vec{j} = -c[B^*]^{-1}\nabla\vec{X} \tag{6.41}$$

or

$$\vec{j} = -\frac{\rho}{M}[B^*]^{-1}\nabla\vec{X} \tag{6.42}$$

which is according to Eq. (6.7).

6.3.4 Relationship between gradient of mass fraction and gradient of molar fraction

If we substitute Eq. (6.42) into Eqs. (6.31), it is still difficult to solve those equations using numerical methodes. The reason is that, the $\vec{j}$ in Eq. (6.42) is a function of molar fraction gradient, not a function of mass fraction gradient. Therefore, it is nesscerary to find the relationship between gradient of mass fraction and gradient of molar fraction. From Eq. (6.9) we get

$$\begin{aligned}\sum_{i=1}^{n}(\nabla X_i) &= \nabla X_1 + \nabla X_2 + \cdots + \nabla X_n \\ &= \nabla X_1 + \nabla X_2 + \cdots + \nabla X_{n-1} + \nabla(1 - X_1 - X_2 - \cdots - X_{n-1})\end{aligned}$$

$$\therefore \sum_{i=1}^{n}(\nabla X_i) = 0 \tag{6.43}$$

Similarly, it is easy to obtain

$$\sum_{i=1}^{n}(\nabla Y_i) = 0 \tag{6.44}$$

From Eq. (6.10) we find

$$\nabla X_i = \frac{\nabla M}{M_i} Y_i + \frac{M}{M_i}\nabla Y_i \tag{6.45}$$

Substituting Eqs. (6.45) into Eqs. (6.43), then we get

$$(\frac{\nabla M}{M_1}Y_1 + \frac{M}{M_1}\nabla Y_1) + (\frac{\nabla M}{M_2}Y_2 + \frac{M}{M_2}\nabla Y_2) + \cdots + (\frac{\nabla M}{M_n}Y_n + \frac{M}{M_n}\nabla Y_n) = 0$$

$$\nabla M(\frac{Y_1}{M_1} + \frac{Y_2}{M_2} + \cdots + \frac{Y_n}{M_n}) = -(\frac{M}{M_1}\nabla Y_1 + \frac{M}{M_2}\nabla Y_2 + \cdots + \frac{M}{M_n}\nabla Y_n)$$

Substituting Eqs. (6.6) into above equation, then we find

$$\nabla M = -M^2 \sum_{i=1}^{n} \frac{\nabla Y_i}{M_i} \tag{6.46}$$

Substituting Eqs. (6.46) into Eqs. (6.45) , then we find

$$\nabla X_i = \frac{M}{M_i}(\nabla Y_i - Y_i \sum_{j=1}^{n}(\frac{M}{M_j}\nabla Y_j)), \quad i = 1, 2, ...n \tag{6.47}$$

From Eq. (6.44) we obtain

$$\nabla Y_n = -(\nabla Y_1 + \nabla Y_2 + \cdots + \nabla Y_{n-1}) \tag{6.48}$$

Substituting Eqs. (6.48) into Eqs. (6.47) , then we get

$$\nabla X_i = \frac{M}{M_i}(\nabla Y_i - Y_i \sum_{j=1}^{n-1}((\frac{M}{M_j} - \frac{M}{M_n})\nabla Y_j)), \quad i = 1, 2, ...n-1 \tag{6.49}$$

Then we take the term of $i = j$ out of the sum, finally it becomes

$$\nabla X_i = \frac{M}{M_i}\underbrace{((1 + Y_i(\frac{M}{M_n} - \frac{M}{M_i}))}_{\text{diagonal}}\nabla Y_i + \underbrace{Y_i \sum_{j=1, j\neq i}^{n-1}(\frac{M}{M_n} - \frac{M}{M_j})\nabla Y_j)}_{\text{off-diagonal}}, \quad i = 1, 2, ...n-1 \tag{6.50}$$

Eqs. (6.50) contain $n - 1$ independent equations, they can be written in matrix form as

$$\nabla \vec{X} = [W]\nabla \vec{Y} \tag{6.51}$$

where $[W]$ is a $(n - 1) \times (n - 1)$ matrix. The elements of this matrix can be written as

$$W_{ii} = \frac{M}{M_i} + Y_i \frac{M}{M_i}(\frac{M}{M_n} - \frac{M}{M_i}), \quad i = 1, 2, ...n-1 \tag{6.52}$$

$$W_{ij(i\neq j)} = Y_i \frac{M}{M_i}(\frac{M}{M_n} - \frac{M}{M_j}), \quad i = 1, 2, ...n-1 \tag{6.53}$$

or

$$W_{ii} = \frac{M}{M_i} + X_i(\frac{M}{M_n} - \frac{M}{M_i}), \quad i = 1, 2, ...n-1 \tag{6.54}$$

$$W_{ij(i\neq j)} = X_i(\frac{M}{M_n} - \frac{M}{M_j}), \quad i = 1, 2, ...n-1 \tag{6.55}$$

6.3.5 Mass-based matrix form of Maxwell-Stefan relationship with respect of gradient of mass fraction

Substituting Eqs. (6.51), (6.54) and (6.55) into (6.42), then we find

$$\vec{j} = -\sum_{j=1}^{n-1} \rho[B^*]^{-1}[W]\nabla \vec{Y} \tag{6.56}$$

$$B^*_{ii} = \frac{X_i}{D_{in}}\frac{1}{M_n} + \sum_{j=1, j\neq i}^{n} \frac{X_j}{D_{ij}}\frac{1}{M_i}, \quad i = 1, 2, ...n-1 \tag{6.57}$$

$$B^*_{ij(i\neq j)} = -X_i(\frac{1}{D_{ij}}\frac{1}{M_j} - \frac{1}{D_{in}}\frac{1}{M_n}), \quad i = 1, 2, ...n-1 \tag{6.58}$$

$$W_{ii} = \frac{1}{M_i} + X_i(\frac{1}{M_n} - \frac{1}{M_i}), \quad i = 1, 2, ...n-1 \tag{6.59}$$

$$W_{ij(i \neq j)} = X_i(\frac{1}{M_n} - \frac{1}{M_j}), \quad i = 1, 2, ...n-1 \tag{6.60}$$

Bibliography

[1] N. Armaroli and V. Balzani, “The future of energy supply: challenges and opportunities,” *Angewandte Chemie International Edition*, vol. 46, no. 1-2, pp. 52–66, 2007.

[2] G. P. Robertson, E. A. Paul, and R. R. Harwood, “Greenhouse gases in intensive agriculture: contributions of individual gases to the radiative forcing of the atmosphere,” *Science*, vol. 289, no. 5486, pp. 1922–1925, 2000.

[3] J. M. Ogden, M. M. Steinbugler, and T. G. Kreutz, “A comparison of hydrogen, methanol and gasoline as fuels for fuel cell vehicles: implications for vehicle design and infrastructure development,” *Journal of Power Sources*, vol. 79, no. 2, pp. 143–168, 1999.

[4] J. Pasel, J. Meißner, Z. Porš, R. Samsun, A. Tschauder, and R. Peters, “Autothermal reforming of commercial Jet A-1 on a scale,” *International Journal of Hydrogen Energy*, vol. 32, no. 18, pp. 4847–4858, 2007.

[5] R. C. Samsun, J. Pasel, R. Peters, and D. Stolten, “Fuel cell systems with reforming of petroleum-based and synthetic-based diesel and kerosene fuels for APU applications,” *International Journal of Hydrogen Energy*, vol. 40, no. 19, pp. 6405–6421, 2015.

[6] H. Dhar, L. Christner, and A. Kush, “Nature of CO adsorption during H_2 oxidation in relation to modeling for CO poisoning of a fuel cell anode,” *Journal of the Electrochemical Society*, vol. 134, no. 12, pp. 3021–3026, 1987.

[7] G. Camara, E. Ticianelli, S. Mukerjee, S. Lee, and J. McBreen, “The CO poisoning mechanism of the hydrogen oxidation reaction in proton exchange membrane fuel cells,” *Journal of The Electrochemical Society*, vol. 149, no. 6, pp. A748–A753, 2002.

[8] S. Gottesfeld and J. Pafford, “A new approach to the problem of carbon monoxide poisoning in fuel cells operating at low temperatures,” *Journal of the Electrochemical Society*, vol. 135, no. 10, pp. 2651–2652, 1988.

[9] Q. Li, J. O. Jensen, R. F. Savinell, and N. J. Bjerrum, “High temperature proton exchange membranes based on polybenzimidazoles for fuel cells,” *Progress in Polymer Science*,

vol. 34, no. 5, pp. 449–477, 2009.

[10] A. Chandan, M. Hattenberger, A. El-Kharouf, S. Du, A. Dhir, V. Self, B. G. Pollet, A. Ingram, and W. Bujalski, “High temperature (HT) polymer electrolyte membrane fuel cells (PEMFC)–A review,” *Journal of Power Sources*, vol. 231, pp. 264–278, 2013.

[11] R. C. Samsun, C. Wiethege, J. Pasel, H. Janßen, W. Lehnert, and R. Peters, “HT-PEFC systems operating with diesel and kerosene for APU application,” *Energy Procedia*, vol. 29, pp. 541–551, 2012.

[12] Q. Li, R. He, J. Jensen, and N. Bjerrum, “PBI-based polymer membranes for high temperature fuel cells–preparation, characterization and fuel cell demonstration,” *Fuel Cells*, vol. 4, no. 3, pp. 147–159, 2004.

[13] J. Wainright, J. Wang, D. Weng, R. Savinell, and M. Litt, “Acid-doped polybenzimidazoles: A new polymer electrolyte,” *Journal of the Electrochemical Society*, vol. 142, no. 7, pp. L121–L123, 1995.

[14] M. Reissig, J. Mathé, S. Planitzer, R. Vötter, and J. Rechberger, “Standalone portable SOFC power generator for autonomous operation,” *ECS Transactions*, vol. 68, no. 1, pp. 143–150, 2015.

[15] H. G. Weller, G. Tabor, H. Jasak, and C. Fureby, “A tensorial approach to computational continuum mechanics using object-oriented techniques,” *Computers in Physics*, vol. 12, no. 6, pp. 620–631, 1998.

[16] A. Kulikovsky, *Analytical modelling of fuel cells*. Amsterdam: Elsevier, 2010.

[17] C. Hartnig and T. J. Schmidt, “On a new degradation mode for high-temperature polymer electrolyte fuel cells: How bipolar plate degradation affects cell performance,” *Electrochimica Acta*, vol. 56, no. 11, pp. 4237–4242, 2011.

[18] V. Weissbecker, K. Wippermann, and W. Lehnert, “Electrochemical corrosion study of metallic materials in phosphoric acid as bipolar plates for HT-PEFCs,” *Journal of The Electrochemical Society*, vol. 161, no. 14, pp. F1437–F1447, 2014.

[19] C. Hartnig, L. Jörissen, J. Kerres, W. Lehnert, and J. Scholta, “Polymer electrolyte membrane fuel cells,” *Materials for Fuel Cells*, pp. 101–184, 2008.

[20] E. Antolini, J. R. Salgado, and E. R. Gonzalez, “The stability of Pt-M (M= first row transition metal) alloy catalysts and its effect on the activity in low temperature fuel cells: a literature review and tests on a Pt-Co catalyst,” *Journal of Power Sources*, vol. 160, no. 2,

pp. 957–968, 2006.

[21] U. Paulus, A. Wokaun, G. Scherer, T. Schmidt, V. Stamenkovic, N. Markovic, and P. Ross, "Oxygen reduction on high surface area Pt-based alloy catalysts in comparison to well defined smooth bulk alloy electrodes," *Electrochimica Acta*, vol. 47, no. 22, pp. 3787–3798, 2002.

[22] F. Liu, S. Mohajeri, Y. Di, K. Wippermann, and W. Lehnert, "Influence of the interaction between phosphoric acid and catalyst layers on the properties of HT-PEFCs," *Fuel Cells*, vol. 14, no. 5, pp. 750–757, 2014.

[23] U. R. Salomov, E. Chiavazzo, and P. Asinari, "Gas-dynamic and electro-chemical optimization of catalyst layers in high temperature polymeric electrolyte membrane fuel cells," *International Journal of Hydrogen Energy*, vol. 40, no. 15, pp. 5425–5431, 2015.

[24] Y. Ma, *The fundamental studies of polybenzimidazole/phosphoric acid polymer electrolyte for fuel cells*. PhD thesis, Case Western Reserve University, 2004.

[25] J. Fontanella, M. Wintersgill, J. Wainright, R. Savinell, and M. Litt, "High pressure electrical conductivity studies of acid doped polybenzimidazole," *Electrochimica Acta*, vol. 43, no. 10, pp. 1289–1294, 1998.

[26] M. S. Kondratenko, M. O. Gallyamov, and A. R. Khokhlov, "Performance of high temperature fuel cells with different types of PBI membranes as analysed by impedance spectroscopy," *International Journal of Hydrogen Energy*, vol. 37, no. 3, pp. 2596–2602, 2012.

[27] K. Neyerlin, A. Singh, and D. Chu, "Kinetic characterization of a Pt-Ni/C catalyst with a phosphoric acid doped PBI membrane in a proton exchange membrane fuel cell," *Journal of Power Sources*, vol. 176, no. 1, pp. 112–117, 2008.

[28] F. Barbir, *PEM fuel cells: theory and practice*. Amsterdam: Academic Press, 2005.

[29] J. Zhang, *PEM fuel cell electrocatalysts and catalyst layers: fundamentals and applications*. Berlin, Heidelberg: Springer Science & Business Media, 2008.

[30] E. L. Cussler, *Diffusion: mass transfer in fluid systems*. Cambridge: Cambridge University Press, 2009.

[31] G. Biswas, *Introduction to fluid mechanics and fluid machines*. New York: McGraw-Hill Education, 2003.

[32] M. M. Mench, *Fuel cell engines*. Hoboken: John Wiley & Sons, 2008.

[33] H. Schlichting and K. Gersten, *Boundary-layer theory*. Berlin, Heidelberg: Springer Science & Business Media, 2000.

[34] B. Sultanian, *Fluid mechanics: an intermediate approach*. Boca Raton: CRC Press, 2015.

[35] Verein Deutscher Ingenieure, *VDI-Wärmeatlas: Berechnungsblätter für den Wärmeübergang*. Berlin, Heidelberg: Springer, 2002.

[36] Z. Liu, J. S. Wainright, and R. F. Savinell, "High-temperature polymer electrolytes for PEM fuel cells: study of the oxygen reduction reaction (ORR) at a Pt-polymer electrolyte interface," *Chemical Engineering Science*, vol. 59, no. 22, pp. 4833–4838, 2004.

[37] Q. Li, R. He, J. Gao, J. O. Jensen, and N. J. Bjerrum, "The CO poisoning effect in PEMFCs operational at temperatures up to 200°C," *Journal of the Electrochemical Society*, vol. 150, no. 12, pp. A1599–A1605, 2003.

[38] J. Supra, H. Janßen, W. Lehnert, and D. Stolten, "Temperature distribution in a liquid-cooled HT-PEFC stack," *International Journal of Hydrogen Energy*, vol. 38, no. 4, pp. 1943–1951, 2013.

[39] J. Scholta, W. Zhang, L. Jörissen, and W. Lehnert, "Conceptual design for an externally cooled HT-PEMFC stack," *ECS Transactions*, vol. 12, no. 1, pp. 113–118, 2008.

[40] K. Saito, T. Tazaki, R. Matsubara, and H. Nishide, "Acid-functionalized poly(phenylene oxide)s: Their preparation and properties," *Industrial & Engineering Chemistry Research*, vol. 44, no. 23, pp. 8626–8630, 2005.

[41] M. S. Kondratenko, M. O. Gallyamov, O. A. Tyutyunnik, I. V. Kubrakova, A. V. Chertovich, E. K. Malinkina, and G. A. Tsirlina, "Degradation of high temperature polymer electrolyte fuel cell cathode material as affected by polybenzimidazole," *Journal of The Electrochemical Society*, vol. 162, no. 6, pp. F587–F595, 2015.

[42] T. E. Springer, T. Zawodzinski, and S. Gottesfeld, "Polymer electrolyte fuel cell model," *Journal of the Electrochemical Society*, vol. 138, no. 8, pp. 2334–2342, 1991.

[43] D. M. Bernardi and M. W. Verbrugge, "Mathematical model of a gas diffusion electrode bonded to a polymer electrolyte," *AIChE journal*, vol. 37, no. 8, pp. 1151–1163, 1991.

[44] M. W. Verbrugge and R. F. Hill, "Ion and solvent transport in ion-exchange membranes

I: A macrohomogeneous mathematical model," *Journal of the Electrochemical Society*, vol. 137, no. 3, pp. 886–893, 1990.

[45] T. F. Fuller and J. Newman, "Water and thermal management in solid-polymer-electrolyte fuel cells," *Journal of the Electrochemical Society*, vol. 140, no. 5, pp. 1218–1225, 1993.

[46] T. V. Nguyen and R. E. White, "A water and heat management model for proton exchange membrane fuel cells," *Journal of the Electrochemical Society*, vol. 140, no. 8, pp. 2178–2186, 1993.

[47] J. Kim, S.-M. Lee, S. Srinivasan, and C. E. Chamberlin, "Modeling of proton exchange membrane fuel cell performance with an empirical equation," *Journal of the Electrochemical Society*, vol. 142, no. 8, pp. 2670–2674, 1995.

[48] A. West and T. Fuller, "Influence of rib spacing in proton-exchange membrane electrode assemblies," *Journal of Applied Electrochemistry*, vol. 26, no. 6, pp. 557–565, 1996.

[49] M. L. Perry, J. Newman, and E. J. Cairns, "Mass transport in gas-diffusion electrodes: A diagnostic tool for fuel-cell cathodes," *Journal of The Electrochemical Society*, vol. 145, no. 1, pp. 5–15, 1998.

[50] M. Eikerling and A. Kornyshev, "Modelling the performance of the cathode catalyst layer of polymer electrolyte fuel cells," *Journal of Electroanalytical Chemistry*, vol. 453, no. 1, pp. 89–106, 1998.

[51] M. Wöhr, K. Bolwin, W. Schnurnberger, M. Fischer, W. Neubrand, and G. Eigenberger, "Dynamic modelling and simulation of a polymer membrane fuel cell including mass transport limitation," *International Journal of Hydrogen Energy*, vol. 23, no. 3, pp. 213–218, 1998.

[52] H. P. van Bussel, F. G. Koene, and R. K. Mallant, "Dynamic model of solid polymer fuel cell water management," *Journal of Power Sources*, vol. 71, no. 1, pp. 218–222, 1998.

[53] Y. Bultel, P. Ozil, and R. Durand, "Modelling the mode of operation of PEMFC electrodes at the particle level: influence of ohmic drop within the active layer on electrode performance," *Journal of Applied Electrochemistry*, vol. 28, no. 3, pp. 269–276, 1998.

[54] J. Baschuk and X. Li, "Modelling of polymer electrolyte membrane fuel cells with variable degrees of water flooding," *Journal of Power Sources*, vol. 86, no. 1, pp. 181–196, 2000.

[55] A. Z. Weber and J. Newman, "Transport in polymer-electrolyte membranes I: Physical model," *Journal of the Electrochemical Society*, vol. 150, no. 7, pp. A1008–A1015, 2003.

[56] S. Chan, S. Goh, and S. Jiang, “A mathematical model of polymer electrolyte fuel cell with anode CO kinetics,” *Electrochimica Acta*, vol. 48, no. 13, pp. 1905–1919, 2003.

[57] A. R. Korsgaard, M. P. Nielsen, and S. K. Kær, “Part one: a novel model of HTPEM-based micro-combined heat and power fuel cell system,” *International Journal of Hydrogen Energy*, vol. 33, no. 7, pp. 1909–1920, 2008.

[58] O. Shamardina, A. Chertovich, A. Kulikovsky, and A. Khokhlov, “A simple model of a high temperature PEM fuel cell,” *International Journal of Hydrogen Energy*, vol. 35, no. 18, pp. 9954–9962, 2010.

[59] A. Kulikovsky, H.-F. Oetjen, and C. Wannek, “A simple and accurate method for high-temperature PEM fuel cell characterisation,” *Fuel Cells*, vol. 10, no. 3, pp. 363–368, 2010.

[60] A. Kulikovsky, “A physically–based analytical polarization curve of a PEM fuel cell,” *Journal of The Electrochemical Society*, vol. 161, no. 3, pp. F263–F270, 2014.

[61] A. Kulikovsky, “Analytical solutions for polarization curve and impedance of the cathode catalyst layer with fast oxygen transport in a PEM fuel cell,” *Journal of the Electrochemical Society*, vol. 161, no. 8, pp. E3171–E3179, 2014.

[62] V. Gurau, H. Liu, and S. Kakac, “Two-dimensional model for proton exchange membrane fuel cells,” *AIChE Journal*, vol. 44, no. 11, pp. 2410–2422, 1998.

[63] E. Ticianelli, C. Derouin, and S. Srinivasan, “Localization of platinum in low catalyst loading electrodes to to attain high power densities in SPE fuel cells,” *Journal of Electroanalytical Chemistry*, vol. 251, no. 2, pp. 275–295, 1988.

[64] N. Djilali and D. Lu, “A multi-component, multi-dimensional model for heat and mass transport in proton-exchange membrane fuel cells,” in *Proceedings of the 1998 Fuel Cell Seminar*, vol. 16, p. 1998, 1998.

[65] S. Um, C. Wang, and K. Chen, “Computational fluid dynamics modeling of proton exchange membrane fuel cells,” *Journal of the Electrochemical Society*, vol. 147, no. 12, pp. 4485–4493, 2000.

[66] Z. Wang, C. Wang, and K. Chen, “Two-phase flow and transport in the air cathode of proton exchange membrane fuel cells,” *Journal of Power Sources*, vol. 94, no. 1, pp. 40–50, 2001.

[67] S. Dutta, S. Shimpalee, and J. Van Zee, “Numerical prediction of mass-exchange between cathode and anode channels in a PEM fuel cell,” *International Journal of Heat and*

Mass Transfer, vol. 44, no. 11, pp. 2029–2042, 2001.

[68] S. Mazumder and J. V. Cole, “Rigorous 3-D mathematical modeling of PEM fuel cells II: Model predictions with liquid water transport,” *Journal of the Electrochemical Society*, vol. 150, no. 11, pp. A1510–A1517, 2003.

[69] S. Um and C. Wang, “Three-dimensional analysis of transport and electrochemical reactions in polymer electrolyte fuel cells,” *Journal of Power Sources*, vol. 125, no. 1, pp. 40–51, 2004.

[70] P. T. Nguyen, T. Berning, and N. Djilali, “Computational model of a PEM fuel cell with serpentine gas flow channels,” *Journal of Power Sources*, vol. 130, no. 1, pp. 149–157, 2004.

[71] K. W. Lum and J. J. McGuirk, “Three-dimensional model of a complete polymer electrolyte membrane fuel cell - model formulation, validation and parametric studies,” *Journal of Power Sources*, vol. 143, no. 1, pp. 103–124, 2005.

[72] N. Siegel, M. Ellis, D. Nelson, and M. Von Spakovsky, “A two-dimensional computational model of a PEMFC with liquid water transport,” *Journal of Power Sources*, vol. 128, no. 2, pp. 173–184, 2004.

[73] S. Shimpalee, U. Beuscher, and J. Van Zee, “Analysis of GDL flooding effects on PEMFC performance,” *Electrochimica Acta*, vol. 52, no. 24, pp. 6748–6754, 2007.

[74] F. Hashemi, S. Rowshanzamir, and M. Rezakazemi, “CFD simulation of PEM fuel cell performance: effect of straight and serpentine flow fields,” *Mathematical and Computer Modelling*, vol. 55, no. 3, pp. 1540–1557, 2012.

[75] S.-J. Cheng, J.-M. Miao, and S.-J. Wu, “Investigating the effects of operational factors on PEMFC performance based on CFD simulations using a three-level full-factorial design,” *Renewable Energy*, vol. 39, no. 1, pp. 250–260, 2012.

[76] A. Iranzo, P. Boillat, and F. Rosa, “Validation of a three dimensional PEM fuel cell CFD model using local liquid water distributions measured with neutron imaging,” *International Journal of Hydrogen Energy*, vol. 39, no. 13, pp. 7089–7099, 2014.

[77] W.-J. Yang, H.-Y. Wang, D.-H. Lee, and Y.-B. Kim, “Channel geometry optimization of a polymer electrolyte membrane fuel cell using genetic algorithm,” *Applied Energy*, vol. 146, pp. 1–10, 2015.

[78] D. Cheddie and N. Munroe, “Three dimensional modeling of high temperature PEM fuel

cells," *Journal of Power Sources*, vol. 160, no. 1, pp. 215–223, 2006.

[79] D. Cheddie and N. Munroe, "A two-phase model of an intermediate temperature PEM fuel cell," *International Journal of Hydrogen Energy*, vol. 32, no. 7, pp. 832–841, 2007.

[80] J. Peng and S. J. Lee, "Numerical simulation of proton exchange membrane fuel cells at high operating temperature," *Journal of Power Sources*, vol. 162, no. 2, pp. 1182–1191, 2006.

[81] E. Ubong, Z. Shi, and X. Wang, "Three-dimensional modeling and experimental study of a high temperature PBI-based PEM fuel cell," *Journal of the Electrochemical Society*, vol. 156, no. 10, pp. B1276–B1282, 2009.

[82] J. Lobato, P. Cañizares, M. A. Rodrigo, F. J. Pinar, E. Mena, and D. Úbeda, "Three-dimensional model of a 50 cm^2 high temperature PEM fuel cell. study of the flow channel geometry influence," *International Journal of Hydrogen Energy*, vol. 35, no. 11, pp. 5510–5520, 2010.

[83] T. Sousa, M. Mamlouk, and K. Scott, "An isothermal model of a laboratory intermediate temperature fuel cell using PBI doped phosphoric acid membranes," *Chemical Engineering Science*, vol. 65, no. 8, pp. 2513–2530, 2010.

[84] T. Sousa, M. Mamlouk, and K. Scott, "A dynamic non-isothermal model of a laboratory intermediate temperature fuel cell using PBI doped phosphoric acid membranes," *International Journal of Hydrogen Energy*, vol. 35, no. 21, pp. 12065–12080, 2010.

[85] G. Doubek, E. Robalinho, E. Cunha, E. Cekinski, and M. Linardi, "Application of CFD techniques in the modelling and simulation of PBI PEMFC," *Fuel Cells*, vol. 11, no. 6, pp. 764–774, 2011.

[86] K. Jiao and X. Li, "A three-dimensional non-isothermal model of high temperature proton exchange membrane fuel cells with phosphoric acid doped polybenzimidazole membranes," *Fuel Cells*, vol. 10, no. 3, pp. 351–362, 2010.

[87] G. Falcucci, E. Jannelli, M. Minutillo, and S. Ubertini, "Fluid dynamic investigation of channel design in high temperature pem fuel cells," *Journal of Fuel Cell Science and Technology*, vol. 9, no. 2, p. 021014, 2012.

[88] J. Park and K. Min, "A quasi-three-dimensional non-isothermal dynamic model of a high-temperature proton exchange membrane fuel cell," *Journal of Power Sources*, vol. 216, pp. 152–161, 2012.

[89] P. Chippar, K. Oh, D. Kim, T.-W. Hong, W. Kim, and H. Ju, “Coupled mechanical stress and multi-dimensional CFD analysis for high temperature proton exchange membrane fuel cells (HT-PEMFCs),” *International Journal of Hydrogen Energy*, vol. 38, no. 18, pp. 7715–7724, 2013.

[90] M. Kvesić, U. Reimer, D. Froning, L. Lüke, W. Lehnert, and D. Stolten, “3D modeling of a 200 cm^2 HT-PEFC short stack,” *International Journal of Hydrogen Energy*, vol. 37, no. 3, pp. 2430–2439, 2012.

[91] V. K. Krastev, G. Falcucci, E. Jannelli, M. Minutillo, and R. Cozzolino, “3D CFD modeling and experimental characterization of HT-PEM fuel cells at different anode gas compositions,” *International Journal of Hydrogen Energy*, vol. 39, no. 36, pp. 21663–21672, 2014.

[92] K. Oh, P. Chippar, and H. Ju, “Numerical study of thermal stresses in high-temperature proton exchange membrane fuel cell (HT-PEMFC),” *international journal of hydrogen energy*, vol. 39, no. 6, pp. 2785–2794, 2014.

[93] T. J. Kazdal, S. Lang, F. Kühl, and M. J. Hampe, “Modelling of the vapour-liquid equilibrium of water and the in situ concentration of H_3PO_4 in a high temperature proton exchange membrane fuel cell,” *Journal of Power Sources*, vol. 249, pp. 446–456, 2014.

[94] S. B. Beale, H. K. Roth, A. Le, and D. H. Jeon, “Development of an open source software library for solid oxide fuel cells,” tech. rep., National Research Council Canada, No. PET-1607-12, 2013.

[95] S. B. Beale, H.-W. Choi, J. G. Pharoah, H. K. Roth, H. Jasak, and D. H. Jeon, “Open-source computational model of a solid oxide fuel cell,” *Computer Physics Communications*, vol. 200, pp. 15–26, 2016.

[96] *The openFuelCell project*. `http://openfuelcell.sourceforge.net/project`.

[97] S. Keuler, “Generisches, OpenFOAM-basiertes Brennstoffzellenmodell angewandt auf die Hochtemperatur-Polymerelektrolyt-Brennstoffzelle,” Master’s thesis, Fachhochschule Aachen, Campus Jülich, 2013.

[98] H. E. Hafsteinsson, “Porous media in OpenFOAM,” *Chalmers University of Technology, Gothenburg*, 2009.

[99] A. Fick, “Ueber Diffusion,” *Annalen der Physik*, vol. 170, no. 1, pp. 59–86, 1855.

[100] E. N. Fuller, P. Schettler, and J. C. Giddings, “New method for prediction of binary gas-

phase diffusion coefficients," *Industrial & Engineering Chemistry*, vol. 58, no. 5, pp. 18–27, 1966.

[101] E. N. Fuller, K. Ensley, and J. C. Giddings, "Diffusion of halogenated hydrocarbons in helium. the effect of structure on collision cross sections," *The Journal of Physical Chemistry*, vol. 73, no. 11, pp. 3679–3685, 1969.

[102] F. Zhao, T. J. Armstrong, and A. V. Virkar, "Measurement of O_2-N_2 effective diffusivity in porous media at high temperatures using an electrochemical cell," *Journal of the Electrochemical Society*, vol. 150, no. 3, pp. A249–A256, 2003.

[103] J. G. Christie, "Transport processes and unit operations," *Prentice-Hall International, Inc*, pp. 393–397, 1993.

[104] D. F. Fairbanks and C. R. Wilke, "Diffusion coefficients in multicomponent gas mixtures," *Industrial & Engineering Chemistry*, vol. 42, no. 3, pp. 471–475, 1950.

[105] M. M. Rathore, *Thermal engineering*. New York: Tata McGraw-Hill Education, 2010.

[106] B. Todd and J. Young, "Thermodynamic and transport properties of gases for use in solid oxide fuel cell modelling," *Journal of Power Sources*, vol. 110, no. 1, pp. 186–200, 2002.

[107] C. Tötzke, G. Gaiselmann, M. Osenberg, J. Bohner, T. Arlt, H. Markötter, A. Hilger, F. Wieder, A. Kupsch, B. Müller, *et al.*, "Three-dimensional study of compressed gas diffusion layers using synchrotron X-ray imaging," *Journal of Power Sources*, vol. 253, pp. 123–131, 2014.

[108] D. Cheddie and N. Munroe, "Mathematical model of a PEMFC using a PBI membrane," *Energy Conversion and Management*, vol. 47, no. 11, pp. 1490–1504, 2006.

[109] A. Su, Y. Ferng, and J. Shih, "CFD investigating the effects of different operating conditions on the performance and the characteristics of a high-temperature PEMFC," *Energy*, vol. 35, no. 1, pp. 16–27, 2010.

[110] A. J. Bard, L. R. Faulkner, J. Leddy, and C. G. Zoski, *Electrochemical methods: fundamentals and applications*, vol. 2. New York: Wiley, 1980.

[111] M. Mathias, J. Roth, J. Fleming, and W. Lehnert, "Diffusion media materials and characterization," in *Handbook of fuel cells—fundamentals, technology and applications*, New York: Wiley, 2003.

[112] J. Dawes, N. Hanspal, O. Family, and A. Turan, "Three-dimensional CFD modelling of

PEM fuel cells: an investigation into the effects of water flooding," *Chemical Engineering Science*, vol. 64, no. 12, pp. 2781–2794, 2009.

[113] S. Cordiner, S. P. Lanzani, and V. Mulone, "3D effects of water-saturation distribution on polymeric electrolyte fuel cell (PEFC) performance," *International Journal of Hydrogen Energy*, vol. 36, no. 16, pp. 10366–10375, 2011.

[114] A. Z. Weber, R. M. Darling, and J. Newman, "Modeling two-phase behavior in PEFCs," *Journal of the Electrochemical Society*, vol. 151, no. 10, pp. A1715–A1727, 2004.

[115] F. Liu, *Interaction of phosphoric acid with cell components in high temperature polymer electrolyte fuel cells*. Jülich: Forschungszentrum Jülich GmbH, 2014.

[116] U. Reimer, J. Ehlert, H. Janssen, and W. Lehnert, "Water distribution in high temperature polymer electrolyte fuel cells," *International journal of hydrogen energy*, vol. 41, no. 3, pp. 1837–1845, 2016.

[117] W. Maier, T. Arlt, C. Wannek, I. Manke, H. Riesemeier, P. Krüger, J. Scholta, W. Lehnert, J. Banhart, and D. Stolten, "In-situ synchrotron X-ray radiography on high temperature polymer electrolyte fuel cells," *Electrochemistry Communications*, vol. 12, no. 10, pp. 1436–1438, 2010.

[118] W. Dai, H. Wang, X.-Z. Yuan, J. J. Martin, D. Yang, J. Qiao, and J. Ma, "A review on water balance in the membrane electrode assembly of proton exchange membrane fuel cells," *International Journal of Hydrogen Energy*, vol. 34, no. 23, pp. 9461–9478, 2009.

[119] D. Weng, J. S. Wainright, U. Landau, and R. F. Savinell, "Electro-osmotic drag coefficient of water and methanol in polymer electrolytes at elevated temperatures," *Journal of the Electrochemical Society*, vol. 143, no. 4, pp. 1260–1263, 1996.

[120] P. Chippar, K. Kang, Y.-D. Lim, W.-G. Kim, and H. Ju, "Effects of inlet relative humidity (RH) on the performance of a high temperature-proton exchange membrane fuel cell (HT-PEMFC)," *International Journal of Hydrogen Energy*, vol. 39, no. 6, pp. 2767–2775, 2014.

[121] A. Schechter, R. F. Savinell, J. S. Wainright, and D. Ray, "^{1}H and ^{31}P NMR study of phosphoric acid-doped polybenzimidazole under controlled water activity," *Journal of the Electrochemical Society*, vol. 156, no. 2, pp. B283–B290, 2009.

[122] DDBST, *Saturated Vapor Pressure Calculation by Antoine Equation*. `http://ddbonline.ddbst.de/AntoineCalculation/AntoineCalculationCGI.exe`.

[123] S. B. Beale, “Mass transfer formulation for polymer electrolyte membrane fuel cell cathode,” *International Journal of Hydrogen Energy*, vol. 40, no. 35, pp. 11641–11650, 2015.

[124] J. A. Wesselingh and R. Krishna, *Mass transfer in multicomponent mixtures*. Delft: Delft University Press, 2000.

[125] R. B. Bird, W. E. Stewart, and E. Lightfoot, *Transport phenomena*, vol. 2. Hoboken: John Wiley & Sons, 2002.

[126] R. Taylor and R. Krishna, *Multicomponent mass transfer*, vol. 2. Hoboken: John Wiley & Sons, 1993.

[127] S. Whitaker, “Derivation and application of the Stefan-Maxwell equations,” *Revista Mexicana de Ingeniería Química*, vol. 8, no. 3, pp. 213–244, 2009.

[128] H. Jasak, H. Weller, and A. Gosman, “High resolution NVD differencing scheme for arbitrarily unstructured meshes,” *International journal for numerical methods in fluids*, vol. 31, no. 2, pp. 431–449, 1999.

[129] A. Kulikovsky, “The effect of stoichiometric ratio λ on the performance of a polymer electrolyte fuel cell,” *Electrochimica Acta*, vol. 49, no. 4, pp. 617–625, 2004.

[130] D. Cheddie and N. Munroe, “Modeling of high temperature PEM fuel cells using FEMLAB,” in *The COMSOL Multiphysics User’s Conferences, Boston, USA*, 2005.

[131] T. Berning, D. M. Lu, and N. Djilali, “Three-dimensional computational analysis of transport phenomena in a PEM fuel cell,” *Journal of Power Sources*, vol. 106, no. 1, pp. 284–294, 2002.

[132] D. Froning, J. Brinkmann, U. Reimer, V. Schmidt, W. Lehnert, and D. Stolten, “3D analysis, modeling and simulation of transport processes in compressed fibrous microstructures, using the Lattice Boltzmann method,” *Electrochimica Acta*, vol. 110, pp. 325–334, 2013.

[133] COMSOL, *Stefan Tube*. `http://www.comsol.com/model/download/222461/models.chem.stefan_tube.pdf`.

[134] D. M. Bernardi, “Water-balance calculations for solid-polymer-electrolyte fuel cells,” *Journal of the Electrochemical Society*, vol. 137, no. 11, pp. 3344–3350, 1990.

[135] S. Eberhardt, M. Toulec, F. Marone, M. Stampanoni, F. Büchi, and T. Schmidt, “Dynamic operation of HT-PEFC: in-operando imaging of phosphoric acid profiles and (Re) distri-

bution," *Journal of the Electrochemical Society*, vol. 162, no. 3, pp. F310–F316, 2015.

[136] W. Lehnert, U. Reimer, and H. Janßen, "Hochtemperatur-Polymerelektrolyt-Brennstoffzellen," in *Brennstoffzellensysteme in der Luftfahrt*, pp. 101–143, Berlin, Heidelberg: Springer, 2015.

[137] S. B. Beale, "A simple, effective viscosity formulation for turbulent flow and heat transfer in compact heat exchangers," *Heat Transfer Engineering*, vol. 33, no. 1, pp. 4–11, 2012.

[138] M. Mamlouk, T. Sousa, and K. Scott, "A high temperature polymer electrolyte membrane fuel cell model for reformate gas," *International Journal of Electrochemistry*, vol. 2011, 2010.

[139] S. Beale, "Personal communication." unpublished.

Nomenclature

Roman Symbols

$[B]$	$(n-1) \times (n-1)$ matrix	
$[W]$	$(n-1) \times (n-1)$ matrix	
ΔG	Gibbs free energy change of a reaction	kJ mol^{-1}
ΔG^0	Gibbs free energy change of a reaction under the standard condition	kJ mol^{-1}
ΔH	enthalpy change of a reaction	kJ mol^{-1}
ΔH^0	enthalpy change of a reaction under the standard condition	kJ mol^{-1}
ΔS	entropy change of a reaction	kJ mol^{-1} K^{-1}
$\mathbf{d}$	Darcy parameter	
$\mathbf{U}$	velocity vector of gas	m s^{-1}
$\mathbf{U}_b$	velocity of the gas mixture on the electrolyte-GDE interface	m s^{-1}
$\vec{j}$	mass based diffusion flux vector	kg m^{-2} s^{-1}
a	width of the channel	m
b	height of the channel	m
c	molar concentration of mixture	mol m^{-3}
c	speed of sound in the medium	m s^{-1}

C_p	heat capacity	J K^{-1}
$c_{H_2O}^{gas,a}$	molar concentration of water vapor at anode	mol m^{-3}
$c_{H_2O}^{gas,c}$	molar concentration of water vapor at cathode	mol m^{-3}
c_{O_2}	molar concentration of oxygen	mol m^{-3}
c_{ref}	reference molar concentration	mol m^{-3}
Cp_i	heat capacity of species i	J K^{-1}
D_i	multi-component diffusivity of species i	m^2 s^{-1}
d_p	mean diameter of pores in porous media	m
D_{CL}	effective diffusivity of oxygen in CL	m^2 s^{-1}
$D_{H_2O}^{eff}$	effective diffusivity of water	m^2 s^{-1}
$D_{ij,p}$	binary diffusivity for species i and j in porous media	m^2 s^{-1}
D_{ij}	binary diffusivity for species i and j	m^2 s^{-1}
D_{K_n}	Knudsen diffusivity in porous media	m^2 s^{-1}
E_A	activation energy	J mol^{-1}
E_{cell}	cell voltage	V
E_{Nernst}	Nernst potential	V
E_{th}	thermodynamic voltage	V
E_{th}^0	thermodynamic voltage of a reaction under the standard condition	V
F	Faraday constant	C mol^{-1}
F_i	diffusion driven force of species i	kg m s^{-2}

h_F	enthalpy of formation	kJ mol^{-1}
h_P	enthalpy of product	kJ mol^{-1}
h_R	enthalpy of reactant	kJ mol^{-1}
I	local current density	A m^{-2}
i_0	exchange current density	A m^{-2}
i_m	mean current density	A m^{2}
i_*	volumetric exchange current density	A m^{-3}
$i_{ref,w}$	reference current density	A m^{2}
J	mass flux of the gas mixture	kg m^{-2} s^{-1}
j_p	proton current density	A m^{-2}
j_*	superficial exchange current density	A m^{-2}
j_σ	characteristic current density	A m^{-2}
j_{H_2O}	mass based diffusion flux of water	kg m^{-2} s^{-1}
J_i	molar based diffusion flux of species i	mol m^{-2} s^{-1}
j_i	mass based diffusion flux of species i	kg m^{-2} s^{-1}
k	thermal conductivity	W m^{-1} K^{-1}
k_B	Boltzmann constant	J K^{-1}
$k_{H_2O,l}^{eff}$	effective mass transfer coefficient of liquid water	kg m^{-1} s^{-1}
$k_{H_2O}^{eff}$	effective mass transfer coefficient of water	kg m^{-1} s^{-1}
k_{ORR}	reaction rate of ORR	A m^{-3} s^{-1}

L	hydraulic diameter	m
l_e	thickness of electrolyte	m
l_g	geometric characteristic length	m
l_t	thickness of the catalyst layer	m
l_e	thickness of electrolyte	m
M_i	molar mass of species i	g mol^{-1}
M_{H_2O}	molar mass of water	kg mol^{-1}
n	number of electron	
p	pressure of gas mixture	Pa
$p_{H_2O}^{gas}$	partial pressure of water vapor	Pa
p_{sat}	saturation vapor pressure of water	Pa
R_Ω	specific ohmic resistance	Ω m^{-2}
R_p	Darcy resistance	Pa m^{-1}
S_i	source term of species i due to chemical reaction	mol m^{-2} s^{-1}
S_h	volumetric heat source	J m^{-3} s^{-1}
T	temperature	K
T_{ref}	reference temperature	K
u_i	relative velocity of species i	m s^{-1}
v	velocity of the fluid	m s^{-1}
v_i	diffusion volume of species i	m^3

x	displacement	m
x	distance from the membrane	m
x^0	total length of the active zone	m
X_i	mole fraction of species i	
$X_{O_2}(x)$	mole fractions of oxygen along the x direction	
$X_{O_2}^0$	mole fractions of oxygen at the beginning of the active zone	
Y_i	mass fraction of species i	
$Y_{H_2O}^g$	mass fraction of water vapor	
$Y_{H_2O}^{liq,a}$	mass fraction of liquid water at anode	
$Y_{H_2O}^{liq,b}$	mass fraction of liquid water of the liquid-gas interface	
$Y_{H_2O}^{liq,c}$	mass fraction of liquid water at cathode	
$Y_{H_2O}^l$	mass fraction of liquid water in the liquid water in the water-acid-PBI system	
Kn	Knudsen number	
Ma	Mach number	
Pe	Péclet number	
Re	Reynolds number	

Greek Symbols

α	symmetry factor
β	dimensionless parameter
δ_i	relative mass transfer error of species i

η	total overpotential in CL	V
η_0	total overpotential at the membrane-electrolyte interface	V
η_{act}	activation overpotential	V
η_{conc}	concentration overpotential	V
η_{max}	thermodynamic efficiency	
η_{max}^0	thermodynamic efficiency under the standard condition	
η_{ohm}	ohmic overpotential	V
γ	cross over rate of water	
λ	mean free path of the molecules	m
μ	dynamic viscosity of gas	Pa·s
μ_i	dynamic viscosity of species i	Pa s
$\phi_{cons,i}$	mass flux of species i which is consumed by the electrochemical reaction	kg s^{-1}
$\phi_{in,i}$	mass flux of species i on the inlet of the channel	kg s^{-1}
$\phi_{in,i}$	mass flux of species i on the outlet of the channel	kg s^{-1}
ψ	empirical factor	
ρ	density of gas	kg m^{-3}
σ	collision diameter of the diffusing species	m
σ_t	proton resistance of the CL	Ω m^{-1}
τ	average geometric tortuosity of porous media	
ε	average porosity of porous media	

φ	volume rate of reaction	mol m^{-3} s^{-1}
$\zeta_{i,j}$	friction coefficient between species i and j	kg s^{-1}

List of Figures

1.1 The basic structure of HT-PEFC. 13
1.2 Graphite bipolar plates of the single cells for laboratory testing. 15
1.3 Photograph of a GDL used in HT-PEFC. 15
1.4 Channel-rib scenario of a GDL embedded in a fuel cell. Reprinted from [19], with the permission from Elsevier. 16
1.5 Chemical structures of PBI (left) and ABPBI (right). 17
1.6 Schematic diagram of a polarization curve and losses of HT-PEFC. 19

2.1 Cross-section of a single channel pair. 32
2.2 Mesh of single channel pair with 17 mm straight channel (bipolar plates not shown). The active zone is 10 mm, one offset (dead zone) on the inlet side is 5 mm, the other offset (dead zone) on the outlet side is 2 mm. Brown part: channel and GDL at the anode side; green part: channel and GDL at the cathode side; red part: electrolyte and CLs. 33
2.3 Left: geometry of single cell with 5-fold serpentine flow field (bipolar plates not shown); right: an enlarged view of inlet area. 34
2.4 Left: the in-house test cell with 5-fold serpentine flow field; right: the bipolar plate of this single cell. 34
2.5 Numerical algorithm of the basic model. 43
2.6 Schematic of the cathode CL and the profiles of oxygen, protons and overpotential. Redrawn from [60] 45
2.7 Numerical algorithm of the macro-homogeneous model. 49
2.8 Schematic model of water transfer in electrolyte. 51
2.9 Numerical algorithm of the water transfer model. 56
2.10 The movement of species inside a control volume. The control volume is chosen as the reference. Red points: Oxygen; blue points: water; black points: nitrogen. 57
2.11 Numerical algorithm of the multicomponent diffusion model. 60
2.12 Sketch of the finite volume discretization. 61

3.1 Mesh independence studies of the single channel pair geometry. The mean current density was 4000 A/m^2. 67

3.2 Mesh independence studies of the single cell geometry with serpentine flow field. The mean current density was 4000 A/m^2. 67

3.3 Polarisation curve: comparison of numerical results of the basic model (blue solid line) and experimental data (red dash line). 70

3.4 Overpotential of numerical results of the basic model. 71

3.5 Cross-sectional planes for presenting the local distribution of properties at the cathode side. 73

3.6 Comparison of mole fraction distribution of oxygen at low- (2000 Am^{-2}) and high (8000 Am^{-2}) mean current densities on Plane A. 74

3.7 Sketch of sampling lines to present the distributions of the oxygen mole fraction on Plane A. 74

3.8 Comparison of mole fraction distribution of oxygen along sampling line 1 at low- (2000 Am^{-2}) and high (8000 Am^{-2}) mean current densities on Plane A. λ = 2/2. The index 0 indicates the channel inlet while the index 1 indicates the channel outlet. L = 17 mm (the total length of the channel). 76

3.9 Comparison of mole fraction distribution of oxygen along sampling lines 2-4 at low- (2000 Am^{-2}) and high (8000 Am^{-2}) mean current densities on Plane A. λ = 2/2. The index 0 indicates the BPP side while the index 1 indicates the membrane side. Z^0 = 1.3 mm (the height of the channel + GDL). 77

3.10 Comparison of mole fraction distribution of water vapour at low- (2000 Am^{-2}) and high (8000 Am^{-2}) mean current densities on Plane A. 78

3.11 Comparison of magnitude of velocity distribution of gas mixture at low- (2000 Am^{-2}) and high (8000 Am^{-2}) mean current densities on Plane A. 79

3.12 The velocity vectors in the GDL at low- (2000 Am^{-2}) mean current density. Position: the cross section in the middle of the channel. 79

3.13 Comparison of temperature distribution at low- (2000 Am^{-2}) and high (8000 Am^{-2}) mean current densities on Plane A. 80

3.14 Comparison of mole fraction distribution of oxygen at low- (2000 Am^{-2}) and high (8000 Am^{-2}) mean current densities on Plane B. 81

3.15 Sketch of sampling lines to present the distributions of the oxygen mole fraction on Plane B. 82

3.16 Comparison of mole fraction distribution of oxygen along sampling line 1 at low- (2000 Am^{-2}) and high (8000 Am^{-2}) mean current densities on Plane B. λ = 2/2. The index 0 indicates the inlet side while the index 1 indicates the outlet side. X^0 = 10 mm (the length of the active area). 83

3.17 Comparison of mole fraction distribution of oxygen along sampling lines 2-4 at low- (2000 Am^{-2}) and high (8000 Am^{-2}) mean current densities on Plane B. λ = 2/2. The index 0 indicates the middle of the channel while the index 1 indicates the side of the rib. Y^{0} = 1 mm (the half width of the channel + the width of one rib). 84
3.18 Current density distribution at low (2000 Am^{-2}) mean current densities on Plane B. 84
3.19 Current density distribution at high (8000 Am^{-2}) mean current densities on Plane B. 85
3.20 GDL sample compressed by a channel-rib profile. From top to bottom, the engineering strain are 0 %, 10 %, 18 %, and 29 %. Reprinted from [107], with permission from Elsevier. 88
3.21 Cross section of the meshes corresponding to the engineering strains: 0 %, 10 %, 18 %, and 29 %. 89
3.22 The regions of GDL under the channel and the rib. 89
3.23 Current density distributions at the electrolyte-GDE interfaces with the GDL engineering strains of 0 %, 10 %, 18 % and 29 %. The mean current density of cases was 6000 Am^{-2}. 92
3.24 Mole fraction of oxygen on the cross sections of the cathode channel and GDL with the GDL engineering strains of 0 %, 10 %, 18 % and 29 %. The mean current density of cases was 6000 Am^{-2}. 93
3.25 Mole fraction of oxygen on the cross-sectional plane, which is in the middle of the channel and perpendicular to the MEA, with the GDL engineering strains of 0 %, 10 %, 18 % and 29 %. The mean current density of cases was 6000 Am^{-2}. . 93
3.26 Three sampling lines in the flow field of the cathode side: (A) at the middle of the channel (B) at the top-middle of the GDL and (C) at the top-corner of the GDL. . 94
3.27 The mole fraction of oxygen over the sampling line A. 94
3.28 The mole fraction of oxygen over the sampling line B. 94
3.29 The mole fraction of oxygen over the sampling line C. 95
3.30 Schematic diagram of a Stefan tube [133]. 98
3.31 Comparison of mole fractions in Stefan tube with numerical solution from Taylor and Krishna. Components: acetone($X1$), methanol($X2$) and air($X3$). 98
3.32 Mole fraction of oxygen at the electrolyte-GDE interfaces: comparison of Fick's law and Maxwell-Stefan formulation. 100
3.33 Current density distribution at the electrolyte-GDE interfaces: comparison of Fick's law and Maxwell-Stefan formulation. 101
3.34 Mole fraction of (1) hydrogen, (2) water, (3) carbon dioxide and (4) nitrogen at the electrolyte-GDE interfaces: comparison of Fick's law and Maxwell-Stefan formulation. 104

3.35 Polarisation curve: comparison of numerical results of the basic model (blue), the macro-homogeneous model (green) and experimental data with the serpentine flow field (red). 108
3.36 Overpotential: comparison of numerical results of the basic model (blue) and the macro-homogeneous model (green). The ohmic overpotentials of the both case are not shown. 109
3.37 The proportion of the oxygen transfer loss in the total overpotential as a function of the mean current density. 109
3.38 Comparison of mole fraction distribution of oxygen calculated by the basic model and the macro-homogeneous model at 4000 Am^{-2} mean current densities. . . . 111
3.39 Comparison of current density distribution calculated by the basic model and the macro-homogeneous model at 4000 Am^{-2} mean current densities. 111
3.40 Percentage based histogram of current density distribution of the basic model (blue) and the macro-homogeneous model (green) at 4000 Am^{-2} mean current densities. 112
3.41 Cross-sectional planes for presenting the velocity and temperature distribution. Left: plane A, which is in the middle of the cell; Right: plane B, which is in the middle of the channel and perpendicular to the MEA. 113
3.42 Velocity profile on the cross-sectional plane A (only five channels are showed). . 113
3.43 Velocity profile on the cross-sectional plane B (only the first 25 mm are showed). 114
3.44 Temperature profile on the cross-sectional plane A. The left part is the inlet side and the right part is the outlet side. 114
3.45 Temperature profile on the cross-sectional plane B (only the first 25 mm are showed). 114
3.46 Generated water at the cathode side and anode side: comparison of the CFD simulation and the experiment. 117
3.47 Cross over rate of the generated water: comparison of the model III-a and the experiment. 118
3.48 Mass fraction of water vapour at the electrolyte-GDE interface: comparison of anode side and the cathode side (the model III-a). 120
3.49 Generated water at the cathode side and anode side: comparison of the model III-a, model III-b and the experiment. 121
3.50 Cross over rate of the generated water: comparison of the model III-a, model III-b and the experiment. 122
3.51 Mass fraction of water vapour at the electrolyte-GDE interface: comparison of anode side and the cathode side (the model III-b). 123
3.52 Mass fraction of phosphoric acid at the electrolyte-GDE interface: comparison of anode side and the cathode side (the model III-b). 124

6.1 The experimental data of the polarization curve for the serpentine single cell with the active area of 50 cm^2. The mean current densities were 0 - 8500 Am^{-2}. 132
6.2 The experimental data of the water condensation rate for the serpentine single cell with the active area of 50 cm^2. The mean current densities were 2000 Am^{-2}, 4000 Am^{-2} and 6000 Am^{-2}. 133

List of Tables

1.1 Knudsen numbers of HT-PEFC species in GDL, T= 160 ℃, l_g = 20 µm. 21
1.2 Reynolds numbers and Mach numbers at the inlets of anode side and cathode side under different operating conditions of a HT-PEFC 23

2.1 Geometric parameters of composite HT-PFC cell structure. 33
2.2 Diffusion volumes of species. 38
2.3 The coefficients of Todd-Young's polynomials to calculate heat capacity and dynamic viscosity. 41
2.4 Physical parameters used in the basic model. 42
2.5 Physical parameters used in the macro-homogeneous model. 47
2.6 Physical parameters used in the water transfer model. 55
2.7 The solution methods of the transfer equations. PCG: preconditioned conjugate gradient solver; PBiCG: preconditioned bi-conjugate gradient solver; DIC: diagonal incomplete-Cholesky; DILU: diagonal incomplete LU. 63

3.1 Operating conditions of the mesh independence studies for both single channel pair and single cell with serpentine flow field. The mean current density was 4000 A/m^2. 66
3.2 Operating conditions for the basic model with the single channel pair geometry. The mean current densities were 1000 - 8000 Am^{-2}. 69
3.3 Porosities of the GDL by different engineering strains [107]. 90
3.4 Aninsotropic permeabilities under the channel/rib [132]. 90
3.5 Relative mass transfer errors of the species by different engineering strains. The mean current density of cases was 6000 Am^{-2}. 91
3.6 Current densities and cell voltages at the electrolyte-GDE interfaces with the GDL engineering strains of $0\,\%$, $10\,\%$, $18\,\%$ and $29\,\%$. 92
3.7 Labels and boundary conditions of Stefan tube simulation 97
3.8 Binary diffusivities in the channel and GDL at the cathode side. Components of the mixture: oxygen (1), water (2) and nitrogen (3). 100
3.9 Multi-component diffusion coefficients of Fick's law in the channel and GDL at the cathode side. Components of the mixture: oxygen (1), water (2) and nitrogen (3). 101

3.10 Diagonal and off-diagonal terms of Maxwell-Stefan formulation in the channel and GDL at the cathode side. Components of the mixture: oxygen (1), water (2) and nitrogen (3). 101

3.11 Operating conditions for the comparison of Fick's law and Maxwell-Stefan formulations with the reforming gas/air system. 102

3.12 The mole fraction of hydrogen, water, carbon dioxide and nitrogen at the electrolyte-GDE interface. 103

3.13 Binary diffusivities in the channel and GDL at the anode side. Components of the mixture: hydrogen (1), water (2), carbon dioxide (3) and nitrogen (4). 104

3.14 Multi-component diffusion coefficients in the channel and GDL at the anode side. Components of the mixture: hydrogen (1), water (2), carbon dioxide (3) and nitrogen (4). 105

3.15 Diagonal and off-diagonal terms of Maxwell-Stefan formulation in the channel and GDL at the anode side. Components of the mixture: hydrogen (1), water (2), carbon dioxide (3) and nitrogen (4). 105

3.16 Total mass flux of the generated water: comparison of the CFD simulation and the experiment. 118

6.1 Operating conditions for the serpentine single cell with the active area of 50 cm^2. The mean current densities were 0 - 8500 Am^{-2}. MEA: CELTEC P1000. 131

6.2 Operating conditions for the serpentine single cell with the active area of 50 cm^2. The mean current densities were 2000 Am^{-2}, 4000 Am^{-2} and 6000 Am^{-2}. MEA: CELTEC P1000. 133

Acknowledgments

During my PhD study, there are many people I want to say thank you, for their support, advice, and friendship. First of all, I would like to say thank you to my advisor Prof. Werner Lehnert for giving me the opportunity to study my PhD in Forschungszentrum Jülich. Prof. Lehnert has supported my study and research all the time with his patience, motivation, and knowledge of physics and fuel cells. His Email and office talk helped me a lot of the research and the writing of this thesis.

Besides my advisor, I would like to thank Prof. Steven Beale for sharing his valuable insights into topics on heat- and mass transfer problems. The discussion with him and his research gave me a lot of inspiration for my work. My sincere thanks also go to the rest of my thesis committee: Prof. Lorenz Singheiser, and Prof. Manfred Christian Wirsum, for their valuable time, effort and insightful comments.

I would like to say thank you to Dr Uwe Reimer and Dieter Froning, for the discussion of fuel cells, the talk of the modelling, the comments of my thesis, the help of the programming and IT skills and the time of the conference journey. Without their precious support, patience, and guidance, it would not be possible to conduct this research.

It is a pleasure to thank my colleagues in IEK-3: Stefanie Keuler, Sohyeon Lee, Huijie Zhang, Dr Fang Liu, Yu Lin, Junliang Yu, Yulin Yan, Shidong Zhang, Yasser Rahim, Manuel Langemann and Michael Höh, who all helped me in numerous ways during various stages of my PhD. I will remember the interesting discussions, the successful cooperations, and all the fun we have had in the last years. The friendships we developed will last a lifetime.

At Last, my deep and sincere gratitude to my parents and my wife, for their love, help, and encouragement all the time. This journey would not have been possible without their support, and I dedicate this milestone to them.

Band / Volume 376
Drying front formation in topmost soil layers as evaporative restraint
Non-invasive monitoring by magnetic resonance and numerical simulation
S. Merz (2017), xxii, 108 pp
ISBN: 978-3-95806-234-4

Band / Volume 377
Low Temperature Thin-Film Silicon Solar Cells
on Flexible Plastic Substrates
K. Wilken (2017), 194 pp
ISBN: 978-3-95806-235-1

Band / Volume 378
Dissolution Behaviour of Innovative Inert Matrix Fuels
for Recycling of Minor Actinides
E. L. Mühr-Ebert (2017), xii, 164 pp
ISBN: 978-3-95806-238-2

Band / Volume 379
Charakterisierung und Modifizierung von Kupferoxid- und Kupfersulfid-
Nanopartikeln für Dünnschichtsolarzellen
J. Flohre (2017), 141, iii pp
ISBN: 978-3-95806-241-2

Band / Volume 380
Einzelfaserkomposite aus Pulvermetallurgischem
Wolfram-faserverstärktem Wolfram
B. Jasper (2017), v, 92, XVIII pp
ISBN: 978-3-95806-248-1

Band / Volume 381
Untersuchungen zur Deckschichtbildung auf $LiNi_{0,5}Mn_{1,5}O_4$-
Hochvoltkathoden
Die Kathoden/Elektrolyt-Grenzfläche in Hochvolt-Lithium-Ionen-Batterien
K. Wedlich (2017), xvi, 157, xvii-xxvi pp
ISBN: 978-3-95806-249-8

Band / Volume 382
Charakterisierung gradierter Eisen/Wolfram-Schichten
für die erste Wand von Fusionsreaktoren
S. Heuer (2017), x, 234 pp
ISBN: 978-3-95806-252-8

Band / Volume 383
High resolution imaging and modeling of aquifer structure
N. Güting (2017), viii, 107 pp
ISBN: 978-3-95806-253-5

Band / Volume 384
IEK-3 Report 2017
Sektorkopplung –
Forschung für ein integriertes Energiesystem
(2017), 182 pp
ISBN: 978-3-95806-256-6

Band / Volume 385
Bestimmung der Wolframerosion mittels optischer Spektroskopie unter ITER-relevanten Plasmabedingungen
M. Laengner (2017), vi, 184, XI pp
ISBN: 978-3-95806-257-3

Band / Volume 386
IEK-3 Report 2017
Sector Coupling –
Research for an Integrated Energy System
(2017), 175 pp
ISBN: 978-3-95806-258-0

Band / Volume 387
Photochemistry of Highly Oxidized Multifunctional Organic Molecules: a Chamber Study
L. I. M. Pullinen (2017), II, 96, xviii pp
ISBN: 978-3-95806-260-3

Band / Volume 388
Poröse Transportschichten für die Polymerelektrolytmembran-Wasserelektrolyse
M. Höh (2017), VI, 186 pp
ISBN: 978-3-95806-262-7

Band / Volume 389
Modelling of High Temperature Polymer Electrolyte Fuel Cells
Q. Cao (2017), 173 pp
ISBN: 978-3-95806-263-4

Weitere ***Schriften des Verlags im Forschungszentrum Jülich*** unter
http://wwwzb1.fz-juelich.de/verlagextern1/index.asp

Energie & Umwelt / Energy & Environment
Band / Volume 389
ISBN 978-3-95806-263-4

JÜLICH
FORSCHUNGSZENTRUM